AN NMR STUDY OF SUPERCOOLED WATER UNDER NANOCONFINEMENT BY HYDROPHOBIC SURFACES

Yan-Chun Ling

A dissertation submitted to the faculty at University of North Carolina at Chapel Hill in Partial fulfillment of the requirements for the degree of Doctor of Philosophy in the Department of Applied Physical Sciences

Chapel Hill
2017

Approved by

Sean Washburn

Yue Wu

Max Berkowitz

Rene Lopez

Jonathan Heckman

ABSTRACT

Yan-Chun Ling: An NMR Study of Supercooled Water under Nanoconfinement by Hydrophobic Surfaces
(Under the direction of Yue Wu)

The main focus of this dissertation is studying the properties of bulk water, confined water, and interfacial water.

The thermodynamics, dynamics and state of water are investigated by DSC and ^{1}H NMR methods. Hydrophobic slit-shaped pores with tunable pore size from 0.5 nm to 1.6 nm are applied as confinement media in our experiments. By confining water in nanopores, we are able to cool the water lower than its homogeneous nucleation temperature 235 K at ambient pressure and access the “no man’s land”. Both experimental and simulation results show water has heterogeneity property, with two “phases”, one is high-density liquid (HDL) “phase” which has dense-packing structure, the other is low-density liquid (LDL) “phase” which has more tetrahedral structure. At room temperature, HDL and LDL two “phases” can coexist in millisecond time scale and 10 nanometer length scale. The room temperature water structure is dominated by HDL structure. By decreasing the temperature, HDL could convert to LDL gradually. At 200 K, LDL dominates the liquid state of water. It is of importance to emphasis, for water confined in nanopores there is no crystallization above 200 K. A dynamic crossover at 225 K in the liquid state is observed in our hydrophobic system, similar to that observed in hydrophilic system. This proves such dynamic crossover is not induced by crystallization or surface effect, but originally from the intrinsic properties of water. At 190 K, we find a second

change of rotational correlation time, which resembles the glassification process of supercooled confined water, suggesting a higher rotational glass transition temperature for bulk water. In the lower temperature range 145 K < T < 165 K, the interfacial water induced glass transition is observed. At sufficient low temperature, confinement plays an important role for the induced glass transition.

We also study the properties of interfacial water by confining water in smaller hydrophobic pores. It shows the interfacial water remains liquid state at 140 K. There is an Arrhenius to Arrhenius dynamic crossover at 170 K due to the rotational motion slowing down. Comparing to bulk water, interfacial water has fast rotation but effectively immobile.

Our studies thus provide a complete picture for the rather controversial supercooled region and also differentiate the properties of bulk water, confined water and interfacial water using different techniques.

ACKNOWLEDGEMENTS

I want to express my sincere appreciation to my advisor, Prof. Yue Wu, for giving me the opportunity to work with him and made this possible. In the beginning of my 3rd year of graduate school, I remember to make the decision to switch my research area from polymer theory to condensed matter physics without any NMR experimental experience. Prof. Wu's continuous encouragement, inspiration, and patience give me confidence to continue scientific research, have scientific characteristics and ambitious. During the past five years, he has taught me how to do research and also guided me seeing the forest for trees. With that being said, I know I could not come this far without the support and help from my advisor and members in our research group.

I am especially grateful towards Prof. Alfred Kleinhammes for his mentorship during my graduate career. His sense of humor, friendship, and appreciation of running are invaluable. He is always supportive and helpful when I had questions on NMR, taught me how to handle hardware and gave me advice on life in general.

I am happy to have met Prof. Horst Kessemeier and learn about his many contributions to NMR. I enjoyed many of our talks regarding NMR and Tai Chi and I believe these two things must have some subtle relationship to be a pioneer of NMR.

Many measurements performed for this dissertation were using equipment in the Wuhan National High Magnetic Field Center, I am very grateful to Dr. Yu Yao, who opened the lab and gave lots of valuable suggestions on my project. I also thank En-Yi Chen, Shi-Yu Liu, Xun Liu,

and Liang Peng, who in addition to being good friends, graciously and patiently assisted the experiments.

I would like to express my special gratitude to our research collaborate: Prof. Li-Mei Xu and Rui Wang in Peking University, International Center for Quantum Materials and School of Physics. Prof. Xu paid lots of attention on our paper, she taught me on hands and gave me a good example how to write a scientific paper. Rui Wang always gave quick response on my questions on her simulation results. Their computational work greatly help us for deeper understanding and further convincing the experimental conclusion.

I am grateful to my committee members, Profs. Sean Washburn, Max Berkrowtiz, Rene Lopez, and Jonathan Heckman for challenging me to be a better scientist, for reading and offering helpful advice on my dissertation.

Many excellent graduate students passed through Wu's lab, I have had a lot of help from the previous and current members of Wu's group. They are: Magdalena Sandor, Jacob Forstater, Shaun Gidcumb, Zhi-Xiang Luo, Yuan Chong, Yun-Zhao Xing, Patrick Doyle and Yan Song. Especially, Magdalena Sandor, I could not express how many times she helped me to construct the high-T probe by telephone calls and emails. I appreciated the conversations between us make light of any difficult and stressful situation I had, although I have never met her. I benefit a lot from the discussions with Zhi-Xiang Luo, Yuan Chong, and Yun-Zhao Xing that their ideas were very insightful and broaden my view on science. Enjoying coffee time and hanging out for outdoor activities with Yan Song, Yun-Zhao became precious memories during these years.

Antoinette Setari, Maggie Jensen, Julia Green and other staffs in the Department of Physics, Department of Applied Physical Science, along with the office of Graduate School, the

FedEx Global Center for International Students and Scholars have provided numerous support through the years. My PhD journey won't have been so smooth without their help.

Thanks also go to my friends, you know who you are: Lei Wang, Yanqian Wang, Lei Zhang, Xiao Yu, and Yuwei 'Freda' Xiong. Your encouragement has sustained me. Especially my two cats: Schrödinger and Booties, thanks for enduring my "harassment" and waiting for me in front of the window every night.

Last but not least, this thesis is dedicated to my parents, grandparents, and granduncle. Words cannot express my thanks. They let me know parents are the best gift to Children and it's never too old to learn.

TABLE OF CONTENTS

LIST OF TABLES

LIST OF FIGURES

LIST OF ABBREVIATIONS

LDA	Low density amorphous
HDA	High density amorphous
LDL	Low density liquid
HDL	High density liquid
LDW	Low density water
HDW	High density water
LLPT	Liquid-liquid phase transition
LLCP	Liquid-liquid critical point
MD	Molecular dynamic
DSC	Differential scanning calorimetry
NMR	Nuclear magnetic resonance
QENS	Quasi-elastic neutron scattering
BDS	Broadband dielectric spectroscopy
XRD	X-ray diffraction
PES	Potential energy surface
LSI	Local structure index
VFT	Vogel-Fulcher-Tammann
RF	Radio frequency
CPMG	Carr-Purcell-Merbromin-Grannie
HB	Hole burning
NICS	Nuclei independent chemical shift

PEEK	Polyether ether ketone
MAS	Magic angle spinning
FWHM	Full width at half maximum

CHAPTER 1 INTRODUCTION

1.1 Water: The Matrix of Life

1.1.1 Bulk Water

Water is the most abundant and important compound on earth. It covers 71% of the planet's surface and I the main constituent of living organisms. As we know, the water molecule is composed of one oxygen atom and two hydrogen atoms, featuring the O-H bond length of 0.9572 Å and a O-H-O bond angle of 104.5° (see **Figure 1.1 (a)**) [1]. One of the interesting features of water molecules is their tendency to connect with other water molecules by hydrogen bonds, ideally forming a tetrahedral structure as shown in **Figure 1.1(b)**. [1]

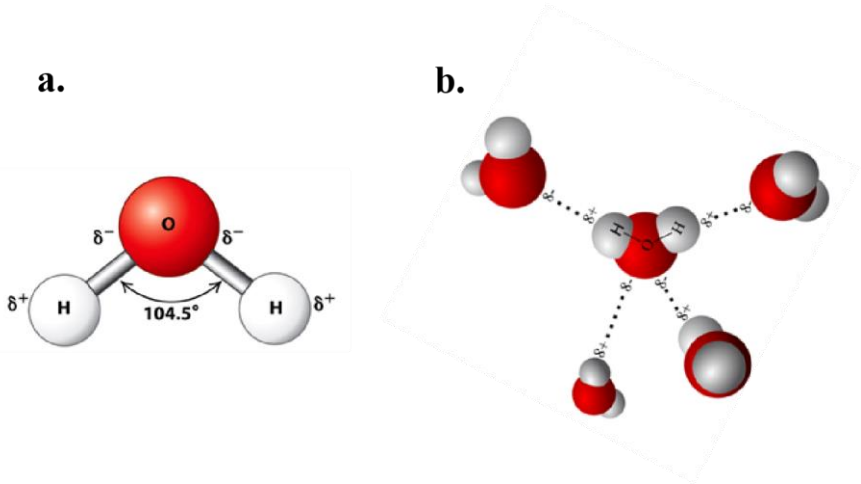

Figure 1.1 (a) A ball and stick model of a single water molecule. The solid red ball represents the oxygen atom. The solid white balls are hydrogen atoms. (b) A four-coordinated water molecule demonstrating the tetrahedral structure of one water molecule bonding with four other neighboring water molecules. The hydrogen bond acceptor. The central water molecule accepts two hydrogen bonds from its lower neighboring water molecules and donates two hydrogen bonds to its upper neighbors. [1]
Note: motif credit: John Millam

The orientation of the hydrogen bonds, variation in hydrogen bond length, and variable number of coordinated water molecules can affect the local structure of water, resulting in the anomalous behavior of water [2]. For instance, water may not always be tetrahedral due to changes in temperature and pressure. This is not the case of most normal liquids, which tend to have a constant number of coordinates in a wider pressure and temperature range. In general, when cooling down a liquid to its crystal state, the density will increase due to molecular dense packing, and therefore the density of crystal is larger than that of the liquid. However, water experiences the opposite effect. The maximum density of water occurs at 4 °C in the liquid state than in the ice state. This property is crucial to the ecology system on earth. Because in the cold winter, rivers, lakes, and oceans, they freeze from the top down, which permit the survival of the bottom ecology, insulating the water from further freezing, and allowing rapid thawing by sunlight. Compared to normal liquids, water also has a large specific heat capacity that can be defined by the fluctuation of entropy (S) as shown in **Eq. (1.1)** [3],:

$$< (\delta S)^2 >= k_B C_P \tag{1.1}$$

in which k_B is the Boltzmann constant. The high isothermal compressibility, κ_T, of water can be characterized by volume fluctuation as described in **Eq. (1.2)** [3],:

$$< (\delta V)^2 >= V k_B T \kappa_T \tag{1.2}$$

The large heat capacity of the seas (4.12 $\mathrm{J \cdot g^{-1} \cdot K^{-1}}$) [1] allows them to act as huge heat reservoirs, such as that sea temperature varies by one-third of as much as the temperature on lan , and so moderates the planet's climate [4]. The low compressibility of water reduces sea level by about 40 m to give us 5% more land [4].

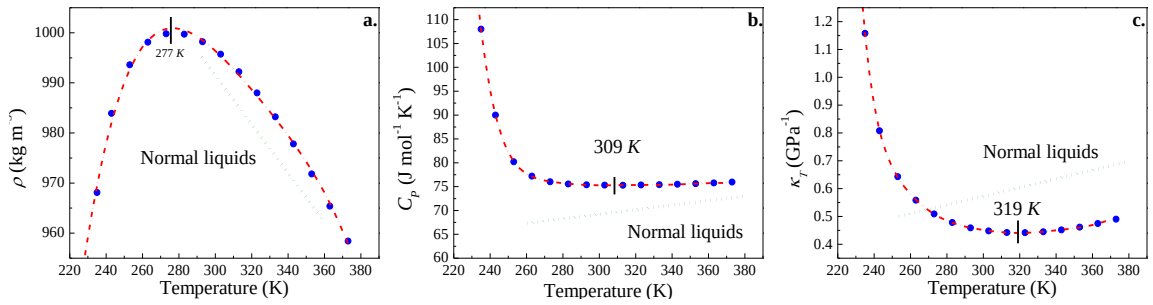

Figure 1.2 Experimental measurements of the (a) density (ρ) [1], (b) specific heat (C_P) [5], and (c) isothermal compressibility (κ_T) of bulk water [6] at a temperature range of 380-235 K. The green dot lines represent the behaviors of normal liquids

The notable properties of water are more accentuated at low temperatures, as shown in **Figure 1.2 (a)-(c)**. For example, when water is supercooled below its freezing temperature 273 K unlike other supercooled liquids (the green dot lines in **Figure 1.2**), the specific heat capacity C_P and compressibility κ_T of bulk water increase rapidly toward "infinity" at 235 K. If we fit the C_P and κ_T with a power law function, see Eq. (1.3) (1.4)

$$C_P \sim \left(\frac{T}{T_s} - 1\right)^{-0.26} \tag{1.3}$$

$$\kappa_T \sim \left(\frac{T}{T_s} - 1\right)^{-0.36} \tag{1.4}$$

we can find it diverges at $T_s = 228$ K from the fitting results [5, 6].

Unfortunately, detailed investigations about supercooled bulk water around 228 K cannot be carried out experimentally, since bulk water crystallizes rapidly below the homogeneous nucleation temperature $T_H \approx 235$ K at atmospheric pressure [7]. So, how to build up a theoretical model to understand the anomalies of water and how to develop experimental techniques to capture the supercooled water properties below T_H become the key to explain the mysteries of water.

1.1.2 Phases of Bulk Water

Phase diagrams show the preferred states of matter at different temperatures and pressures. With each phase, the material is uniform with respect to its chemical composition and physical state. The phase diagram of water is complex. For example, ice has 16 known phases at low temperature and different pressures [8].

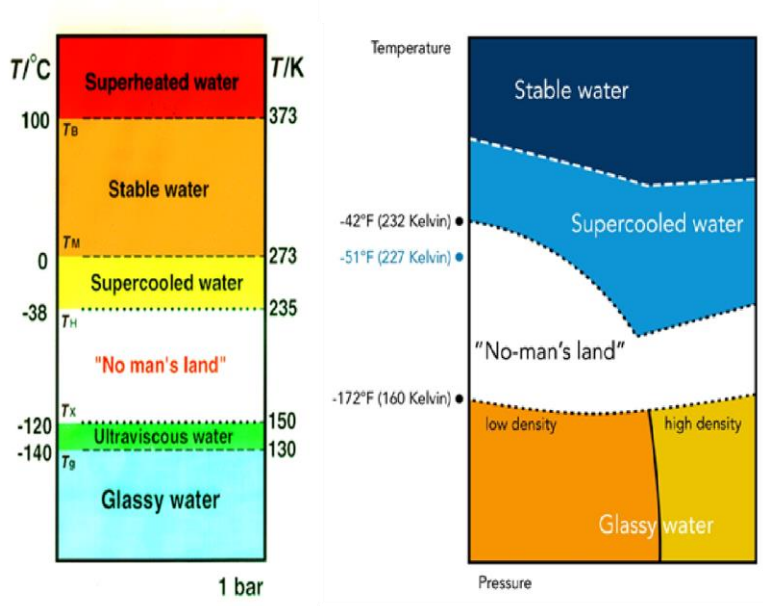

Figure 1.3 (a) The state of water at ambient pressure [9]. (b) The temperature-pressure phase diagram of water [10]. The solid black line that divides the orange and yellow-shaded areas at the bottom of the temperature-phase (*T*-*P*) diagram indicates a phase transition between LDA and HDA, which has been experimentally observed

Note: T_B is the boiling temperature, $T_B\ (P = 1\text{atm}) = 373$ K; T_M is the hexagonal ice (I_h) melting temperature, at 1atm, $T_M(P = 1\text{atm}) = 273$ K; T_H is the homogeneous nucleation temperature, $T_H(P = 1\text{atm}) = 235$ K; T_X is the cubic ice (I_c) crystallization temperature, $T_X(P = 1\text{atm}) = 150$ K; T_g is the putative glass transition temperature, $T_g(P = 1\text{atm}) = 130$ K. *P* represents pressure.

According to **Figure 1.3 (a)** [9], liquid water can be supercooled to $T_H = 235$ K, which is the homogeneous nucleation temperature (T_H) and therefore it cannot be cooled further or remain in the liquid state due to the spontaneous crystallization to hexagonal ice (I_h). However, water can also exist in a glassy state below 130 K by cooling micrometer-sized water droplets at a rate of $10^6\ K/min$ [11] (see the bottom light blue box in **Figure 1.3 (a)**). Then by heating the glassy

water above 130 K it transforms to a highly viscous liquid that exists up to 153 K [12], at which point it changes to cubic ice [13]. As marked in **Figure 1.3 (a)**, this temperature range between 153 K to 235 K is called "no man's land" because there is no stable liquid water survival in this regime. Therefore, it is extremely difficult to study the nature of the sharp increase of water's thermal properties towards $T_s = 228\ K$ in bulk water by means of experimentation, although some progress has been recently made [14].

Depending on the pressure (*P*) and temperature (*T*), as shown in **Figure 1.3(b)** , water has two amorphous states: a low density amorphous (LDA) state, which was first observed by depositing water vapor on a cold plate 80 years ago [11]; and a high density amorphous (HDA) state, which researchers discovered by compressing hexagonal ice (I_h) below 150 K at high pressure [15-19].

In addition to the original preparation method based on the vapor and crystalline phases of water, LDA can be formed directly from HDA, which is called a polyamorphic transition with a large volume change [20]. The properties of the amorphous states change discontinuously at this polyamorphic transition [20]. Therefore, the transformation between LDA and HDA appears to be a first-order phase transition rather than a relaxation phenomenon between two unstable amorphous changing continuously from LDA to HDA [17].

This well-established first order phase transition between the amorphous states of water suggests an idea that can be extended to higher temperatures in the "no man's land" region of the phase diagram, namely that there exists low density liquid (LDL) and high density liquid (HDL) whose corresponding glass forms are LDA and HDA [21-24], respectively. The two liquid phases, LDL and HDL, have different local structures [25]. The LDL structure is driven by H-

bond and form more tetrahedral structure network, while the HDL is more dense packing and less tetrahedral structure which interacts with other water molecules by Van de Walls interaction.

The following section will introduce different hypotheses and models that attempt to explain the anomalous properties of bulk water and the state of supercooled water in the "no man's land" region of the phase diagram.

1.1.3 Dissertation Outline

In subsequent chapters, I will discuss the properties of water in a wide temperature range from room temperature to supercooled region. To access the "no man's land" temperature region, we confined bulk water in nanoporous materials by hydrophobic surfaces to avoid crystallization at low temperatures. DSC and NMR were performed on the nanoconfined water samples to investigate the structure, thermodynamic, and dynamic properties of water under nanoconfinement in the wide temperature range.

Chapter 1 briefly reviews the main hypotheses of bulk water in a wide temperature regime which includes the heterogeneity model of water at high temperature and three models for supercooled water to explain the anomalies of water properties. The important experimental evidences, MD simulation results are also reviewed and discussed in this chapter.

Chapter 2 introduces the principle of NMR and DSC techniques, material characterization methods, and detailed NMR pulse sequence we applied in the experiments.

Chapter 3 reports the structure, thermodynamic, and dynamic properties of water under hydrophobic nanoconfinement from 290 to 200 K, as measured by NMR and DSC. The experimental results and simulation discussion show that water has heterogeneity property. Above 200 K, the nanoconfined water is in a liquid state without crystallization and a dynamic

crossover is observed at 225 K due to the quick conversion from HDL to LDL which relates to the intrinsic property of bulk water.

Chapter 4 focuses on the observation of the rotational glass transition of water at 190 K. At 200 K, LDL dominates the water structure. Below 200 K, there is a second Arrhenius to Arrhenius transition occurring at 190 K due to change of low-density water molecular tumbling motion. The NMR spectra analysis shows part of the LDL forms amorphous ice. This is a strong evidence that supercooled water transfers to the glassy state below 200 K.

Chapter 5 reports another glass transition observed from the endothermic shoulder at 150 K on the DSC curve. We proved only existing "carbon surface/interfacial water/bulk-like water" sandwich structure would have this transition. So, this glass transition is induced by interfacial water.

Finally, Chapter 6 I extended my work to the role of interfacial water from 290 K to 140 K. I provided evidence that for monolayer water confined in nanopores, it doesn't freeze at extremely low temperature, and have an Arrhenius to Arrhenius transition at 170 K.

1.2 Hypotheses, Simulation Discussions, and Experimental Evidences of Water

1.2.1 Hypotheses of Supercooled Bulk Water

As mentioned in Section 1.1.2, the LDA to HDA first order phase transition and liquid-gas critical point inspired scientists to have the similar idea to the water in the "no man's land". They assume if heating glassy water to higher temperature, there could have LDL which is the LDA glass forming liquid and HDL which is the HDA glass forming liquid coexist in "no man's land" [26]. For such liquid-liquid coexistence model, there are three main theoretical physics pictures: (1) stability limit hypothesis [6] (2) singularity-free hypothesis [27, 28] (3) liquid-liquid critical point hypothesis [26]. This section will briefly review the physic in these three models.

One of the popular explanations for the anomalous behaviors of liquid water is the stability limit hypothesis [6], which assumes that the spinodal temperature line, $T_S(P)$, in the pressure-temperature (P-T) phase diagram of water connects to the locus of the liquid-to-gas spinodal (i.e., the limit of metastability) of superheated water. It predicts that liquid water cannot be cooled or stretched beyond the $T_S(P)$ line [29].

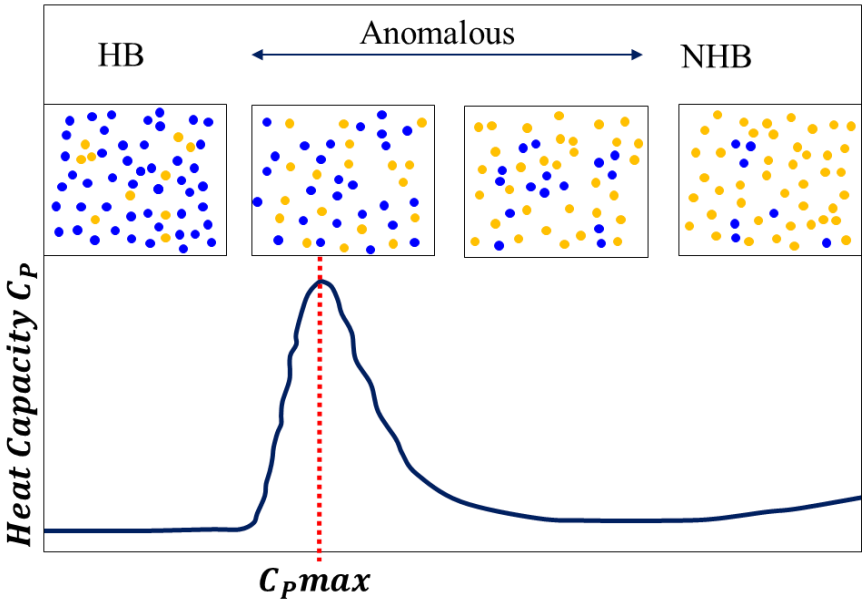

Figure 1.4 Illustration of singularity-free hypothesis. The yellow dots represent water connecting each other by non-hydrogen bonds and the blue dots represent water connecting each other by hydrogen bonds

The second theory about supercooled bulk water is called the percolation hypothesis [27, 28, 30-32], which is also referred to as the singularity-free hypothesis (**Figure 1.4**). It claims that the thermal response functions of bulk water in the supercooled region have a rapid rise without singularity. Sastry and Stanley treated bulk water as a network connected with the neighboring water molecule both by hydrogen bonds and non-hydrogen bonds (Van de Walls interaction). The Hamiltonian of water molecules in the network is Eq. 1.5

$$\mathcal{H} = \mathcal{H}_{NHB} + \mathcal{H}_{HB} = -\epsilon \sum_{i,j}^{<1,2>} n_i n_j - J \sum_{i,j}^{<1,2>} n_i n_j \delta_{ij} \quad (1.5)$$

Where the $\mathcal{H}_{NHB}$ is the non-hydrogen bond Hamiltonian and the $\mathcal{H}_{HB}$ represents the Hamiltonian part for hydrogen bond. ϵ and J are the energy for non-hydrogen bonds and hydrogen bonds interaction. n_i, n_j represent nearest neighbor occupation. δ_{ij} is the angle between two nearest water molecules. The heat capacity and other thermal response functions are solved by the network partition function. This hypothesis considers water as a locally structured gel comprised of "monomers" (i.e., water molecules) held together by hydrogen bonds and non-hydrogen bonds. When temperature decreases, the number of monomers held by hydrogen bonds increases. These growing local "patches" formed by water molecules lead to enhanced fluctuations of specific volume and entropy, which results in a drastic increase of the thermal response functions of supercooled water, such as specific heat and compressibility. However, the percolation hypothesis fails to explain the first order phase transition of the amorphous states from LDA to HDA [27, 33].

The third theory is called the liquid-liquid phase transition (LLPT) hypothesis[26], which was inspired from the gas-liquid phase transition of water and molecular dynamic (MD) simulations. As shown in both experiments and theory, below the gas-liquid critical point *C* (see **Figure 1.5**), where the critical temperature $T_C = 647\ K$ and the critical pressure $P_C = 22\ MPa$, the superfluid phase separates into two new phases: a low-density gas phase at low pressure and a high-density liquid phase at high pressure [34]. The thermodynamic response functions are at a maximum on the Widom line, which corresponds to the maximum fluctuations of structures just beyond the liquid-gas critical point, *C*, in the higher temperature and higher pressure region [26]. Similarly, beyond the predicted second critical point, *C'*, in the liquid-liquid phase transition,

there will also be two phases: a low-density liquid phase at low pressure and a high-density liquid phase at high pressure [35, 36]. The LLPT hypothesis also predicts there is a Widom line beyond *C'*, as the red dashed line shown in Figure 1.5.

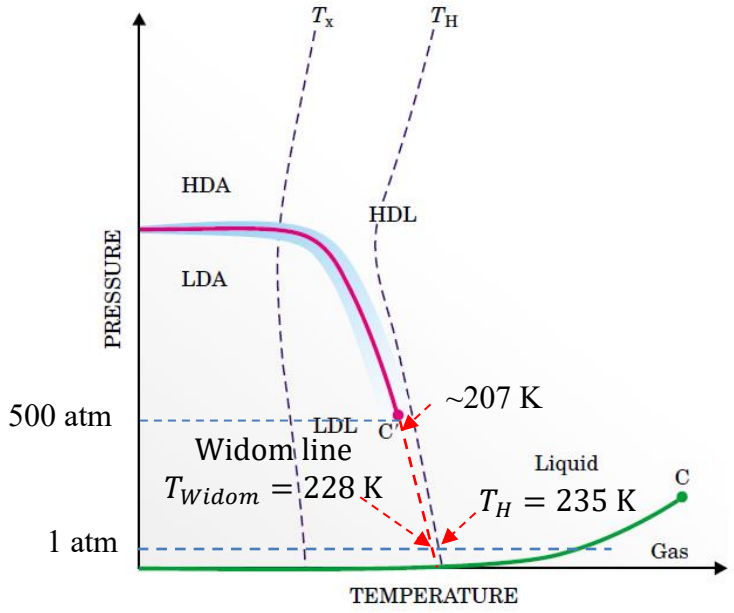

Figure 1.5 The liquid-liquid phase transition (LLPT) of water under ambient pressure as predicted by the LLPT hypothesis. **C** is the liquid-gas critical point and **C'** is the hypothesized liquid-liquid critical point around $T_{C'}$ = 207 K and $P_{C'}$ = 50 MPa (simulation results) [37]. The magenta solid line is the coexistence line of HDA-LDA and HDL-LDL predicted from LLPT hypotheses. Dashed red line denotes the Widom line, which intersects with the 1 atm pressure line at $T_W = 228\ K$ [26, 28, 34]

It is of importance to emphasis that the Widom line intersects with 1 atm pressure line at temperature $T_W = 228\ K$ [26], which is the same as T_S (fitted from **Eq. 1.3, 1.4**).

1.2.2 Hypothesis of Heterogeneity of Water: two-state model

Dating back to 1892, Roentgen's proposal, he considered water is a mixture of two basic components, a icelike component and a normal liquid component[38]. Roentgen's essential idea has been developed and extended by many researches [39]. This hypothesis has been successfully in explaining the anomalous properties of bulk water.

Anisimov et. al considered the pure water working as a non-ideal mixed solution[40, 41]. Assume the fraction of state B (LDL) is x with chemical potential μ^B, and the fraction of state A (HDL) which has chemical potential μ^A is $(1-x)$. The overall Gibbs energy for such mixed water is Eq. (1.6)

$$G = (1-x)\mu^A + x\mu^B = \mu^A + x(\mu^B - \mu^A) = \mu^A + x\mu^{BA} \tag{1.6}$$

Where μ^{BA} is defined as the chemical potential different between state A and B. The Gibbs energy of the mixture is derived in Eq. (1.7)

$$\frac{G}{k_B T} = \frac{\mu^A}{k_B T} + x\frac{\mu^{BA}}{k_B T} + xlnx + (1-x)ln(1-x) + \omega x(1-x) \tag{1.7}$$

Where ω is state A and B interaction parameter, variant with temperature and pressure.

However, the two-state model or heterogeneity hypothesis is based on mean field theory not affected by fluctuation. So, when the fraction x approach to the critical fraction x_c, **Eq. (1.7)** should consider Landau expansion. The crossover theory developed by Anisimov et. al [42]combining with the two-state mean field theory in a wide temperature range predicts there is a sharp change of thermal response function without discontinuity [43].

1.2.3 Liquid-Solid Transition Hypothesis

There is another hypothesis to understand the supercooled water: Chandler thought the phenomenon predicted in LLPT that stable HDL and LDL phase coexistence at low temperature high pressure is putative [44]. The liquids demonstrated in LLPT hypothesis are metastable phases, especially the low-density liquid is suggested to being coarsening of the ordered ice-like phase.

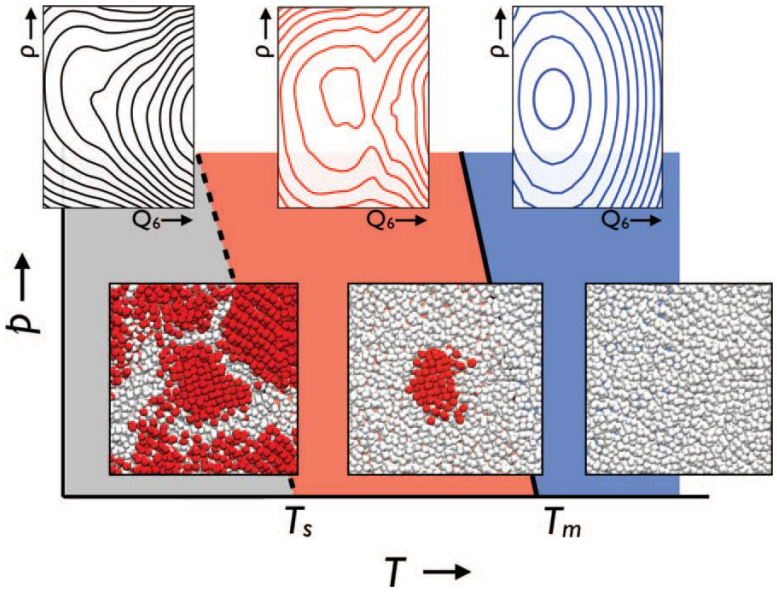

Figure 1.6 Pressure-Temperature (*P-T*) Phase diagram of supercooled water. T_m and T_s represent melting temperature and stability limit temperature. Blue region in the P-T plane is the stable state of liquid, red region is where the liquid is metastable, and grey region is where liquid is unstable. The free energy surfaces of liquids are shown above in a function of density and structure orientation parameter Q_6. The molecular configurations from simulation are shown below. The white patches are representing liquids, the red patches are coarse grained ice, respectively[45].

Figure 1.6 shows the pressure-temperature phase diagram of bulk water from liquid-solid transition hypothesis. The liquid is the stable equilibrium phase above ice-water melting temperature $T > T_m$, and is unstable below the stability limit temperature T_s. Between $T_s < T < T_m$, intermediate region, liquid is metastable phase with respect to crystal ice. In liquid-solid transition hypothesis, during the intermediate temperature region, the water structure relaxation is slower when going to lower temperature. When the temperature approach to the stability limit temperature T_s, coarsening of water occurs on time scale in milliseconds and such water is preparing to form coarse-grained ice. The free energy surfaces for water below T_s shows it is not a stable phase. The snapshot from the simulation box also shows the coarse-grained ice forming faster than the liquid structure relaxation.

In summary, the LLPT hypothesis considers water has a second metastable critical point at high pressure low temperature. The long-range fluctuation from the critical point could affect the properties of bulk water at lower pressure higher temperature. The anomalous properties of water are the influence from the hidden second critical point. The singularity-free scenario shows, there is the appearance of sharp but continuous changes in density and entropy at low temperature without hidden critical point. The anomalies of water at ambient pressure supercooled region can be reproduced by adjusting the water cooperativity parameter. Spinodal stability limit hypothesis and solid-liquid transition hypothesis both consider supercooled water is unstable liquid below T_s. The sharp increase of the thermal properties of supercooled water are due to approaching the stability line. The two-state model is discussing the problem from another point of view. It treated water as a mixture of two types of clusters. One is liquid-like (high-density liquid) cluster and the other is ice-like (low-density liquid) cluster. By modulating the interaction parameter, Anisimov et. al also can reproduce the anomalies of water at ambient pressure in supercooled regime.

1.2.4 Simulation Results from Different Water Models

Water is a particularly difficult material to simulate because it is a molecular liquid and researchers have been unable to universally agree on its tractable intermolecular potential [46]. Nevertheless, there is still a distinct advantage of using simulations over experiments when studying the bulk water. Even the most recent experimental techniques, such as X-ray diffraction [14] still cannot probe the “no man’s land” region of the phase diagram due to the homogeneous nucleation of the supercooled water from liquid to ice. However, nucleation will not occur on the timescale of computer simulations, which is typically in the picosecond range. Therefore, simulations have the ability to probe the local structure and dynamics of water below T_H.

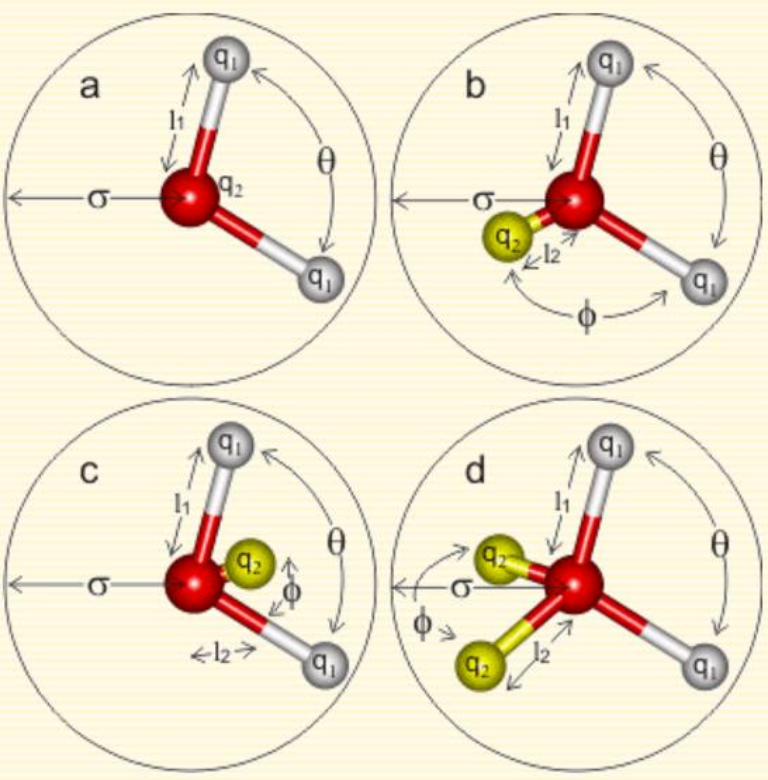

Figure 1.7 Simple water molecule models and their structure parameters. Model types a, b and c are all planar, whereas type d is almost tetrahedral [47]. The middle point site in c and the lone pair sites in d are labeled q2. The model types (a-d) are explained and defined in Table 1.1

Note: σ is the average distance between water molecules; I_1 is the O-H bond length; I_2 is the average distance between oxygen to the nearest neighboring hydrogen; q_1 is the charge on hydrogen; q_2 is the average charge on oxygen; θ^0 is the H-O-H bond angle; ϕ^0 is the angle between two nearest neighboring hydrogens

Table 1.0.1 Parameters of Selected Water Molecule Models

Water Model	**Type**	$\boldsymbol{\sigma}$ **(Å)**	$\boldsymbol{\epsilon}\ (\frac{\boldsymbol{kJ}}{\boldsymbol{mol}})$	$\boldsymbol{I_1}$ **(Å)**	$\boldsymbol{I_2}$ **(Å)**	$\boldsymbol{q_1}\ (\boldsymbol{e})$	$\boldsymbol{q_2}(\boldsymbol{e})$	$\boldsymbol{\theta}^\circ$	$\boldsymbol{\phi}^\circ$
ST2[48]	d	3.1	0.3169	1	0.8	+0.243	-0.2436	109.47	109.47
SPE/C[49]	a	3.166	0.650	1	-	+0.4238	-0.8476	109.47	-
TIP4P/2005[50]	c	3.159	0.7749	0.957	0.1546	+0.5564	-1.1128	104.52	52.26
TIP5P[51]	d	3.12	0.6694	0.9572	0.7	+0.241	-0.241	104.52	109.47
WAIL[52]	c	2.483		0.9496		+0.686	-1.373	106.89	-

Table 1.0.2 Calculated physical properties of selected water molecule models and experimental data measured from bulk water

Model	$\boldsymbol{\mu}$	$\boldsymbol{\epsilon_r}$	$\boldsymbol{D_0}$ $(\boldsymbol{10^{-5}}\frac{\boldsymbol{cm^2}}{\boldsymbol{s}})$	$\boldsymbol{E_a}$ $(\frac{\boldsymbol{kJ}}{\boldsymbol{mol}})$	$\boldsymbol{\rho_0}$ (℃)	$\boldsymbol{\alpha}$ $(\boldsymbol{10^{-4}}\ ℃^{\boldsymbol{-1}})$
Experimental	2.95	78.4	2.30	-41.5	+3.984	2.53
SPE/C	2.35[53]	71[53]	2.49[54]	-41.5[53]	-38[55]	5.14[56]
TIP4P/2005	2.305[57]	60[57]	2.08[58]	-	+5[58]	2.8[58]
TIP5P	2.29[51]	81.5[51]	2.62[54]	-41.3[51]	+4[51]	6.3[51]
WAIL	-	80.8[59]	1.56[59]	-45.38[59]	+9[59]	-

Note: μ is dipole moment; ϵ_r is dielectric constant; D_0 is self-diffusion coefficient; E_a is activation energy to break the O-H bond; ρ_0 is the temperature at maximum density; α is thermal expansion coefficient.

ST2 (see **Figure 1.7 (d)**) water was the first simulated water model developed by Stillinger et al. in 1974 [48]. It exaggerates the real properties of water when the temperature approaches $T_H = 235\ K$. The MD results from the ST2 water model at low temperature and high pressure support the LLPT hypothesis. However, ST2 overestimates the melting temperature of ice, T_m, by 30 K [48]. Other water models, such as SPC/E (see **Figure 1.7 (a)**) TIP5P (see **Figure 1.7 (d)**) support the LLPT hypothesis at low temperature also, but SPC/E predicts the maximum density of water is at 240 K [54], and TIP5P predicts the ice I_h state to be metastable [51]. TIP4P/2005 (see **Figure 1.7 (d)**) is widely used nowadays. It predicts the maximum density temperature at 278 K. Figure 1.8 shows the snapshot of simulation results for TIP4/2005 water at room temperature and supercooled region. It is clear to see that water has two different local structures: HDL (yellow patches) and LDL (blue patches). At room temperature, water structure is dominated by HDL (less tetrahedral) structure. While at supercooled region, water structure is dominated by LDL (more tetrahedral) structure. Nilsson et. al have observed the continuous conversion between HDL to LDL by lowering temperature at ambient pressure. He concludes this continuous conversation is due to the influence from the hidden critical point from LLPT

hypothesis. But TIP4/2005 doesn't predict the melting temperature for ice-water transition precisely, it gives a T_m that is 20 K lower [58, 60]. There are also other models, such as the mW model, do not support LLPT, but rather suggest micro-crystallization of supercooled water occurs [45, 61]. However, none of these models were able to predict the phase diagram around the ice (I_h) melting temperature.

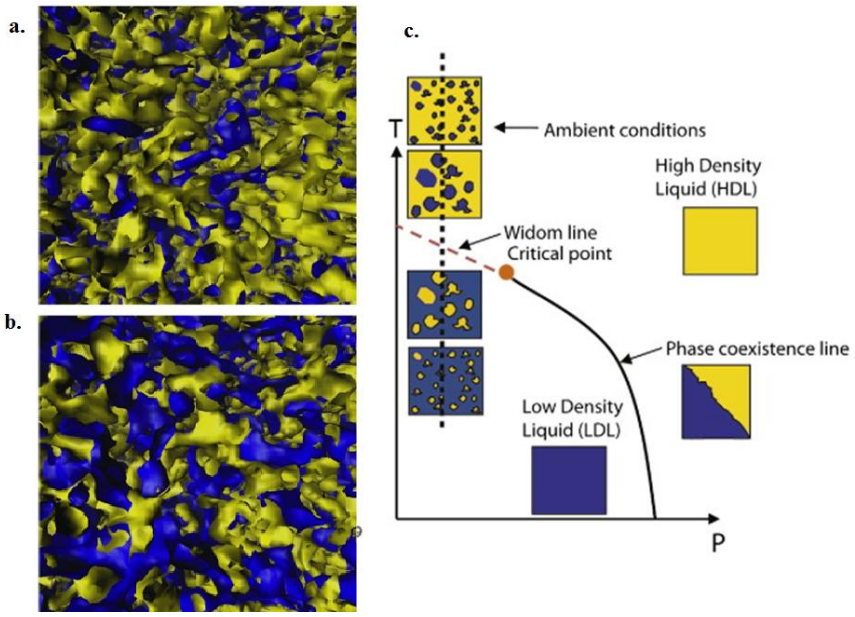

Figure 1.8 (a) Snapshot of simulation results for TIP4/2005 water at T = 340 K. (b) Snapshot of simulation results for TIP4/2005 water at T = 253 K. (c) Illustration of simulation results for TIP4/2005 at ambient pressure from room temperature to supercool region. And illustration of

hypothetical LLPT phase diagram. The yellow patches represent HDL water and blue patches represent LDL [62]

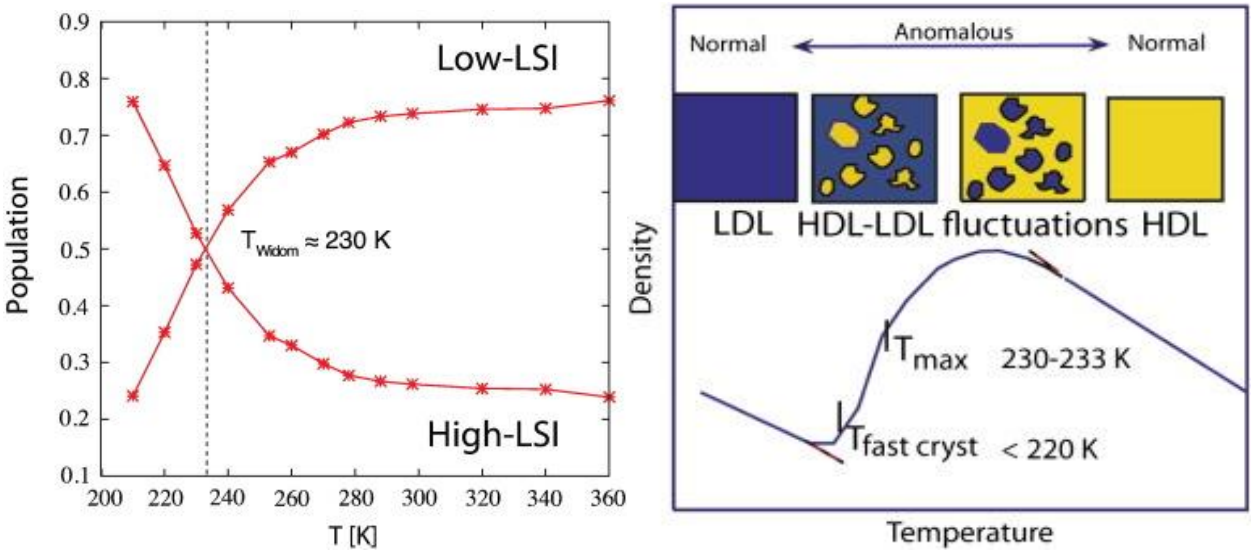

Figure 1.9 (a) The relative population of high-LSI and low-LSI from TIP4/2005 simulation results versus temperatures [63] (b) Hypothetical temperature dependent heterogeneity of water. The density of water separated in normal region and anomalous region. The blue solid line is the simulation result, the inserted pictures illustrate the continuous transition from HDL to LDL. From right to left, HDL dominated water structure, fluctuation into dense packing HDL liquid, HDL patches into LDL liquid, LDL dominates liquid. [62, 64]

Figure 1.9 (a) plots the conversion between local HDL and LDL versus temperature, (b) shows such local structure conversion resulting the anomalies of water. The local structure continuous conversion gives the anomalies of water at ambient pressure.

Recently, a new model named WAIL derived from Adaptive Force Matching for Ice was created through quantum and molecular mechanics calculations by fitting a coupled-cluster quality potential energy surface (PES) of water [52, 65]. The WAIL water predicts the T_m of ice (I_h) to be 270 K [59] and the temperature at its maximum density at 282 K [59].

The LLPT in supercooled water was observed by applying the WAIL model (**Figure 1.10**) [37]. At a pressure below 50 MPa, the density demonstrates a non-linear change with temperature. At 50 MPa, the change becomes more drastic. Above 50 MPa, the density adopts a

linear response as a function of temperature. The simulated liquid-liquid critical point occurs at a pressure and temperature of 50 MPa and 207 K [37].

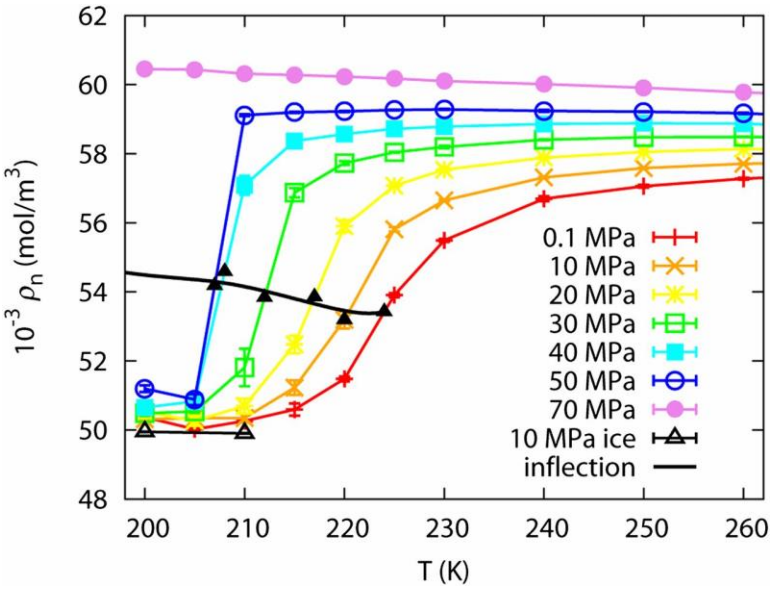

Figure 1.10 Density isobars of supercooled water from 200–260 K and 0.1–70 MPa. The densities of WAIL ice (I_h) at 10 MPa from 200–210 K is plotted as reference. [37]

In summary, the WAIL model describes the properties of water most accurately among these tremendous water models.

For this dissertation, we collaborated with Professor Limei Xu's group in Peking University who has expertise in WAIL water model simulations so that we could get the information of the diffusion coefficient of confined water and the local structures of supercooled water. Determining the rotational and translational diffusion coefficients will help us to understand the dynamic properties of water (e.g., molecular motions). Additionally, investigating the local structures of water may enable us to determine the existence of possible molecular structures in supercooled water. However, due to the limitations of the simplified energy, there is no exactly traceable potential to describe the real molecular potential of water which is extremely

important in MD simulation, therefore in order to confirm or disprove the theory and simulations, it is still necessary to collect experimental data.

1.2.5 Nanoconfined Water Experiments

Decades ago, scientists found when they confined water in nanopores, such as MCM-41 (a porous hydrophilic silica nanotube) [66-77], SBA-15 (a micellar material) [78], and layered vermiculite clay [79, 80], the freezing point could be suppressed to a low temperature region [81, 82], even avoiding crystallization altogether [82].

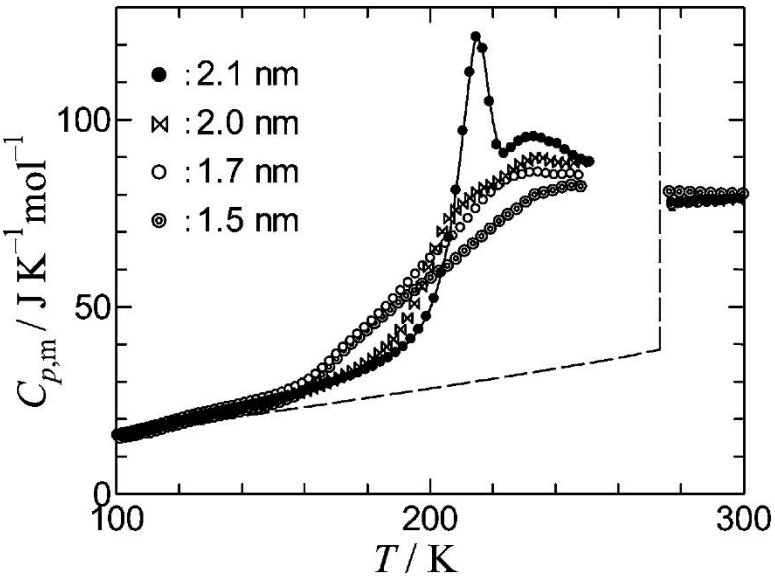

Figure 1.11 The heat capacity (C_P) of water confined in MCM-41 featuring different pore sizes (1.5–2.1 nm). The dashed line is the C_P of bulk water and ice, provided for reference [83]

Recent experimental studies on water confined in MCM-41 shed light on ways to investigate the properties of supercooled water in the "no man's land" region of the phase diagram. The specific heat capacity of water confined in different MCM-41 pore sizes showed that in a system featuring 2 nm-sized confinement or less, there was no fusion of ice (**Figure 1.11**). This result indicates that nanoconfinement can prevent crystallization of water and enable us to measure the properties of water in the temperature range between 150–230 K.

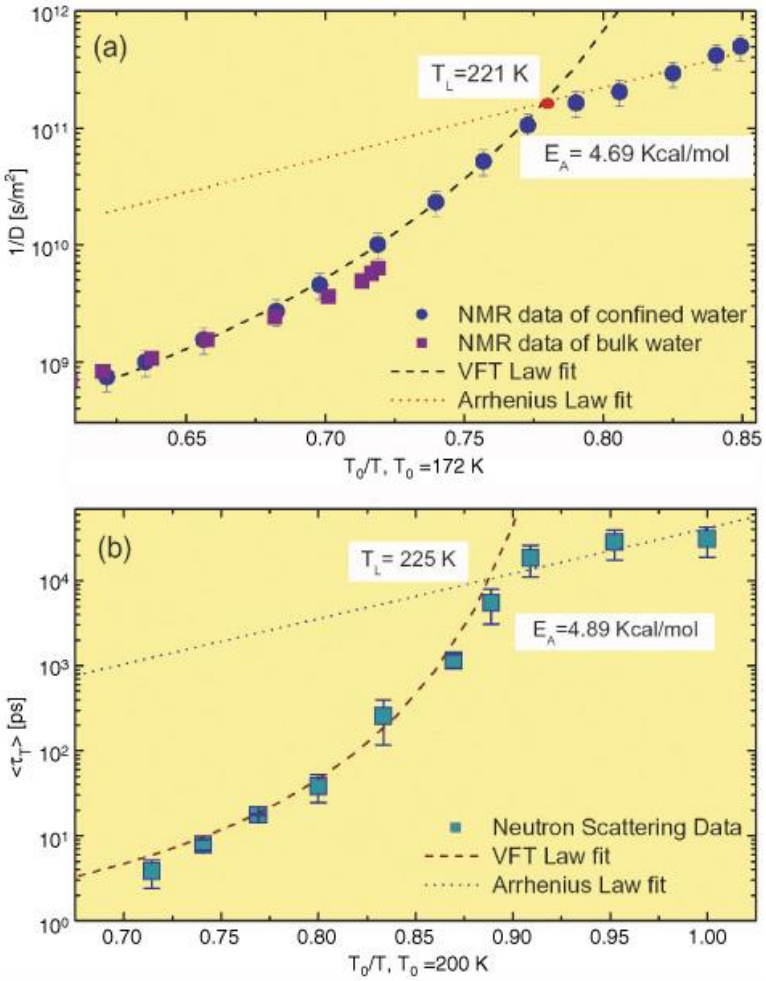

Figure 1.12 (a) The inverse of the diffusion coefficient versus 1000/*T* as measured by NMR for water confined in 1.4 nm MCM-41. (b) Translational correlation time of water confined in MCM-41 samples in 1.4 nm pores versus 1000/*T* as measured by QENS [69, 84].

Quasielastic neutron scattering (QENS) and nuclear magnetic resonance (NMR) spectroscopy are two techniques that can be used to probe the dynamics of a material. **Figure 1.12 (b)** demonstrates the correlation time of water molecules obtained from QENS experiments on water confined in an MCM-41 samples. In this plot, there is a dynamic crossover temperature T_L at $225\ K$, which was found from the intersection of two different types of correlation time fittings (Vogel-Fulcher-Tammann (VFT) fitting and the Arrhenius fitting, which will be further discussed in Section xx) [85, 86]. Meanwhile, the diffusion coefficient of water in the MCM-

41measured from pulse gradient NMR also showed a similar transition temperature at $223 \pm 2\ K$ (see **Figure 1.12 (a)**). The Chen's group considered such a dynamic transition as related to the second critical point in LLPT theory. 225 K is the temperature where the fluctuation of the two liquids (VFT and Arrhenius) reaches a maximum by the definition of Widom line [69, 84].

However, the claim remains in question. Vogel's group shows for water confined in MCM-41, it has step crystallization below 250 K, the observed transition and other dynamic changes may be induced by micro-crystallization. These experiments and active discussions bring up following questions in our research:

(1) Is the water homogeneous or heterogeneous naturally?

(2) Is the LDL existing at low temperature region if water is not freezing?

(3) Is the dynamic crossover induced by micro-crystallization instead of LLPT?

(4) How does the surface effect or nanoconfinement effect affect the properties of water?

(5) What is the mechanism for water's glass transition?

My main focus in this dissertation is trying to understand the physics behind the anomalous behavior of water. To access the "no man's land", we applied water confined in hydrophobic surfaces. To investigate the properties of confined water, we performed DSC and NMR methods to study the thermodynamic and dynamic properties of water.

In our experiment, most importantly, we captured the macroscopic heterogeneity of water at room temperature and proved LDL is a stable liquid state at low temperature. We also noticed, above 200 K, there is no crystallization for supercooled confined water and has a dynamic crossover temperature at around 225 K which is the same as water confined in hydrophilic pores. This is a strong evidence to prove the dynamic crossover is not induced by micro-crystallization or surface effect but the intrinsic property of bulk water. At 190 K, we observed a rotational

glass transition of water and a growth of amorphous ice. Finally, we found there is a glass transition at 150 K for confined water which is induced by the interfacial water.

CHAPTER 2 EXPERIMENT METHOD, SAMPLE PREPARATION AND CHARACTERIZATION

2.1 Nuclear Magnetic Resonance (NMR)

Studying the structure and dynamics of a material is generally performed using X-ray diffraction (XRD) [25, 87, 88], rheology, or various optical methods [89, 90]. However, these techniques can only measure bulk material properties. For confined systems, X-ray fails to penetrate the surface. shear stress cannot be applied on the material in the pores, optical methods only give local structure information. In contrast, NMR is uniquely suited for probing local structures and dynamic properties of liquids or gases inside porous media, as long as it contains nuclear spin [91].

In this dissertation, we applied NMR to probe the size distribution of activated carbon micropores (< 2 nm), as well as to investigate the state of water confined in the nanopores, including the dynamics and local structure [92]. Therefore, it is necessary to review some of the basic concepts of NMR prior to its application in this research.

2.1.1 Magnetization

Materials are made of atoms. Atoms have electrons and nuclei. Every nucleus has mass, electric charge, magnetism, and spin. The magnetism of a nucleus can interact with a magnetic field. The spin of nucleus acts like it is spinning around, rotating in space like a planet. Nuclear magnetism and nuclear spin are sensitive to the molecular environment, for example, the surrounding electrons, or other spins from the same molecule. These properties provide scientist

with an excellent tool for spying on the microscopic and internal structure of objects without destructivity.

Table 2.1 Gyromagnetic ratio of the nuclei used in NMR spectroscopy [93]

Nucleus	**Spin**	**Natural Abundance (%)**	$\boldsymbol{\gamma}$ $(\mathbf{10^6\ rad \cdot s^{-1} \cdot T^{-1}})$	$\frac{\boldsymbol{\gamma}}{\mathbf{2\pi}}$ $(\boldsymbol{MHz \cdot T^{-1}})$
^{1}H	1/2	99.9885	267.513	42.576
^{2}H	1	0.015	41.066	6.539
^{13}C	1/2	1.07	67.262	10.705
^{19}F	1/2	100	251.662	40.053

Note: γ is gyromagnetic ratio

A rotating object possesses a quantity called angular momentum. In quantum mechanics, angular momentum is quantized as $I\hbar$, in which I is the spin quantum number and $\hbar$ is Planck's constant. The dipolar magnetic momentum can be defined as $\mu = \gamma I\hbar$, where γ is the gyromagnetic ratio. When an external magnetic field (B_0) is applied to a nuclear state with spin I, it will degenerate to $(2I + 1)$ sublevels featuring magnetic quantum numbers (m) of $-I, -I + 1, \ldots I - 1, I$. **Table 2.1** lists the spin number and gyromagnetic ratio for selected nuclei. For example, ^{1}H has a nucleus of spin ½. When B_0 is applied, the equilibrium energy state will split into two different energy states, featuring an energy (E_m) of $\mu B_0 = -\gamma I\hbar B_0 = -m\gamma\hbar B_0 = \pm\frac{1}{2}\gamma\hbar B_0$ (see **Figure 2.1**). The spins will possess along the external field axis with the Larmor frequency ω_0 ($\omega_0 = -\gamma B_0$).

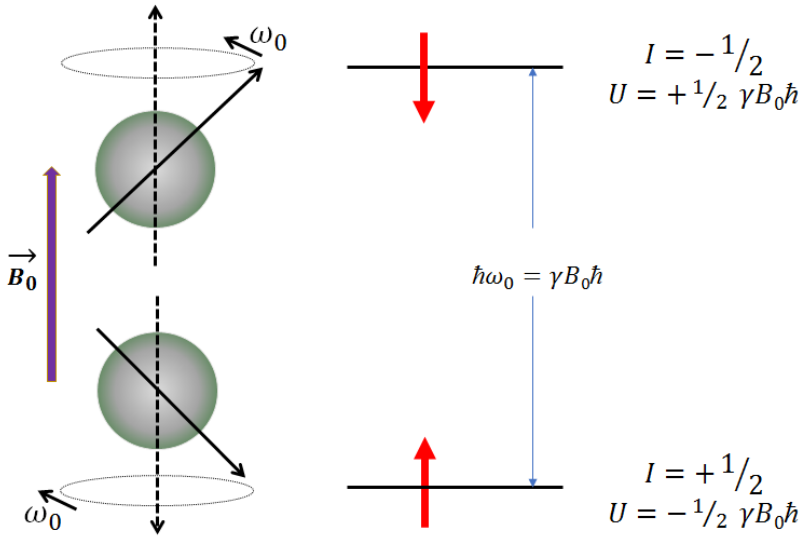

Figure 2.1 Illustration of a ^{1}H nucleus in an external magnetic field [93]

In thermal equilibrium, the probability for a spin to remain at the split energies follows the Boltzmann distribution $P_m \propto \exp(-E_a/k_BT)$, in which E_a is the degeneracy energy and k_B is the Boltzmann constant. The net magnetization, M_0, for N non-interacting spins follows Eq. (2.1):

$$M_0 = N\gamma\hbar \frac{\sum_{m=-I}^{I} m exp\left(\frac{m\gamma\hbar B_0}{k_BT}\right)}{\sum_{m=-I}^{I} \exp\left(\frac{m\gamma\hbar B_0}{k_BT}\right)} \ . \tag{2.1}$$

At the high temperature limit, $\gamma\hbar B_0 \ll k_BT$, Eq. (2.1) can be simplified to:

$$M_0 = \frac{N\gamma^2\hbar^2 B_0 I(I+1)}{3k_BT}. \tag{2.2}$$

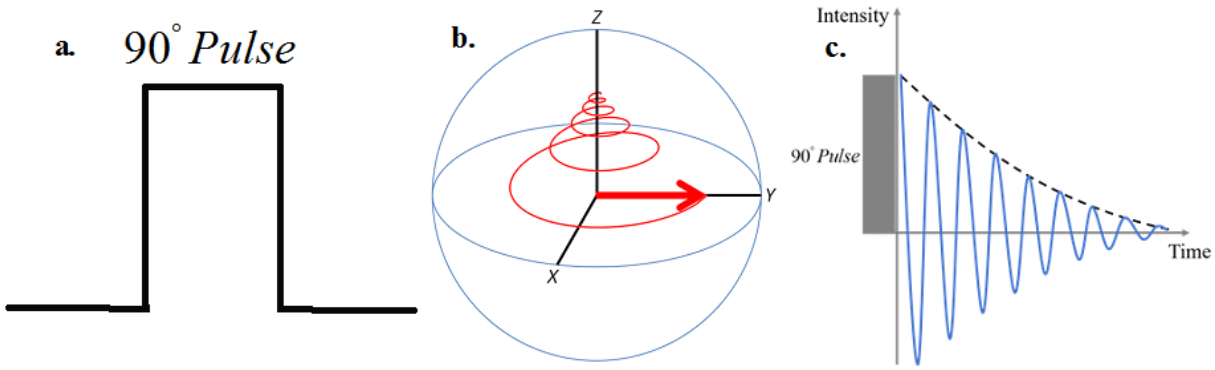

Figure 2.2 Schematic illustrations of the (a) external field perturbation of an RF pulse, (b) the net magnetization precession after the RF pulse, and (c) the FID

When an external oscillation field at the Larmor frequency (ω_0) is applied perpendicular to the static field, the net magnetization will tip away from the z-direction. After perturbation, the net magnetization will start precession along the static field (B_0) as a single spin and generate an electromagnetic signal that can be detected by a radio-frequency (RF) sensor. Such a signal is referred to as the free induction decay (FID). (see **Figure 2.2 (c)**)

2.1.2 Relaxation

There are two types of relaxation that can describe the interactions between spins: longitudinal (T_1) and transverse (T_2). The Bloch equations describe the time evolution of the net magnetization in a classical picture in three-dimensional space (x, y, and z) [91, 94]:

$$\frac{dM_x}{dt} = \gamma(\boldsymbol{M}\times\boldsymbol{H})_x - \frac{M_x}{T_2}$$

$$\frac{dM_y}{dt} = \gamma(\boldsymbol{M}\times\boldsymbol{H})_y - \frac{M_y}{T_2} \qquad (2.3)$$

$$\frac{dM_z}{dt} = \gamma(\boldsymbol{M}\times\boldsymbol{H})_z + \frac{M_0 - M_z}{T_1} \quad .$$

When an RF pulse at its Larmor frequency is applied to the nucleus, the magnetization (M) will be tipped away from its thermal equilibrium value (M_0). After such perturbation, the net

magnetization tends to move back to its equilibrium state. The temporary magnetization on the x, y and z directions can be described by:

$$M_x = M_0 \sin(\omega t) \exp(-t/T_2)$$

$$M_y = -M_0 \cos(\omega t) \exp\left(-\frac{t}{T_2}\right) \tag{2.4}$$

$$M_z = M_0(1 - \exp(-t/T_1))$$

In the longitudinal direction, M_z associates with the energy transfer from the spin to the surroundings, which is also called the lattice. Therefore, T_1 is also referred as the spin-lattice relaxation. On the other hand, in the transverse plane, T_2 describes the amount of time that the spins will lose their coherence. There is no energy transferred during the spin-spin relaxation time.

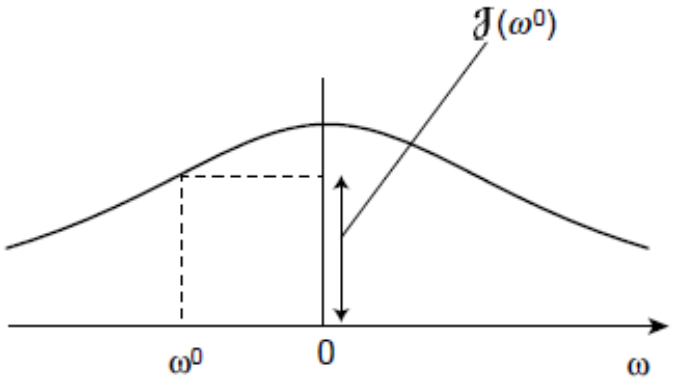

Figure 2.3 Fourier Transform of spectral density $J(\omega^0)$ in terms of frequency ω [93].

In liquids, for a spin ½ system, the main relaxation mechanism is the dipolar interaction through space between two spins. Both rotation and translation result in the fluctuation of the local field [95]:

$$\frac{1}{T_1} = \frac{3}{2}\gamma^4 \hbar^2 I(I+1)[J^1(\omega) + J^2(\omega)] \tag{2.5}$$

$$\frac{1}{T_2} = \gamma^4 \hbar^2 I(I+1)\left[\frac{3}{8}J^0(0) + \frac{15}{4}J^1(\omega) + \frac{3}{8}J^2(2\omega)\right] \tag{2.6}$$

in which the tensor *J* is the Fourier transformation of the spectral density of the dipolar interaction as shown in **Figure 2.3**. And could be described by Eq. (2.7):

$$J^0 = \frac{1}{b^6}\frac{24}{15}\frac{\tau}{1+\omega^2\tau^2}$$
$$J^1 = \frac{1}{b^6}\frac{14}{15}\frac{\tau}{1+\omega^2\tau^2} \quad (2.7)$$
$$J^2 = \frac{1}{b^6}\frac{16}{15}\frac{\tau}{1+\omega^2\tau^2}$$

in which b is the distance between two spins and τ is the correlation time. For ^{1}H and other ½ spin systems, this leads to the expressions of T_1 and T_2 as:

$$\frac{1}{T_1} = \frac{3\gamma^4\hbar^2}{10b^6}\left[\frac{\tau}{1+\omega^2\tau^2} + \frac{4\tau}{1+4\omega^2\tau^2}\right] \quad (2.8)$$

$$\frac{1}{T_2} = \frac{3\gamma^4\hbar^2}{20b^6}\left[3\tau + \frac{5\tau}{1+\omega^2\tau^2} + \frac{2\tau}{1+4\omega^2\tau^2}\right] \quad (2.9)$$

Note: in SI unit, right hand side equation should times $\left(\frac{\mu_0}{4\pi}\right)^2 = 10^{-14}$

From **Eq. (2.8) (2.9),** it is clear to say that T_1 relaxation time is strongly depending on the external magnetic field B_0 ($\omega_0 = -\gamma B_0$) and T_2 relaxation time is less or zero dependent on B_0 (see **Figure 2.4**)

For a fixed external magnetic field B_0 and known spin, such as ^{1}H, the correlation time τ and T_1, T_2 could be plotted in **Figure 2.4.** Along the correlation time τ axis, lightly speaking, it is divided into three main regions: small molecule, large molecules/proteins/polymers, and solids. The shorter value of correlation time indicates faster motion or smaller size of molecules and longer correlation time represents slower motion or larger size of molecules. For small molecules, such as water, alcohol, due to fast motion limit, $T_2 \approx T_1$, which is defined as fast motion region in **Figure 2.4**. In the contrast, macromolecules and polymers, $T_2 < T_1$ which is

categorized in slow motion region. For solids, $T_2 \ll T_1$, due to the rigid lattice of solid structure. It shows the advantage that using T_1, T_2 relaxation time and correlation time can distinct different type of species, determine the motion of molecules, estimate the molecular sizes and roughly achieve liquids viscosity.

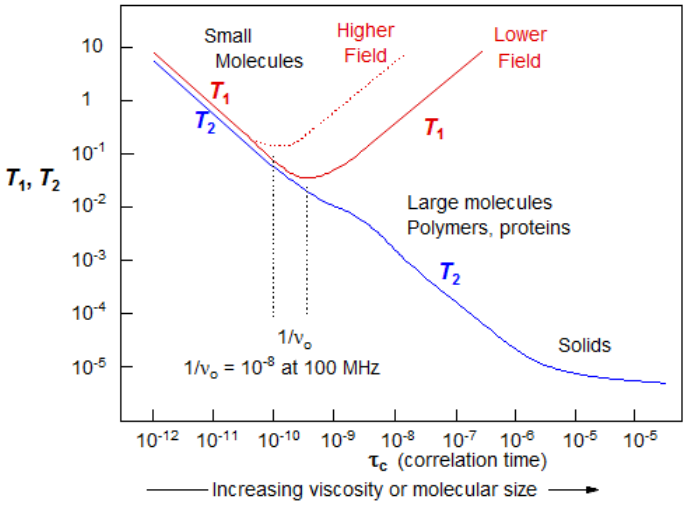

Figure 2.4 Illustration of correlation time τ versus T_1, T_2. The red solid line and dashed line represent T_1 value in low external field and high external field. The blue solid line represents T_2 value [92]. (T_2 is almost zero depend on Larmor frequency ω_0)

2.1.3 NMR Measurements

FID measurements

The proton (^{1}H) NMR spectra were recorded using a Bruker Avance III spectrometer and a Bruker PH MASDVT 500W2 BL4 N-P/H probe on a 500 MHz magnet (11.7 T). The temperature was controlled within ± 0.2 K by heating evaporated liquid nitrogen from 77 K to the target temperature. A single pulse sequence was applied during the measurements. The free induction decay was extrapolated to $t = 0$ in order to obtain the total intensity. The intensity was also corrected by Currie's Law ($1/T$) and the Q factor of the equipment (see **APPENDIX B**).

It is important to emphasis that the RF pulse length we applied in our experiments is $0.5us$ much shorter than $4.5us$ which is the ^{1}H 90° pulse for 500 MHz system at highest power level.

The reason we chose $0.5us$ instead of $4.5us$ is we want to excite as many spins as possible especially at low temperatures. For a $0.5us$ RF pulse length, it could excite and capture the information of spins located in a large frequency region of 0.6 MHz ($1/(\pi(0.5us)$) instead of 0.06 MHz. Such short RF pulse will tip the net magnetization M_0 a small angle away from the z axis, so it is called small-angle measurement.

^{1}H spin-lattice relaxation measurements

To study the spin-lattice relaxation, we applied an inversion-recovery pulse sequence of $180^o_x - t - 90^o_y$, in which the duration time t was varied from 5 μs to10 s (see **Figure 2.5**).

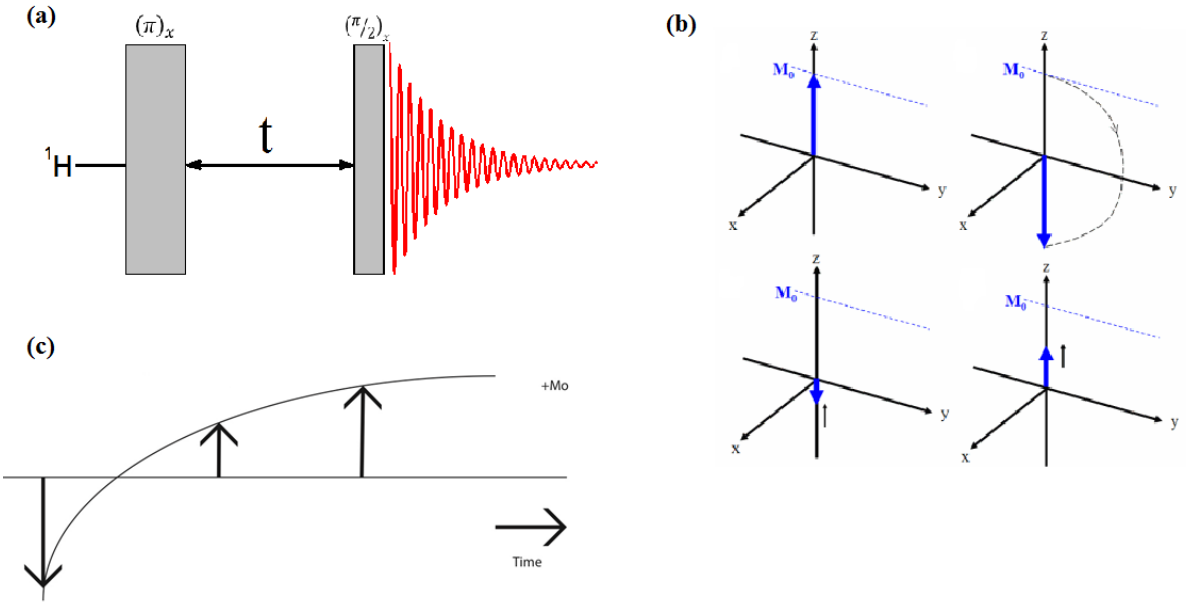

Figure 2.5 (a) Illustration of inversion-recovery pulse (b) Magnetization varies by the pulse and evolution (c) Magnetization growth for different *t* value.

The function of the inversion pulse (π_x in **Figure 2.5 (a)**) is to flip the longitudinal magnetization (M_0) to the opposition direction of the main magnetic field (B_0) (see **Figure 2.5 (b)**). It inverses the population of the spins to $-\boldsymbol{I_Z}$ direction. During the delay time t, the spins are allowed to relax and seek to re-establish magnetization along $\boldsymbol{I_Z}$ direction until $(\pi/2)_x$ applied. During the spin relaxation time, it releases energy to the surrounding environment which is called

lattice conventionally. The magnitude and sign of the signal in the acquired FID depend on the longitudinal relaxation rate of each spin and the during time set in between two pulses (see Figure 2.5 (c)). If t systematically varies, the FID signal of t follows Eq. (2.10)

$$\frac{M(t)}{M_0} = 1 - 2e^{-\frac{t}{T_1}} \tag{2.10}$$

Since T_1 relaxation is dominated by the intramolecular dipole-dipole interaction in liquids, the rotational correlation time, τ, could be calculated from **Eq. (2.8)**. γ in Eq. (2.8) is the gyromagnetic ratio of the proton, b is the distance between the two hydrogen atoms in the molecule (0.156 nm for H_2O), and ω_0 is the Larmor frequency ($2\pi\times500$ MHz at 11.7 T).

^{1}H spin-spin relaxation measurements

To study the spin-spin relaxation, we applied two types of pulse sequences performed in this thesis: Hahnecho pulse [96] and Carr-Purcell-Meiboom-Gill (CPMG) pulse [97].

The NMR signal decays following an initial RF pulse due to both spin relaxation and inhomogeneous in field space which cause spins in the sample to precess at different rate. The relaxation is an irreversible loss of magnetization. However, the inhomogeneous dephasing can be removed by an inversion pulse that inverts the magnetization vectors. If the inversion pulse is applied following a duration time t of dephasing, the inhomogeneous evolution will rephrase to form an echo after waiting for the same time t. (see Figure 2.6(F))

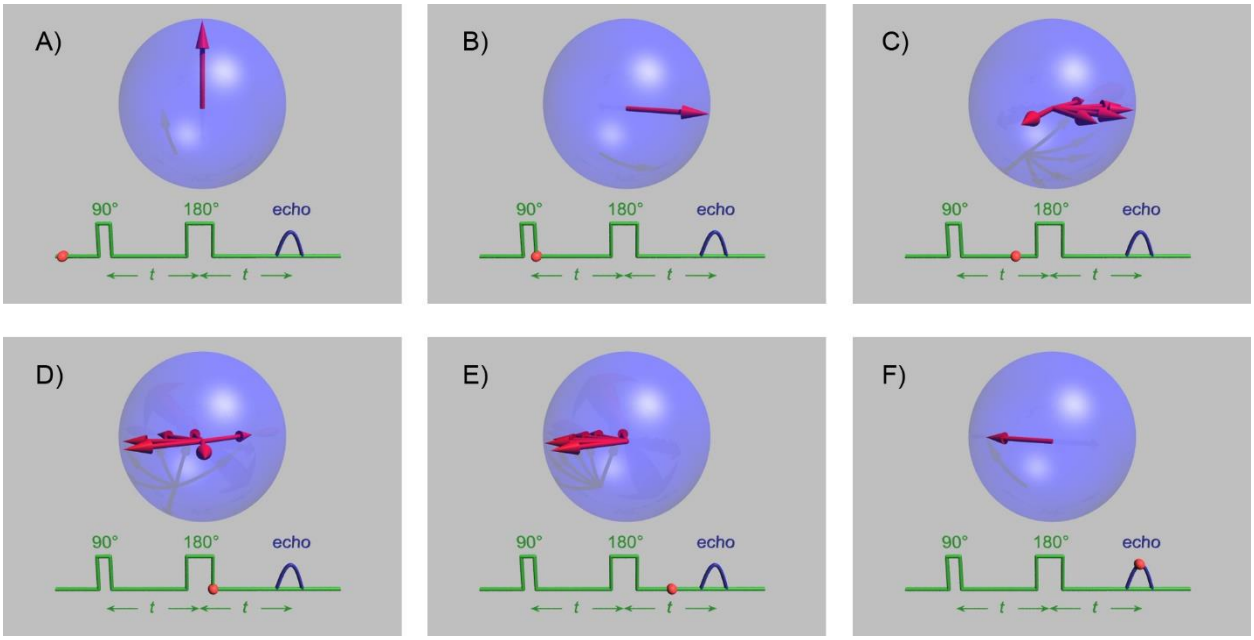

Figure 2.6 (A)-(F) Illustration of Hahnecho pulse sequence and dephasing and refocusing process for spins step by step [97]

Note: (A)-(B) The vertical red arrow represents the net magnetic moments of a group of spins in the rotation frame before and after a 90° RF pulse. (C) due to local magnetic field inhomogeneities, some spins slow down due to lower local magnetic field strength which are at the tail behind, while some speed up due to higher local magnetic field which are ahead of others. The heterogeneity of filed makes spins decay. (D) A 180° pulse added after spins diphase in time t interval makes the slower spins ahead and faster spins behind. (E) Similarly, the faster spin will catch up with slower spins after time t. (F) Complete refocusing has occurred.

The Hahnecho method could remove the inhomogeneous field effect, however, the random translational diffusion during time t cannot be ignored. For spins diffuse to another field strengths, the inversion pulse cannot refocus these spins and will contribute an extra decay during two pulses. In 1954, Carr and Purcell first developed the Hahnecho method [97] by applying a sequence of inversion pulses with a sufficiently short time interval t that could greatly reduce the diffusion effect. Later on, Meiboom and Gill in 1958 improved this approach by using better electronics to generate coherent pulses with the initial 90° pulse shifted in phase by 90° relative to the subsequent 180° pulses [98].

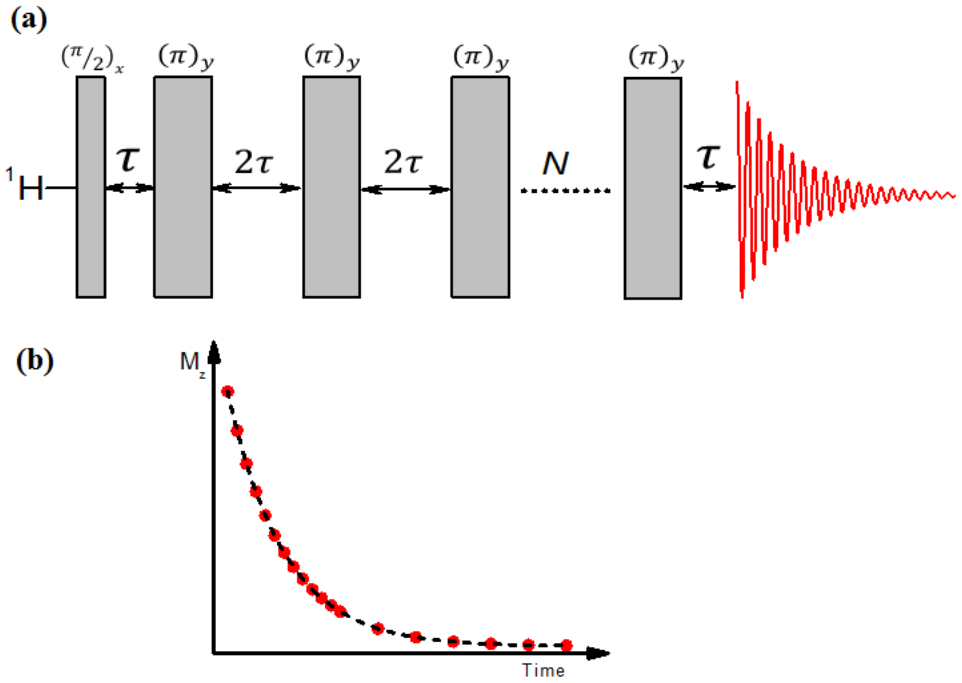

Figure 2.7 (a) Illustration of CPMG pulse (b) Magnetization versus time

Figure 2.7 (a) is a simple illustration of CPMG pulse with single phase setup. The final signal is variant by the number of 180° (n) in the pulse. The relaxation time of the spins for a fixed n is. The spin-spin relaxation time T_2 follows Eq. (2.11)

$$M(t) = M_0 e^{-t/T_2} \tag{2.11}$$

Hole-burning experiment

In principle, the hole-burning experiment is to study the motion of spins in a highly inhomogeneous filed [99, 100]. In this thesis, we applied the hole-burning experiment to investigate the reason of spectrum line broadening at low temperature. Field inhomogeneity is one of the mechanism of line broadening. Strong dipole-dipole interaction and isotropic rotational motion are also considered as important reasons. To understand the dipolar interaction and cooperativity of spins is crucial to this research.

The hole-burning sequence, employed in the NMR experiments starts with a long, low-power pulse of length P1, to irradiate the spin system in a narrow frequency band. The spectrum of this pulse is the $sinc$ function with bandwidth $\Delta\Omega_{\mathrm{HB}}/2\pi \approx 1/P1$. It determines the bandwidth of the hole pulse and correlates with the sizes of the spatial domain of interest. Such RF pulse is called selective pulse. After applying the selective pulse, it excites a group of spins locating in the region $\omega_0 \mp 1/2P1$ where ω_0 is the center frequency set in the transmitter (SFO1). Such excited spins are tipped away from their equilibrium position where the magnetic moment is along $\boldsymbol{I_Z}$. The other spins remain parallel to $\boldsymbol{B_0}$. Following a recovery time D1, a broad-band detection sequence for longitudinal magnetization is applied with a "hard" high power pulse and a "hard" pulse length $P2 \ll P1$. The frequency band width of the "hard" pulse $\Delta\Omega/2\pi \approx 1/P2$ is larger than the selective hole bandwidth $\Delta\Omega_{HB}/2\pi$. So, more spins should be excited by the detection pulse. If the hole spins are independent with the other spins, under the action of the detection pulse sequence, the magnetization M_{HB} from the hole pulse selected spins contributes little to the signal. Only the magnetization M_{Other} from the other unselected spins dominates the signal. Otherwise, M_{HB} and M_{other} will both contribute to the final signal.

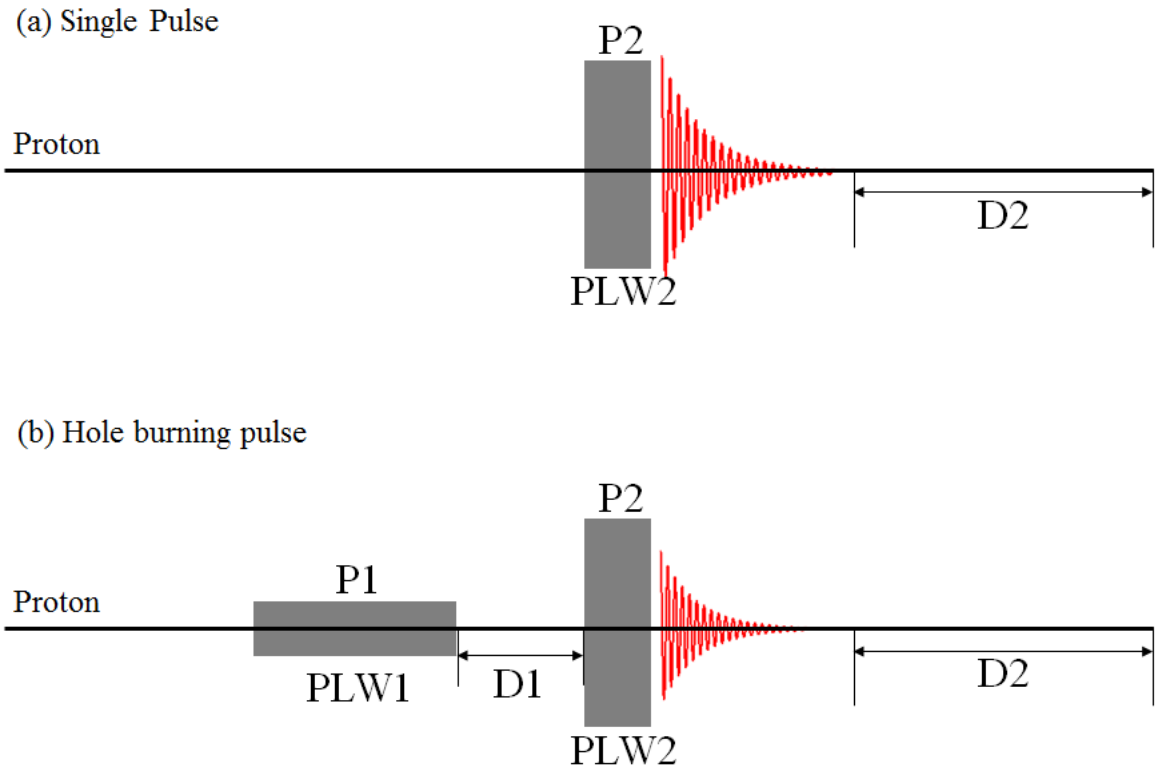

Figure 2.8 (a) Illustration of single pulse (b) illustration of hole burning pulse
Note: P1, P2 are RF pulse lengths; PWL1, PLW2 are RF power level; D1 is the duration time between first and second pulse in hole burning pulse; D2 is the recovery time (last delay) for spins back to the equilibrium state (D2≥ $5T_1$)

2.2 Differential Scanning Calorimetry (DSC)

2.2.1 Principles of DSC

DSC is a thermoanalytical technique used to measure the specific heat capacity of a material by measuring the amount of heat required to increase the temperature of a sample and reference. For a heat flux DSC, the sample and reference are heated by a single furnace (see **Figure 2.9**), and the signal that is measured is the temperature difference between the sample (T_s) and the reference (T_r). The heat flow is calculated based on this temperature difference.

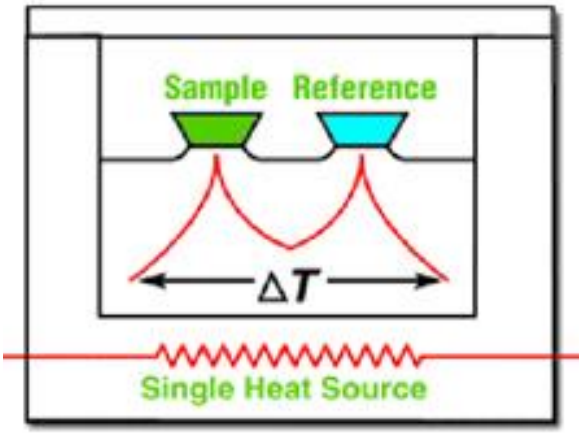

Figure 2.9 Schematic illustration of a heat flux DSC, in which $\Delta T = T_r - T_s$

In thermodynamics, the specific heat capacity is the response function of enthalpy changed by temperature at a fixed pressure, see **Eq. (2.12)**:

$$C_p = \frac{\partial H}{\partial T}\Big|_p = \frac{1}{m}\frac{\delta Q}{dT} = \frac{1}{m}\left[\frac{\frac{\Delta Q}{t}}{\frac{\Delta T}{t}}\right] \tag{2.12}$$

in which m is the mass of the sample, $^{\Delta Q}/_{t}$ is the heat flux measured directly from the DSC, and $^{\Delta T}/_{t}$ is the heating rate.

Determining phase and glass transitions are the two main uses of DSC. Before the sample undergoes a physical transformation, the temperature difference (ΔT) is constant for the system. When the sample undergoes an exothermic or endothermic physical transformation, ΔT will change by applying a fixed power output. By observing the heat flow between the sample and the reference, the DSC technique can measure the amount of heat absorbed or released during such a transition. Compared to heat compensated DSC, heat flux DSC has higher resolution to observe more subtle material changes and its baseline is more stable [ref].

2.2.2 Fragility

In glass physics, fragility is an index to characterize how rapidly the dynamics of a material slow down as it is cooled toward its glass transition temperature [101]. Liquids with high fragility are called fragile liquids, which have a relatively narrow glass transition temperature range. For those liquids with low fragility are classified as strong liquids, which have a broader glass transition temperature range (Fig 2.10). Angel [101-104] was the first to propose this classification and defined the fragility index (m) as a slope of viscosity (or relaxation time, τ) for a material at a temperature near its glass transition temperature T_g (Eq. 2.13)

$$m = \left(\frac{\partial \log_{10} \eta}{\partial (T_g/T)}\right)_{T=T_g} = \frac{1}{ln10}\left(\frac{\partial \ln \eta}{\partial (T_g/T)}\right)_{T=T_g} = \frac{T_g}{\ln 10}\left(\frac{\partial \ln \eta}{\partial T}\right)_{T=T_g} \quad (2.13)$$

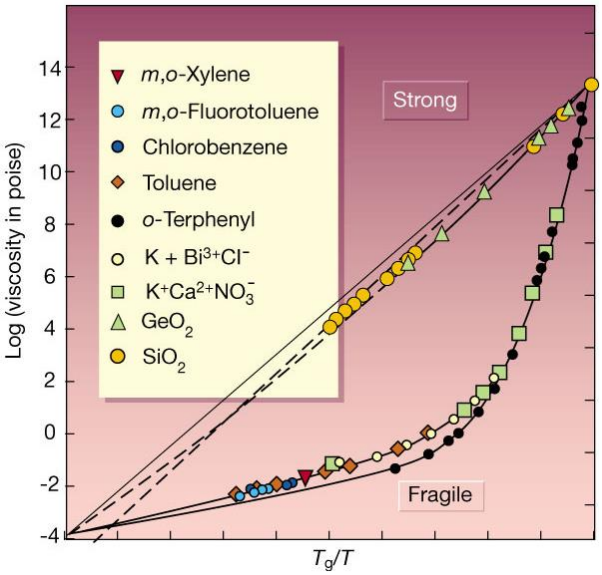

Figure 2.10 Plot of viscosity in logarithmic scale versus T_g/T [104]

As shown in **Figure 2.10**, liquids that display linear behavior for the plot of $\log(\eta)\ vs. T_g/T$ are classified as strong liquids, which follow the Arrhenius law, $\eta = \eta_0 exp(-\frac{E_g}{RT})$. For strong liquids, m can also be derived from Eq. (2.13) to give Eq. (2.14):

$$m = \frac{E_g}{\ln 10\ RT_g}. \tag{2.14}$$

Meanwhile, liquids that have a non-linear relationship of $\log(\eta)\ vs. T_g/T$ are categorized as fragile liquids (**Figure 2.10**), which follow the VFT law, $\eta = \eta_0 exp(-\frac{E_g}{R(T-T_0)})$, in which E_g is the activation energy for structure relaxation at T_g, and T_0 is the ideal glass transition temperature for the fragile liquid.

Based on Angel and Moynihan's work [101, 105], the fragility index m can be estimated from DSC measurements. Early study of glass transitions [13, 105] suggested that the dependence of the cooling rate (Q) of T_g obeys an exponential law (Eq. 2.15):

$$Q = Q_0 \exp\left(\frac{-E_g}{RT_g}\right) \tag{2.15}$$

in which Q_0 is a constant. Different cooling and heating rates will result in different onset temperatures for T_g. Selecting a standard cooling/heating rate (Q_s) to achieve a standard T_g provides a reference glass transition temperature (T_g^S). Then by choosing another cooling/heating rate (Q) and obtaining that corresponding T_g, it is possible to compare it with the reference T_g^S value and take the logarithm of the Q/Q_s ratio to derive Eq. (2.16):

$$log\frac{Q}{Q_s} = \frac{E_g}{\ln 10\ R}\left(1 - \frac{T_g^S}{T_g}\right) = m\left(1 - \frac{T_g^S}{T_g}\right) \tag{2.16}$$

If we plot $\log(Q/Q_s)$ versus $(1 - T_g^S/T_g)$, the slope represents the fragility index m.

2.3 Material Characterization and Experiment Preparation

2.3.1 Material Preparation

In our experiments, activated carbon is the confinement media and was prepared from polyether ether ketone (PEEK). The PEEK pellets were carbonized at 900 ^oC for 30 min in 99.5% Argon atmosphere at a ramping rate of 45 ^oC/min starting from room temperature. After cooling the sample back to room temperature, the carbonized material was ground into powder featuring an average particle diameter of 0.5 mm. The pulverized sample was activated at 900 ^oC using water vapor and Argon gas as a carrier flow. The activation time was varied to achieve different burn-off (BO) percentages, defined as the ratio of mass reduction during activation to the mass of the starting carbon material. Longer activation times led to higher BO values and larger micropores. The pore size distributions of the different BO samples were characterized using the nucleus independent chemical shift NMR porometry method which will discuss in the next section.

2.3.2 Nucleus Independent Chemical Shift (NICS) Effect to Characterize Pore Size

In this thesis, we applied ^1H magic angle spinning (MAS) NMR method at room temperature to characterize the nanopore size quantitatively by NICS effect [106-108]. NICS is an

aromatic ring current effect on the local magnetic field experienced by the nuclear spin of the probe atom. It is not related to chemical bond and is nucleus independent.

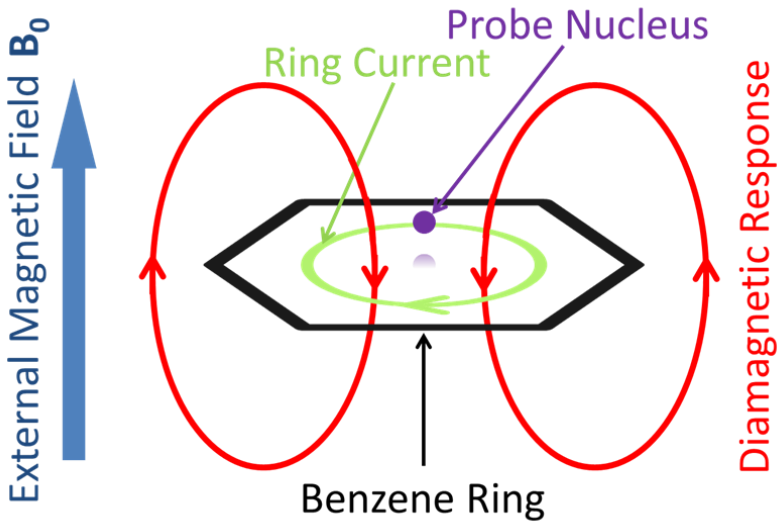

Figure 2.11 Illustration for a benzene molecule and ring current in an external field B_0

Figure 2.11 shows an example of NICS effect on a benzene molecule. The benzene molecule with π electrons inducing a ring current in the external magnetic field gives a diamagnetic response to the file plane of the benzene ring and courses an upfield chemical shift. The mechanism of chemical shift is dominated from diamagnetic and paramagnetic effects from the ring currents associated with the aromatic and antiaromatic compounds. So, it is independent with the probe atoms.

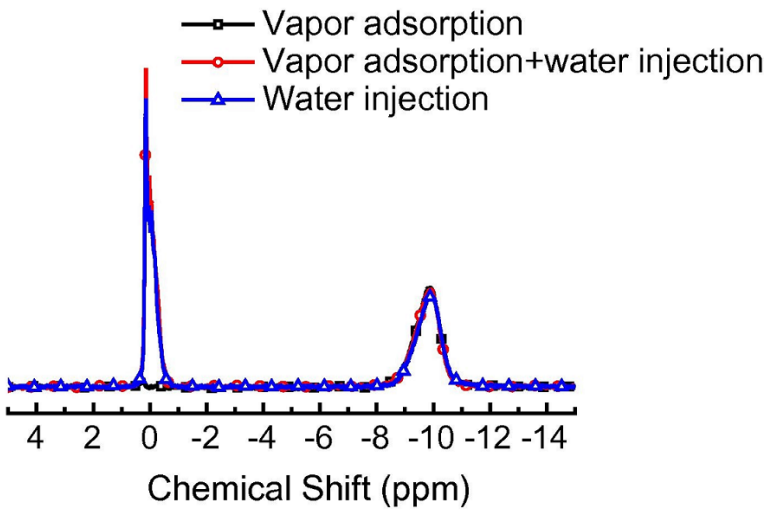

Figure 2.12 ^{1}H NMR magic angle spinning (MAS) spectra of water in P-0 AC with different filling condition: black line represents vapor adsorption, red line represents partial vapor adsorption and injecting water, blue line represents absorption by syringe injection water [109].

The activated carbon (AC) has hexagonal structure with the ring current, as expected, there has a NICS effect in AC. Two well-resolved peaks are clearly observed in the ^{1}H NMR spectrum (see **Figure 2.12**). The ^{1}H chemical shift of the left peak is due to water stored in intergranular space or mesopores. The right peak is associated with water adsorbed in the nanopores. The upfield shift of the right peak with respect to the left peak is due to NICS effect of AC. From NMR spectra comparing three different filling methods, it shows there is no difference between syringe injection and vapor adsorption. The chemical shift $\delta(r)$ is a function of distance between the probe atom center and the surface of carbons which achieved from Density Function Theory (DFT) calculation.

As shown in **Figure 2.13**. A summary of the center to center or surface to surface mean pore sizes with different burn off percentage samples are listed in **Table 2.2**.

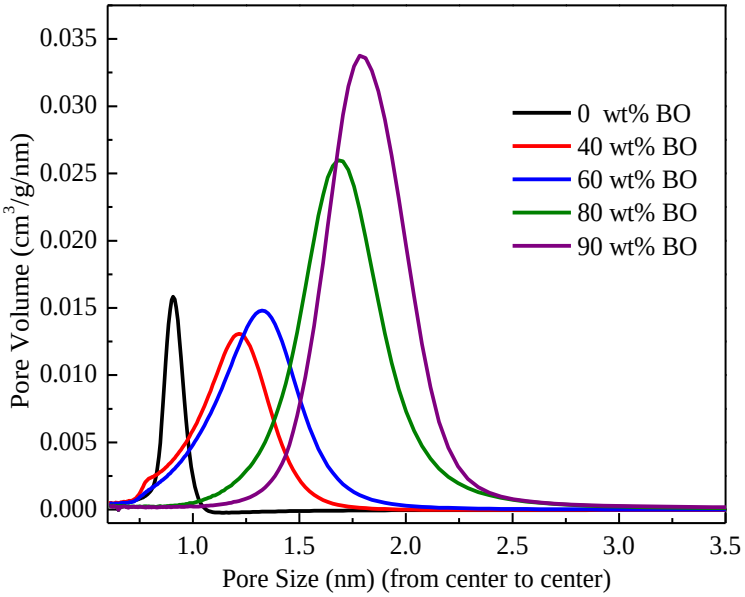

Figure 2.13 Pore size distribution for different BO PEEK samples

Table 2.2 List of activated carbon sample sizes.

BO %	Pore size *d* (nm) center to center	Pore size *d**(nm) surface to surface
0	0.9	0.56
40	1.21	0.87
60	1.42	1.08
80	1.64	1.3
90	1.94	1.6

2.3.3 DSC Sample preparation

DSC measurements were carried out on a Q200 DSC (TA Instruments) for temperatures ranging from 120 K to 310 K. Activated carbon samples were put into a vapor chamber to absorb water until the nanopores were filled, which was defined as the sample weight no longer increased by the set time. The samples were then placed in an aluminum cell pan and hermetically sealed to prevent water evaporation. The same cooling and heating is applied for each DSC experiment trail. To determine C_p of the confined water in the activated carbon, the background contribution from a dry activated carbon control was subtracted from the

thermograms during data analysis. To study T_g of the confined water in the activated carbon samples, 6 different cooling/heating rates (Q) were applied.

CHAPTER 3 HETEROGENEITY OF WATER: EVIDENCE OF HIGH-DENSITY LIQUID AND LOW-DENSITY LIQUID

3.1 INTRODUCTION

Water in the confinement system plays a crucial role in various applications such as protein folding and drug delivery [110-112], electron storage mechanism in the supercapacitors [113]. Most importantly, confined water shed the light to study the bulk water properties in details. Confinement systems reducing the dimension of bulk system could slow down the dramatic change during phase transition and make it possible to take a snapshot to observe the structure details [114]. Another notable effect of confinement system is for water under nanoconfinement, the freezing temperature greatly suppressed to much lower temperature region beyond the bulk homogeneous nucleation temperature T_H [70, 82, 115, 116]. It provides an experimental access to investigate the water thermodynamic properties in "no man's land" and to help further understand the anomalies of water such as maximum density at 4 ℃ [71, 117].

Activated carbon with tunable pore sizes prepared in our lab provides hydrophobic surfaces for studying the properties of nanoconfined water at ambient pressure from 290 to 140 K. In this chapter, we mainly use burn off 90% activated carbon (P-90 AC) which has average pore size 1.6nm from carbon surface to surface as the nanoconfinement media. P-90 AC could hold at least 5 layers of water, the specific heat capacity (C_P) of water confined in P-90 AC is the same as bulk water at 25℃, 4.12 $\mathrm{kJ \cdot K^{-1} \cdot g^{-1}}$ which indicates the total confined water behaves like bulk water at high temperature and in atmospheric pressure. From NMR relaxation

experiments and MD simulations, we found at room temperature, confined water has “two phases”, one is dominated by high-density liquid (HDL) structure which is a dense-packing structure, the other is contributed by low-density liquid (LDL) structure which is a more tetrahedral structure [25]. This is a key point to understand the water unique properties: water is a heterogeneous liquid in contrast of a homogeneous liquid.

The following sections will guide the investigation of water properties by applying NMR and DSC and arrive a deeper understanding of water itself.

3.2 EXPERIMENTS SET UP

The activated carbon sample is prepared from organic precursor PEEK and characterized by NMR porometry method (see **Chapter 2.3.2**). The main hydrophobic porous material used in our experiments are P-90 AC sample. To support our discoveries of intrinsic bulk water properties, we also run the same experiments on water confined in different pore sizes, P-80 AC which has pore size 1.3 nm from surface to surface and in P-94 AC which has 1.8 nm pore size from surface to surface but most of the pores are collapsed (pore structure are more complicated).

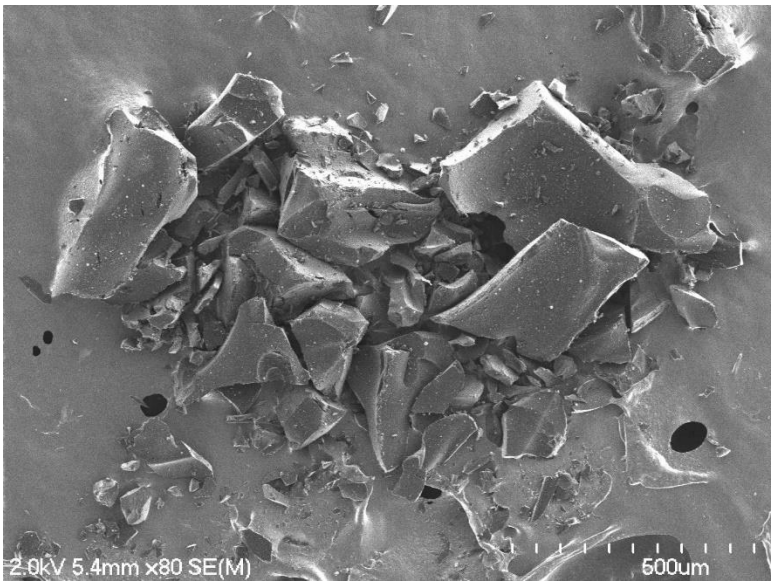

Figure 3.1 SEM image of dry activated carbon sample of P-90. The scalebar is 500 μm, each subdivision is 50 μm

Figure 3.1 is a scanning electron microscopic (SEM) image of a dry P-90 sample. ^{1}H NMR shows these carbonized sample at 900℃ have proton residue 0.1%.

The DSC experiments run for dry activated carbon, bulk water/ice, and water confined in P-80/90/94 AC from temperature range 300-140 K at different heating/cooling rate. The dry activated carbon is baked at 150 ℃ under vacuum overnight to remove the moisture as much as possible. It is sealed in the aluminum pan immediately after baking. The confined water sample is prepared in the vapor chamber until it is fully filled with water.

The NMR experiments run for two sets of samples mainly: (1) pure water confined in P-80/90/94; (2) D_2O-H_2O mixed in molar ratio 4:1 confined in P-90. The D_2O existence reduces the intermolecular interaction between two H_2O molecules so that the relaxation mechanism and line width of ^{1}H in NMR spectra are contributed from intramolecular dipolar interaction in H_2O molecules mostly. For the pure water in P-80/90/94 samples, they are prepared to load the dry AC samples in a vapor chamber until the fully filled by water molecules. The mixed water in P-90 sample, it is applied by dripping the mixed water droplets into the dry P-90 sample sitting in

the 4mm rotor. The previous study (see **Figure 2.12**) shows there is no difference between two preparation process, the water confined in nanopores is not forming chemical bonds to the surface and cavity [109].

3.3 RESULTS AND DISCUSSION

3.3.1 Specific Heat of Water under Nanoconfinement

Using DSC method on water confined in P-90, we are able to obtain the heat capacity for temperatures ranging from 300 to 140 K. **Figure 3.2** shows the specific heat C_P of water confined by activated carbon at ambient pressure. Upon cooling from high temperature, the specific heat exhibits three regions: a sharp peak around 268 K, a broad peak centered at 230 K, and a shoulder region around 150 K. Comparing to the heat capacity of bulk water, the sharp endothermic peak at 268 K corresponds to the melting peak of excess water in the meso pores or intergranular special space [109]. Between 200 K and 250 K, a broad endothermic peak from 245 K to 210 K centered at 230 K is observed. This peak drop quickly below 200 K and at further lower temperature C_P exhibits a shoulder around T~150 K which we will discuss further in the **CHAPTER 4** and **CHAPTER 5**.

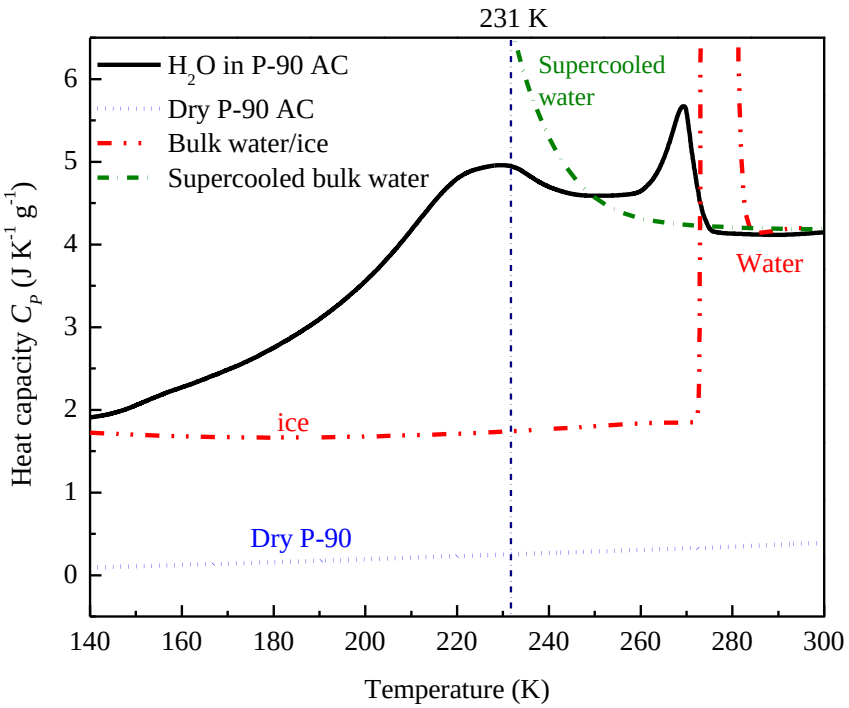

Figure 3.2 Specific heat C_P for water confined in activated carbon P-90, dry activated carbon P-90, and bulk water/ice from temperature 140 K to 300 K under heating rate 10 K/min. Solid black line represents the C_P for confined water, blue dot line represents C_P for dry P-90 carbon, red dash dot line represents C_P of bulk water/ice. All the measurements are under ambient pressure with heating/cooling rate 10 K/min. Green dash dot line is the guideline for experimental supercooled bulk water. [5]

In the following sections, based on dynamic measurements we will show that the broad peak centered at 230 K is related to the high-density liquid (HDL) to low-density liquid (LDL) conversion. The quick drop of C_P below 230 K corresponds to the gradually freezing of rotational degree of freedom for water confined in the nanopores.

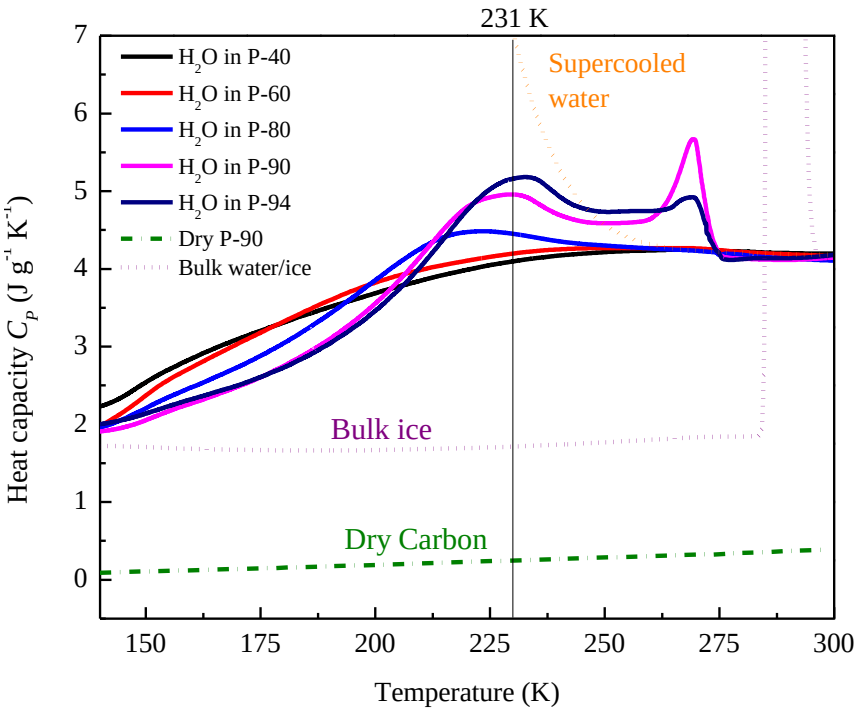

Figure 3.3 Specific heat for water confined in different pore sizes P-40/60/80/90/94, specific heat for bulk water/ice, and specific heat for dry activated carbon. Solid lines are specific heat for water confined in different activated samples. Purple dot line is experimental bulk ice/water specific heat, green dash dot line is experimental dry activated carbon specific heat. These experiments are running on heating rate 10 K/min. Orange dot line is specific heat of supercooled water in supercool experiment [5]

It is important to emphasis, at room temperature, the C_P of confined water and bulk water are almost the same around 4.12 $\mathrm{kJ \cdot K^{-1} \cdot g^{-1}}$ and at 140 K, the C_P of confined water are obviously larger than the ice. We also measured the heat capacity of water confined in different pores from 0.9 nm (H_2O in P-40) to 1.8 nm (H_2O in P-94) as shown in **Figure 3.3**. For water confined in pore size less than 1 nm (H_2O in P-40), the specific heat increases as a smooth convex curve by increasing temperature. For water confined in pore size 1.3 nm (H_2O in P-80) or larger (H_2O in P-90/94), the specific heat capacity increases as a concave curve and has a broad endothermic peak from 200 K-240 K. For water confined in larger pores such as 1.6 nm (P-90) and 1.8 nm (P-94), the broad endothermic peak is more obvious and the peak center shifted to

higher temperature by increasing the pore sizes. There also has excess water accumulated in mesopores for water confined in P-90 and P-94 sample corresponding to the sharp melting peak at 268 K. This series of experiments shows, water confined under 1 nm cannot represent bulk water, only for water confined in larger than 1.3 nm it can be similar to bulk water. It is worth to mention, for water confined in larger than 2 nm, it will crystallize to ice below bulk water freezing temperature and is not suitable for the designed experiments at sufficient low temperature.

3.3.2 State of Confined Water above 200 K

Based on DSC experiment, to explain the endothermic peak centered at 230 K is the key to understand the thermal dynamic property of water. One point of view is it is related to the maximum C_P on Widom line which is the extension of LLPC [26, 67-69, 72, 73, 84, 90, 118-120]. The second explanation is it is micro-melting/crystallization of confined water [45, 75-77, 121]. The third interpretation is this endothermic peak corresponds to glass transition of confined water [122, 123]. We applied six different heating/cooling rate variants from 2.5 K/min to 20 K/min on the sample in DSC. Then we observed the broad endothermic peak doesn't shift by varying the heating or cooling rate, which indicates it is not related to glass transition.

However, it is still hard to tell the structure fluctuation or micro-melting/crystallization from DSC measurements. At this moment, NMR is a unique technique to probe the state of water. Due to the strong dipolar interaction of hexagonal ice, the signal of ice has extremely fast decay in FID and the FFT spectrum would have 2.1 MHz in width, respectively, which is too broad to be seen in NMR spectrum. Hence, if the water freezes to ice, it will have an intensity loss on NMR signal, if not, the confined water still stays in liquid state.

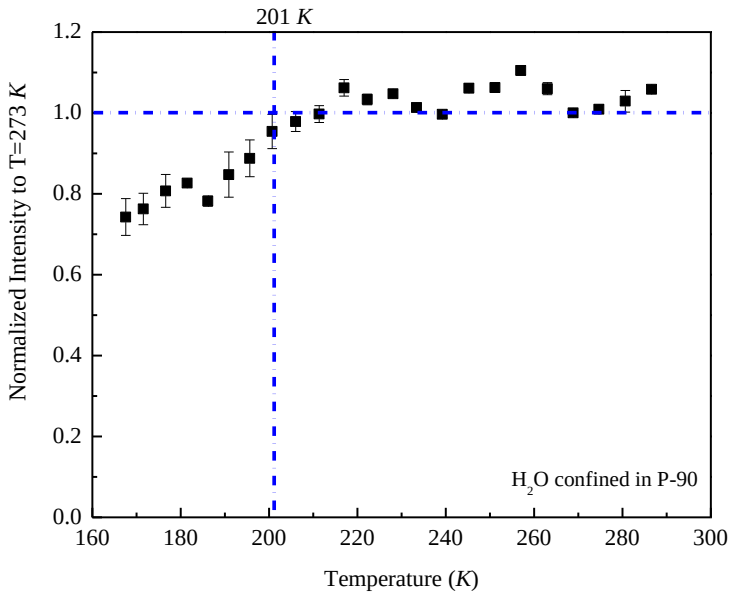

Figure 3.4 Plot of normalized intensity from ^{1}H NMR on water in P-90 AC versus temperatures

We run the single pulse experiments for water confined in P-90 at different temperatures. The FID signal is extrapolated to $t = 0$ and corrected by Curries law ($1/T$). As shown in **Figure 3.3**, above 200 K, there is no intensity loss, indicated by the more or less constant intensity above 200 K as it is in the room temperature. That is a strong evidence that above 200 K, there is no crystallization happened for confined water.

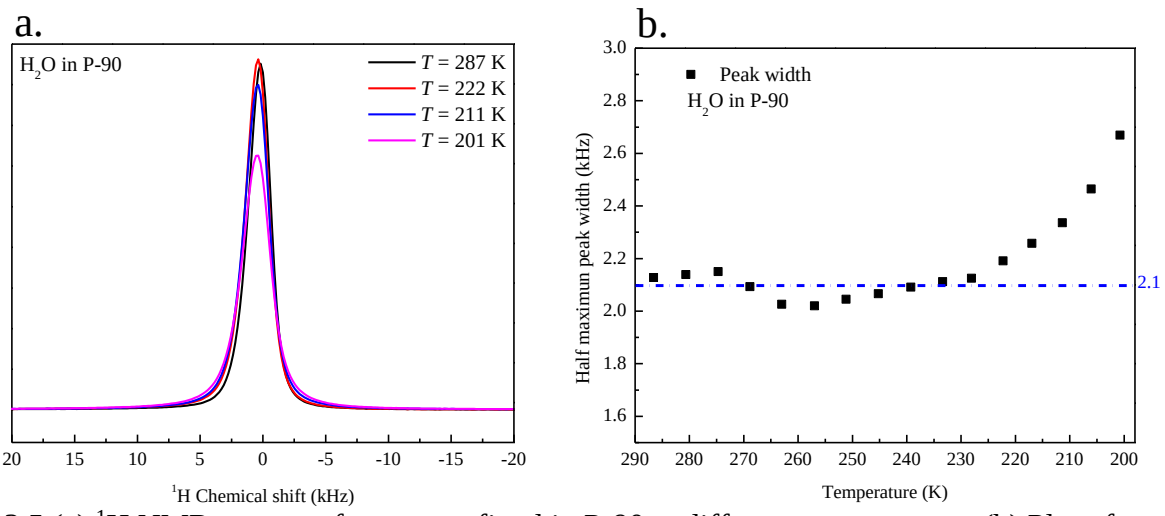

Figure 3.5 (a) ^{1}H NMR spectra of water confined in P-90 at different temperatures. (b) Plot of full width at half maximum (FWHM) from ^{1}H NMR spectra of water in P-90 versus temperatures.

Furthermore, the spectrum has a narrow Lorentzian peak with peak width 2.1 kHz (4.2 ppm) (see **Figure 3.5 a.** and **b.**) corresponding to the motional narrowing of water molecules, in contrast to 32 kHz the static limit of water molecule. Therefore, the confined water is highly mobile as bulk water and no crystallization occurs above 200K. Such high mobility of water molecules is also consistent with our MD simulation studies, for instance, the translational and rotational diffusion coefficient of water confined in 1.6nm pores are $D_t \approx 10^{-6}\, nm^2/ps$ and $D_r \approx 10^{-4} nm^2/ps$, respectively.

It is worth noticing that there is a gentle non-linear increase of the peak with (see **Figure 3.5 (b)**) when cooling the sample from 220-200 K. The peak width of the spectrum at room temperature is mainly contributed from pore size distribution. The broaden of the peak width is mainly due to the dipolar interaction which is related to the molecular motion. The slowing down molecular motion such as the rotational motion (related to intra-molecular dipolar interaction) or the translational motion (related to inter-molecular dipolar interaction) would cause the peak width broaden [92].

Then, it is important to study the dynamic properties of confined water in the liquid state. We applied NMR relaxation measurements in the following session: spin-lattice T_1 relaxation measurements and spin-spin T_2 relaxation measurements to further discuss the dynamic changes of the confined water.

3.3.3 Spin-Lattice Relaxation Measurements for Water in P-90 AC

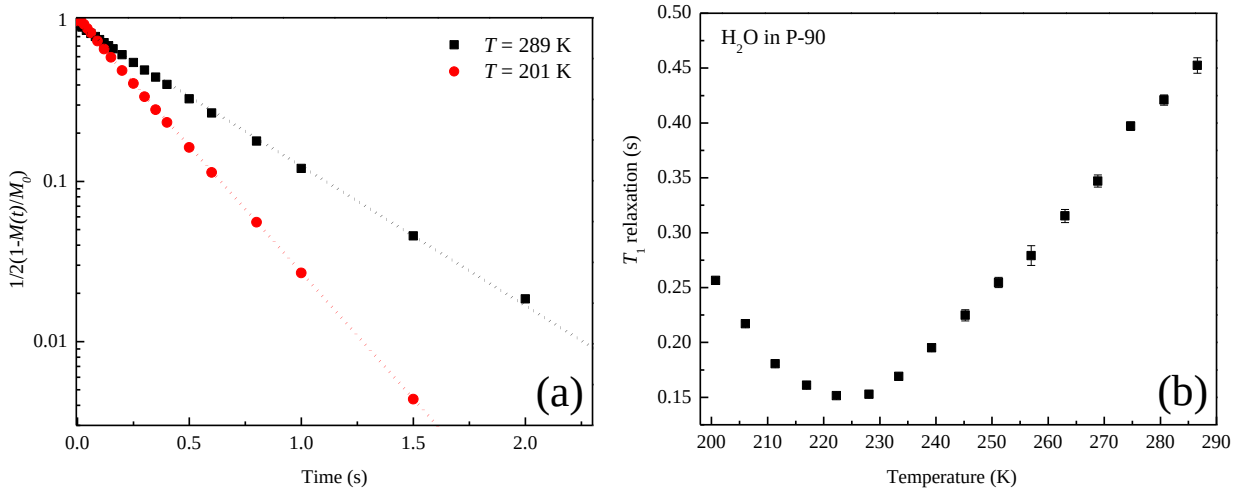

Figure 3.6. (a) Logarithm magnetization versus time at selected temperatures. (b) Temperature dependence of the ^{1}H NMR spin-lattice relaxation time T_1 for water confined in P-90 sample.

We applied inversion-recovery pulse sequence to measure the spin-lattice relaxation time of confined water in P-90. For the whole temperature range, T_1 is obtained from fitting the **Eq. (2.10)** $M(t) = M_0(1 - 2\exp(-t/T_1))$ with NMR signal by varying a serious of *t*. As shown in Figure 3.6 (a), by plotting logarithm of magnetization versus time, there is a straight line fitted for T_1, which means there is single component for T_1. T_1 has a minimum at T = 228 K (see **Figure 3.5** (a)). Assume the T_1 relaxation is dominant from the tumbling motion of the water molecule, then the rotational correlation time could be calculated from Bloembergen-Purcell-Pound Equation **Eq. (2.8)**: $\left(\frac{1}{T_1}\right) = \frac{3\gamma^4\hbar^2}{10b^6}\left(\frac{\tau}{1+\omega_0^2\tau^2} + \frac{4\tau}{1+4\omega_0^2\tau^2}\right)$

Here γ is the gyromagnetic ratio of proton, h is plank constant, b is the distance between the two hydrogen atoms in a water molecule (0.156 nm) and $\omega_0/2\pi$ is the Larmor frequency (500 MHz at 11.7 T). Correlation time τ is estimated by the average time taken for the molecule to rotate by 1 rad. Smaller τ corresponds to faster molecular motion, while larger τ corresponds to slower molecular motion.

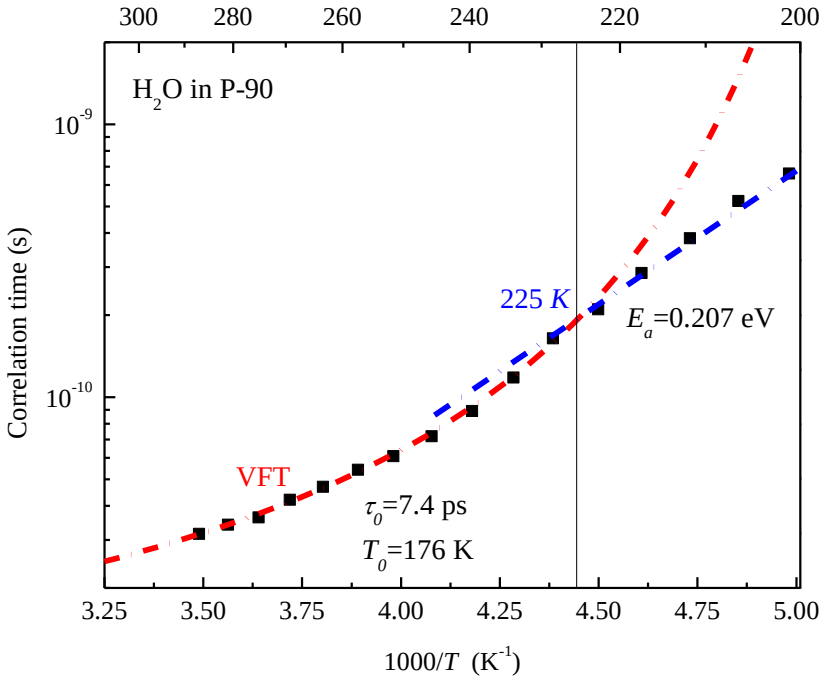

Figure 3.7 Correlation time of water confined in P-90 AC versus temperatures. The red dash dot line is the VFT fitting for the high temperature regime data with $T_0 = 176$ K and $\tau_0 = 7.4$ ps. The activation energy calculated from Arrhenius equation $E_a = 0.207$ eV

The correlation time versus temperature is plotted in **Figure 3.7**. There is a non-linear increase of the rotational correlation time when decreasing the temperature. At high temperature, the correlation time follows Vogel-Fulcher-Tubman (VFT) equation $\tau = \tau_0 exp(-A/(T - T_0))$ where A is a fitting parameter, T_0 is the ideal glass transition temperature, and τ_0 is the initial relaxation time. Since at high temperature, the confined water is similar to the bulk water, here we fixed $T_0 = 176\ K$ which is obtained from the best VFT fitting parameter for bulk water (see **Appendix B1**).

In **Figure 3.7**, we can see below 228 K, there is an obvious deviation for correlation time from the VFT behavior (red dot dashed line) and following Arrhenius behavior (blue dot dashed line). The activation energy calculated from Arrhenius equation, E_a, is 0.207 eV, which is exactly the energy to break hydrogen bonds. The transition temperature is at 225 K from the intersection of two behavior fitting lines. Such mild transition is called dynamic crossover transition or fragile to strong transition (FST) where VFT liquid represents fragile liquid while Arrhenius liquid represents strong liquid.

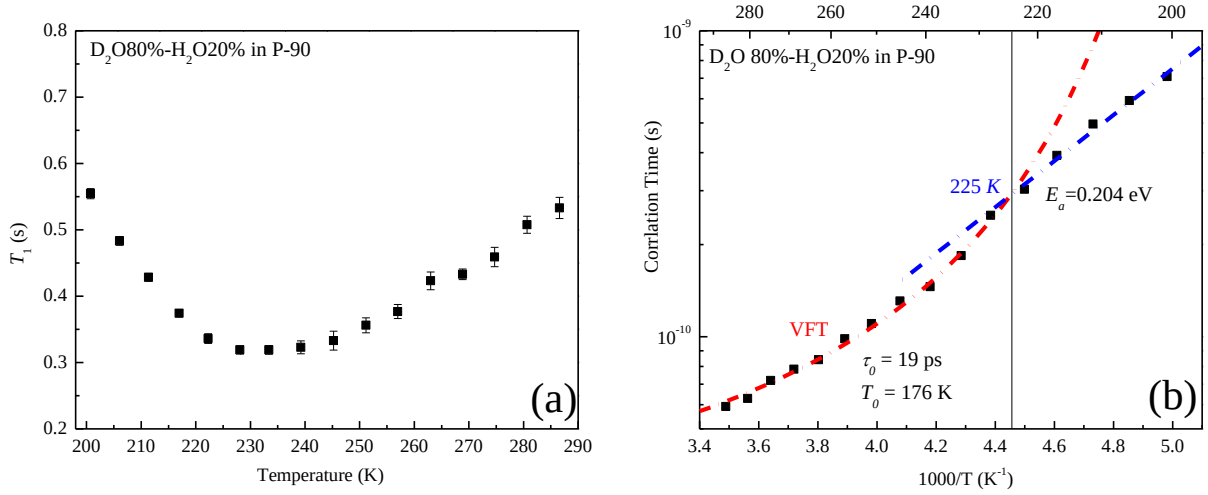

Figure 3.8 (a) Temperature dependence of the ^{1}H NMR spin-lattice relaxation time T_1 of mixed water confined in P-90 sample. (b) Correlation time of mixed water in P-90 AC versus temperatures. The red dash dot line is the VFT fitting for the high temperature regime data with $T_0 = 176$ K and $\tau_0 = 19\ ps$.

To enhance the effect of rotational motion on T_1 relaxation and reduce the translational motion effect, the measurement of T_1 is also performed on a mixed sample of 80%D_2O-20%H_2O confined in P-90. The reason is that the number of H_2O molecules surrounded each H_2O will decrease by adding D_2O, which greatly weakens the intermolecular dipole-dipole interaction between H-H. Due to the fast exchange between D-O and H-O, the intramolecular dipolar interaction between H-H also reduced by adding D_2O. So T_1 of the mixed sample is longer than that in pure H_2O sample. Since, the exchange rate between D-O and H-O is faster than the rate of

tumbling motion of water molecule. So, the T_1 of mixed sample mainly reflects the rotational motion of intra-molecule proton. The activated energy obtained from Arrhenius equation is $0.204\ eV$ which is the hydrogen bond break energy.

In **Figure 3.8** (a), the T_1 value of mixed water sample. T_1 still has a minimum at around 230 K. To obtain the "real" rotational correlation time we applied BPP equation to the T_1 value to estimate the correlation time. The VFT and Arrhenius fitting shows the dynamic crossover temperature is still at 225 K. This confirms the FTS transition is related to slowing down the rotational motion.

Recall the dynamic crossover or FST observed for water confined under hydrophilic surfaces system at 225 K also, (see **Figure 1.12**), then, the surface effect for this dynamic crossover can be excluded. Furthermore, it is observed in the liquid state of water, so such FST is not induced by crystallization. In the following session, we will discuss the pore-size independent measurement results and confirm this observed dynamic crossover is driven by the supercooled bulk water.

3.3.4 Size Independent T_1 Relaxation Measurements

In **section 3.3.3**, we selected P-90 AC as our standard confinement model to investigate the properties of confined water.

To discuss the size effect of the observed dynamic crossover, we performed other two samples: pure water confined in P-80 which has pore size 1.3 nm and pure water in P-94 with pore size 1.8 nm (some pores are collapsed during activation process).

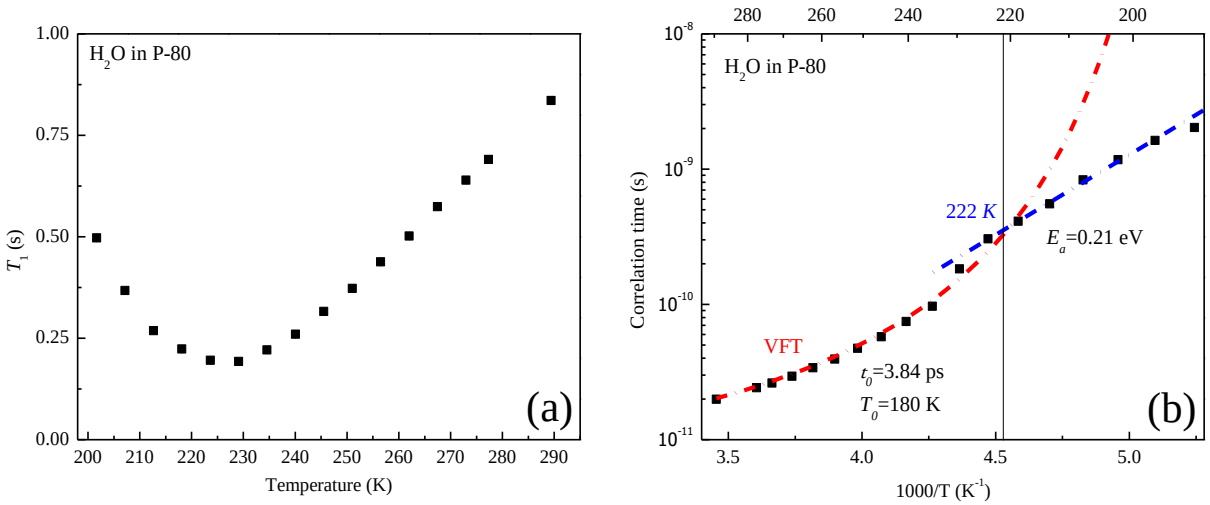

Figure 3.9 (a) Temperature dependence of the ^{1}H NMR spin-lattice relaxation time T_1 of water confined in P-80. (b) Correlation time of water in P-80 versus temperatures. The red dash dot line is the VFT fitting for the high temperature regime data with $T_0 = 180$ K and $\tau_0 = 3.84$ ps. The activation energy got from Arrhenius equation fitting is 0.21 eV.

Figure 3.9 (a) shows for pure water confined in P-80 sample, T_1 has a minimum at 230 K. By applying **Eq. (2.8)** to calculate the correlation time τ as plotted in **Figure 3.9** (b), at 222 K the rotational correlation time is not following VFT liquid behavior. When going to lower temperature 220 K, the rotational correlation time followers Arrhenius equation well. The activation energy obtained from Arrhenius fitting is 0.21 eV close to the hydrogen bonds breaking energy.

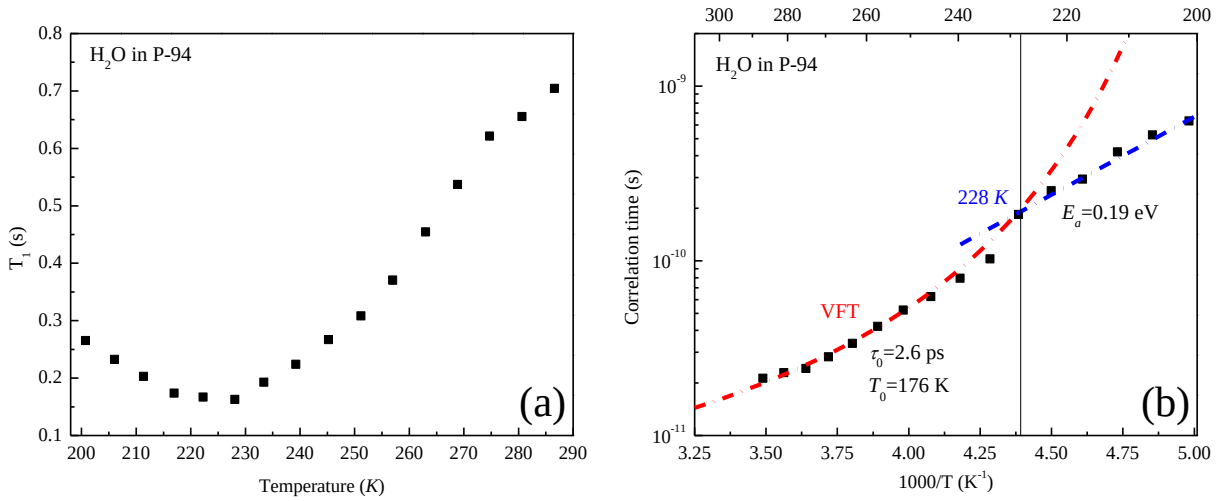

Figure 3.10 (a) Temperature dependence of the ^{1}H NMR spin-lattice relaxation time T_1 of water confined in P-94 sample. (b) Correlation time of water in P-94 versus temperatures. The red dash dot line is the VFT fitting for the high temperature regime data with $T_0 = 176$ K and $\tau_0 = 2.6$ ps. The activation energy $E_a = 0.19$ eV

Figure 3.10 (a) shows for pure water confined in P-94 sample, T_1 also has a minimum at 228 K. The dynamic crossover temperature is at 228 K to distinguish VFT liquid and Arrhenius liquid. The activation energy calculated from Arrhenius fitting parameter is 0.19 eV, which is close to the hydrogen bond broken energy.

For the state of confined water in these two activated carbons, we also applied single pulse measurements for both samples. For water confined in P-80, the NMR intensity doesn't lose until 190 K (see **Figure 3.11** (a)), for water confined in P-94, the intensity keeps constant until 210 K (see **Figure 3.11** (b)). So, both temperatures are lower than 228 K, which ensure the dynamic crossover happens in the liquid state instead of inducing by micro-crystallization.

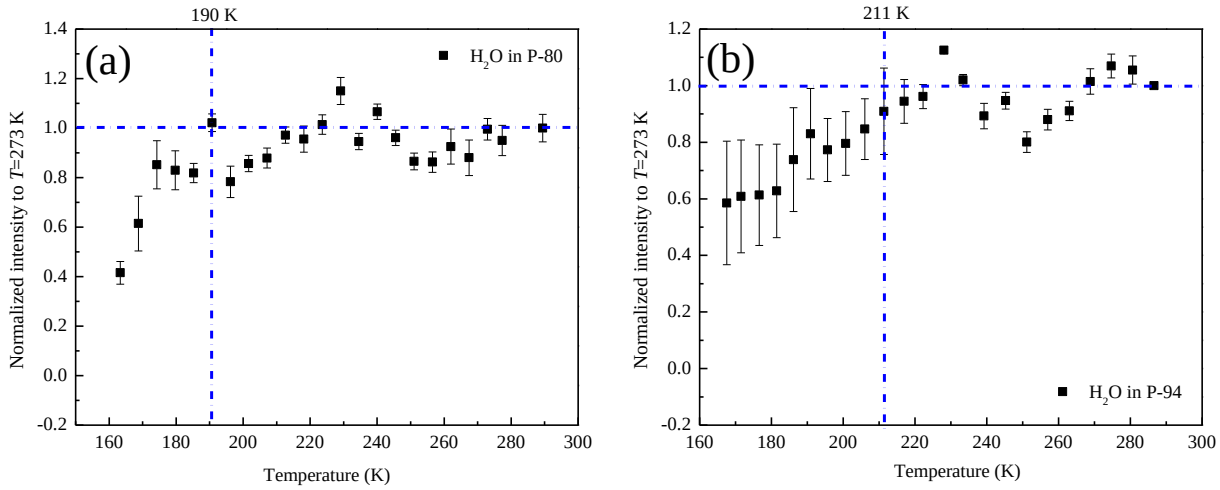

Figure 3.11 (a) Normalized intensity of water in P-80 versus temperatures. (b) Normalized intensity of water in P-94 versus temperatures

Based on the analysis of T_1 for water confined in different pore sizes, we concluded the dynamic crossover temperature around 225-228 K is independent with the pore size, and surface effect, which indicates it is related to the intrinsic property of bulk water.

3.3.5 T_2 Spin-Spin Relaxation Measurements for Water in P-90

On the other hand, the spin-spin lattice time T_2 measured by CPMG pulse reflects more translational motion of the molecules.

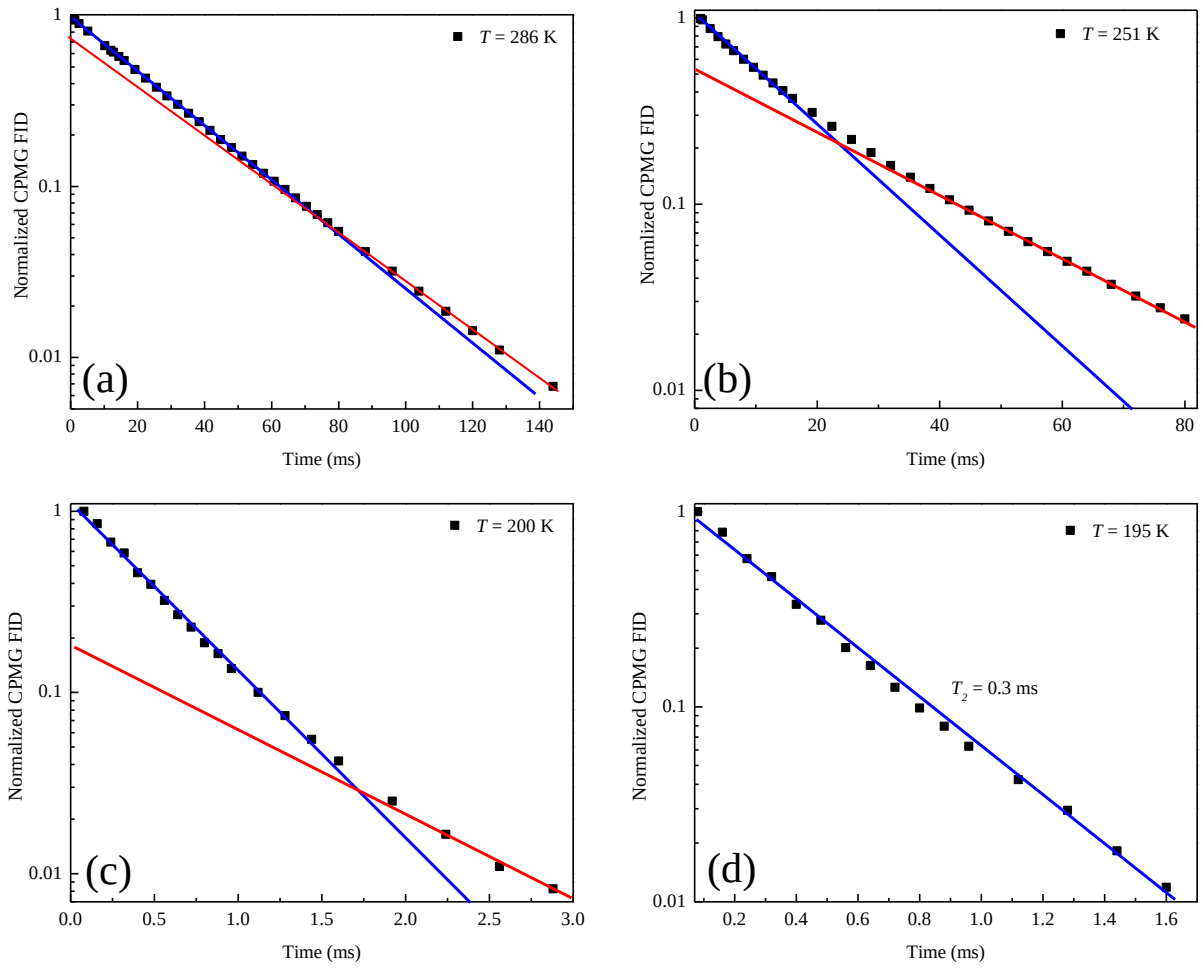

Figure 3.12 (a)-(d) ^{1}H NMR spin-spin relaxation time T_2 CPMG measurement for water in P-90 AC at selected temperatures. Y axis is normalized to M_0, black squares are the data obtained from different number of echoes. Red solid lines represent longer T_2 time and blue solid lines represent shorter T_2 time.

In contrast to T_1 above 200 K, T_2 is a bi-exponential decay function of temperature with two components: short-time scale and the long-time scale components, respectively. (see **Figure 3.12** (a-d)). At 195 K, there is single exponential decay for T_2 measurement. The two different

time scales coexistence at one temperature indicates protons having two different environments. Water has two different "states" coexistence in T_2 time scale.

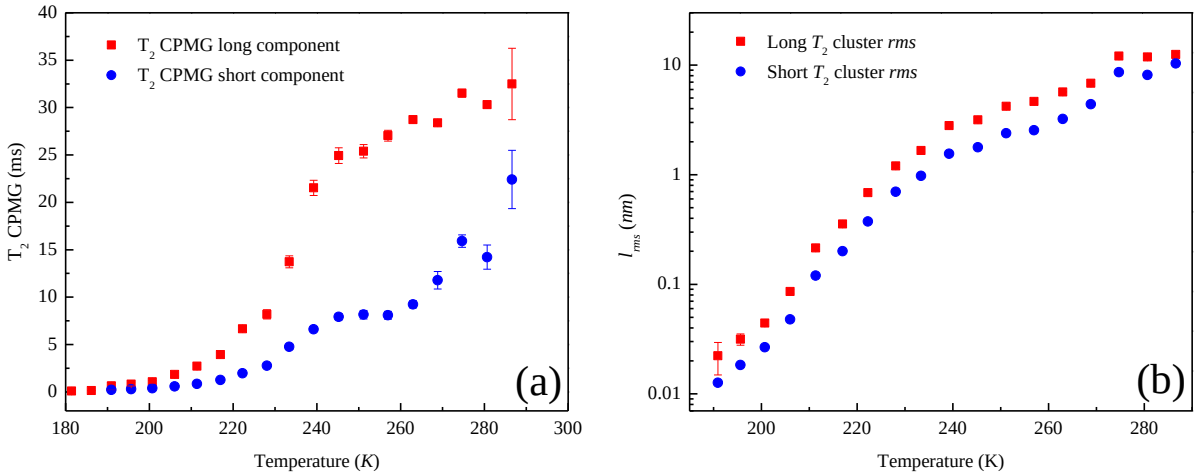

Figure 3.13 (a) T_2 long and short components versus temperatures. (b) Root mean square distance in long and short T_2 time scale.

To investigate the "two states" time scale and length scale, we plot the long and short T_2 versus temperature (see **Figure 3.13** (a)) and calculate the root mean square distance in T_2 time scale as shown in **Figure 3.13** (b).

The spin-spin relaxation time T_2 reflects not only the time scale of cluster existence but also indicates the correlation length or diffusion length for a cluster or molecules. We applied root mean square (rms) distance calculation equation $l = \sqrt{6Dt}$ for our slit-shaped pore system to estimate the water cluster size and diffusion length, where l is the diffusion length, D is molecule self-diffusion coefficient, t is the diffusion time. In the calculation, the water self-diffusion coefficients at different temperatures are obtained from the collaborate simulation results [ref], the diffusion time t is replaced by T_2 value. We estimated the diffusion length and plotted by temperatures as shown in **Figure 3.13**. The HDW and LDW at room temperature, the diffusion length is around 10 nm for both which indicates the HDW cluster size and LDW cluster sizes is in

10 nm length scale. This length scale is not in atomic scale and cannot be negligible. The two components T_2 value and 10 nm scale cluster size both are strong evidence that water is heterogeneity and has HDL and LDL clusters coexistence at room temperature. When temperature decrease, the diffusion of HDL and LDL clusters are slowing down and become more viscous. At low temperature, intermolecular dipolar interaction dominates the T_2 relaxation mechanism.

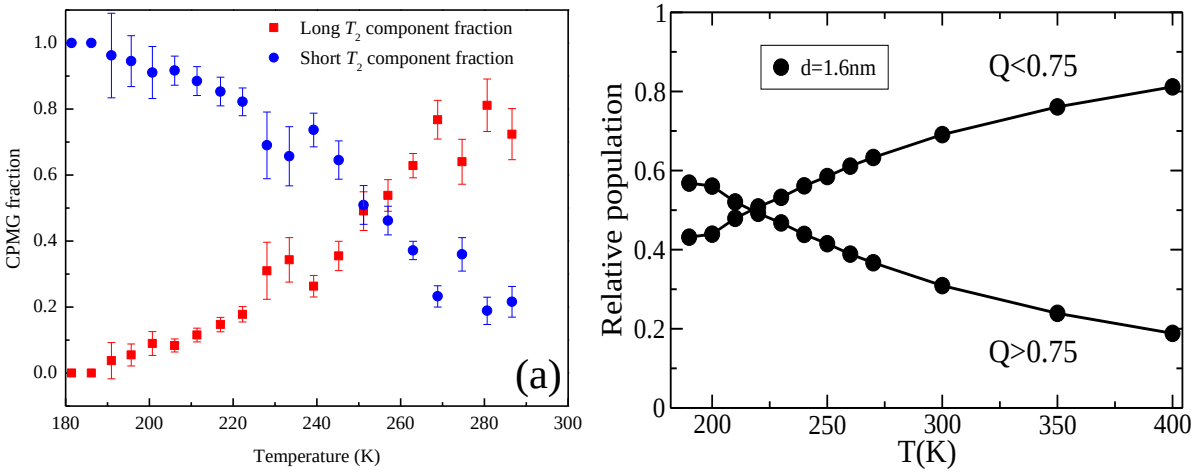

Figure 3.14 (a) The fraction of long and short T_2 component versus temperatures. (b) Relative population from MD simulation for HDL and LDL local structure versus temperatures

Figure 3.14 (a) shows the fraction for two components obtained from CPMG data fitting. (b) shows local structure of the simulation results from WAIL water. Q is local structure index. Q>0.75 corresponds to more tetrahedral-like structure and Q<0.75 represents more dense-packing structure. This is consistent with the two-state model at room temperature [38, 40] and coexistence of two structure components in the LLPT hypothesis [26]. Two-state model mentioned two "macro-state" HDL state and LDL state with their dominated local structure HDL and LDL structures. And LLPT indicates the two different microscopic structures HDL and LDL at room temperature. Also, in our collaborate simulation results, it clearly shows that HDL-like continuously transform to LDL-like structure as temperature decreases.

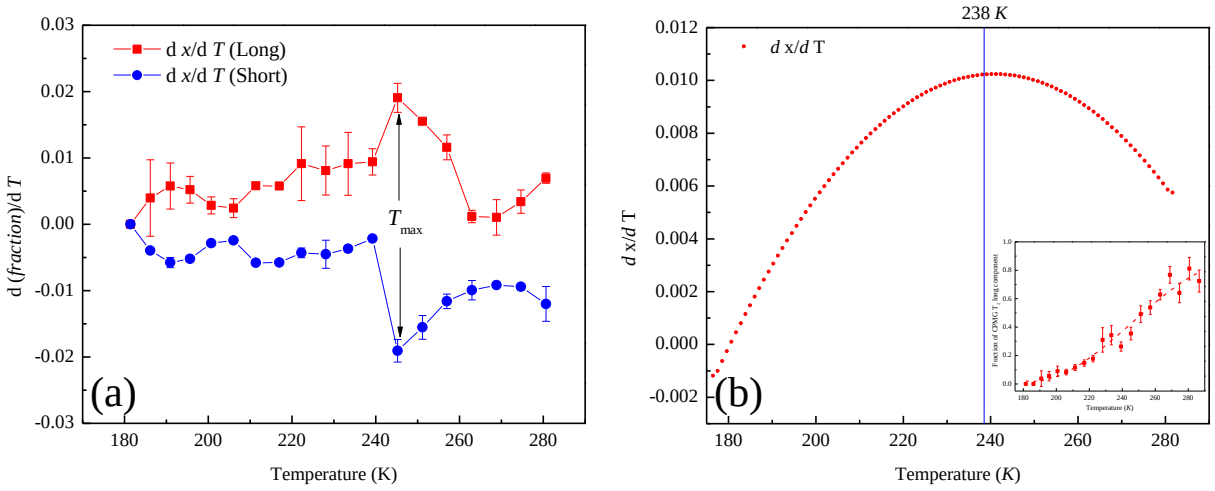

Figure 3.15 (a) Derivative of fraction of long and short components in T_2 measurements versus temperature. (b) Mathematical derivative of the fraction of CPMG long T_2 component versus temperatures. The inserted picture is the plot of fraction of CPMG long T_2 component versus temperature and empirical fitting for the fraction plot

Figure 3.15 describes how fast the fraction changed by temperature. In **Figure 3.15** (a), we found the fastest conversion between HDL and LDL clusters is around 245 K and in **Figure 3.15** (b) is at 238 K. Note: We fitted the fraction of CPMG long T_2 component by a polynomial equation empirically: $f(x) = A + Bx^1 + Cx^2 + Dx^3$, where A=11.7, B=-0.1587, C=6.86×10^{-4}, D=-9.31×10^{-7} from best fitting. The differential of fraction and temperature shows there is a peak around 238 K which is not far away from the endothermic peak on DSC around 230 K (see **Figure 3.2**)

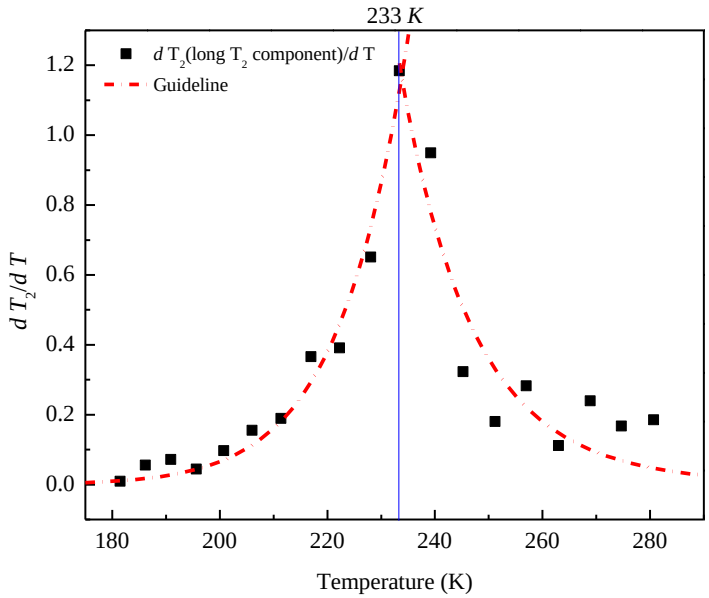

Figure 3.16 Derivative of CPMG long T_2 value of temperature versus temperatures. The red dash dot line is the guideline for reading the data.

Figure 3.16 shows how fast the T_2 value changed by temperatures. It is clear to see at 233 K, the change of T_2 is the most drastic which is consistent with the fast drop of T_2

3.3.6 Size Independent T_2 CPMG Measurements

In the same way, to see the phase separation phenomenon in different pore-size samples is the method we determine the phenomenon is induced by confinement effect or from supercooled water. We also applied CPMG T_2 measurements on sample P-80 and P-94.

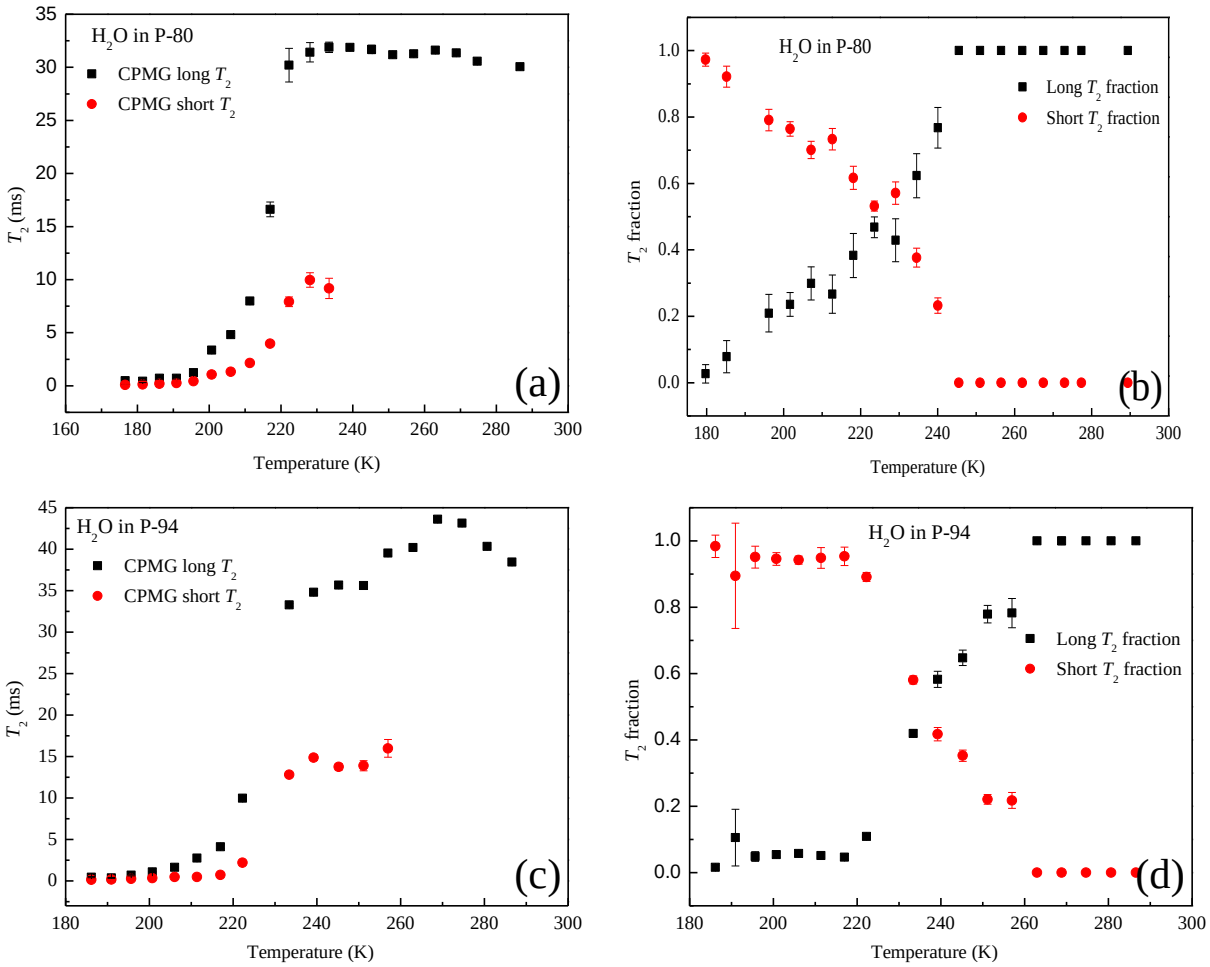

Figure 3.17 (a) Temperature dependence of ^{1}H NMR spin-spin relaxation time T_2 of water in P-80 (b) The fraction of longer T_2 and shorter T_2 components of water in P-80 versus temperatures. (c) Temperature dependence of ^{1}H NMR spin-spin relaxation time T_2 of water in P-94 (d) The fraction of longer T_2 and shorter T_2 components of water in P-94 versus temperatures. Black solid squares represent longer T_2 and red solid dots represent shorter T_2

From biexponential decay analysis, it is clear to see in sample P-80 and P-94, there still exists phase separation and HDL gradually converted to LDL by lowering the temperature.

So, the two liquids conversion is not only happened under nanoconfinement, also could happen in the deep supercooled bulk water.

3.4 CONCLUSION

In this chapter, we investigate the state of water confined in hydrophobic nanopores by employing DSC, NMR and MD simulations (collaborate work). For the studied matrices, we find that water under nanoconfinement is in the liquid state above 200 K. Water is heterogeneity at room temperature which could be identified as HDW cluster and LDW cluster. HDL and LDL could convert to each other by varying temperature. Water confined in hydrophobic matrices exhibits a dynamic crossover from VFT to Arrhenius behavior at 230K. It is important to emphasis that this dynamic crossover, previously reported in hydrophilic and other confined systems, is a general feature of liquid water, which is not induced by crystallization or glass transition. The endothermic peak centered at 230K corresponds to the quick conversion from high-density liquid clusters to low-density liquid clusters. The coexistence of HDL and LDL cluster and the gradual conversion between two clusters indicates why water, especially supercooled water has these anomalous properties. Furthermore, the quick drop of C_P below 230 K to 200K was due to freezing the degree of freedom, especially translational motion. At 200 K, most of the confined water are converted to LDL, at this moment, it proves the existence of low density liquid is a thermal equilibrium liquid rather than coarse-grained ice.

CHAPTER 4 ROTATIONAL GLASS TRANSITION FOR SUPERCOOLED WATER

4.1 INTRODUCTION

Liquids could be cooled below its conventional freezing temperature but still remaining liquid states. Such kind of liquids are called supercooled liquids [7]. Thermodynamically, supercooled liquid is a metastable liquid [124]. As a supercooled liquid cooled to lower temperature without nucleation, the collisions and movements of molecules become more and more sluggish, and the time-scale for the molecules rearrangement to reach thermal equilibrium state is getting longer [125]. At certain low temperature, the structural relaxation time becomes extremely long and the liquids becomes ultra-viscous like solid [126]. One well-known example is window glass which is formed from quenching supercooled SiO_2 liquid. The transition from a highly viscous supercooled liquid to a non-equilibrium solid is known as glass transition, and the onset transition temperature T_g is called glass transition temperature [124].

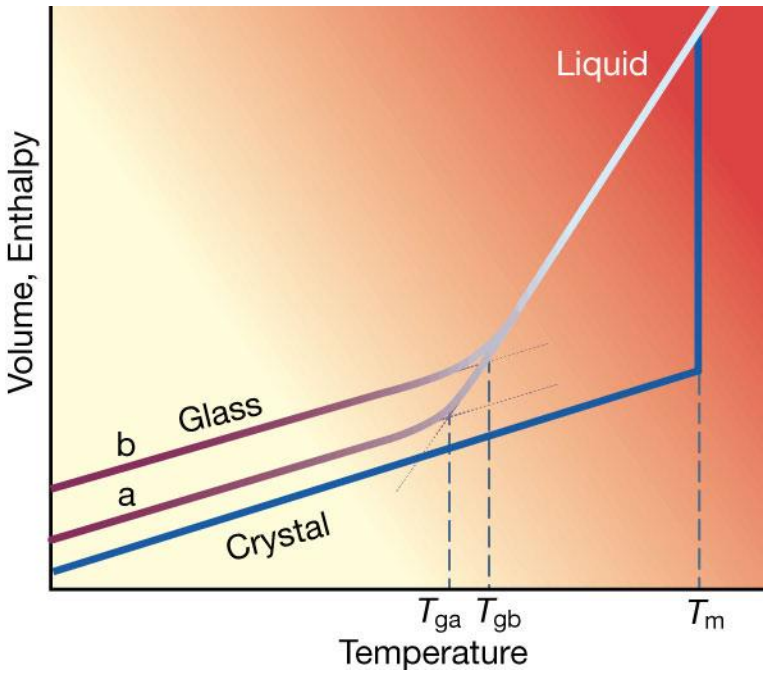

Figure 4.1 Illustration of volume/enthalpy change for liquid, crystal and glass [124]

To determine the glass transition and glass transition temperature has several ways. One conventional way is to observe the volume or enthalpy changed by temperature as shown in **Figure 4.1**. For the liquid-crystal first order phase transition, the enthalpy changed from liquid state to crystal state is discontinuous. While for the liquid-glass glass transition, the change of enthalpy is continuous and variant by the cooling rate. As we know, the specific heat is the thermal response function of enthalpy changed by temperature. So, for the first-order phase transition such as freezing, the C_P will have a sharp narrow peak at freezing temperature, while for the glass transition, the C_P will show a broad peak over a few degrees. Not only the thermodynamics changes when approaching to the glass transition temperature T_g, the nature of dynamics around T_g is also quite different from the liquid behavior. For example, when cooling the glass-forming liquid near T_g, the structural relaxation time increases significantly and is dominated by non-exponential relaxation process [127]. In addition to the dramatic change of

relaxation, some other interesting behavior for the supercooled liquids includes the Stokes-Einstein relation breakdown and decoupling between rotational and translational motion [13].

For bulk water, if the cooling rate is sufficiently fast enough, for example, dripping a drop of micrometer sized water onto the cool plate, it could form glassy state below 136 K at ambient pressure [11, 128]. For last two decades, the existence of water glass transition temperature at 136 K is widely accepted. However, the transition qualities are difficult to reconcile in the current knowledge of glass transition. Angel al. et research group argued that the real glass transition temperature of water should be around 150 K from their analysis of DSC experiments on hyperquenched inorganic glasses results [102-104]. Miller and Swenson's research group considered the T_g of water is located at 160-165 K from the calculation of Tammann-Hesse viscosity equation and broadband dielectric spectroscopy (DBS) experiments for bulk water [74, 123].

In this chapter, we keep cooling the water confined in P-90 below 200 K, at which all the liquid water is low-density water. We found partial water form amorphous ice and the rotational motion of the liquid water slowing down. Thermodynamically, the specific heat C_P dropped quickly due to loss of the degree of freedom.

All these experimental evidences indicate the water could have a glass transition just below 200 K.

4.2 EXPERIMENTAL RESULTS AND DISCUSSION

We applied single pulse NMR experiments on water confined in P-90 to get the ^{1}H spectra at different temperatures and performed T_1 relaxation measurements from 200-170 K to discuss the change of rotational motion. To discuss the different features on ^{1}H NMR spectra at low temperatures, we performed spin echo pulse on the tested sample. If the spin echo

(Hahnecho pulse) spectrum could overlap with the single pulse spectrum, all the spins included in the spectrum are coupled and belong to the same state of confined water. Otherwise, mismatched part is decoupled with previous spins and belongs to other types of state of water. We also did single pulse experiments and T_1 relaxation measurements on water confined in P-80 and P-94.

4.2.1 ^{1}H NMR Spectrum Analysis

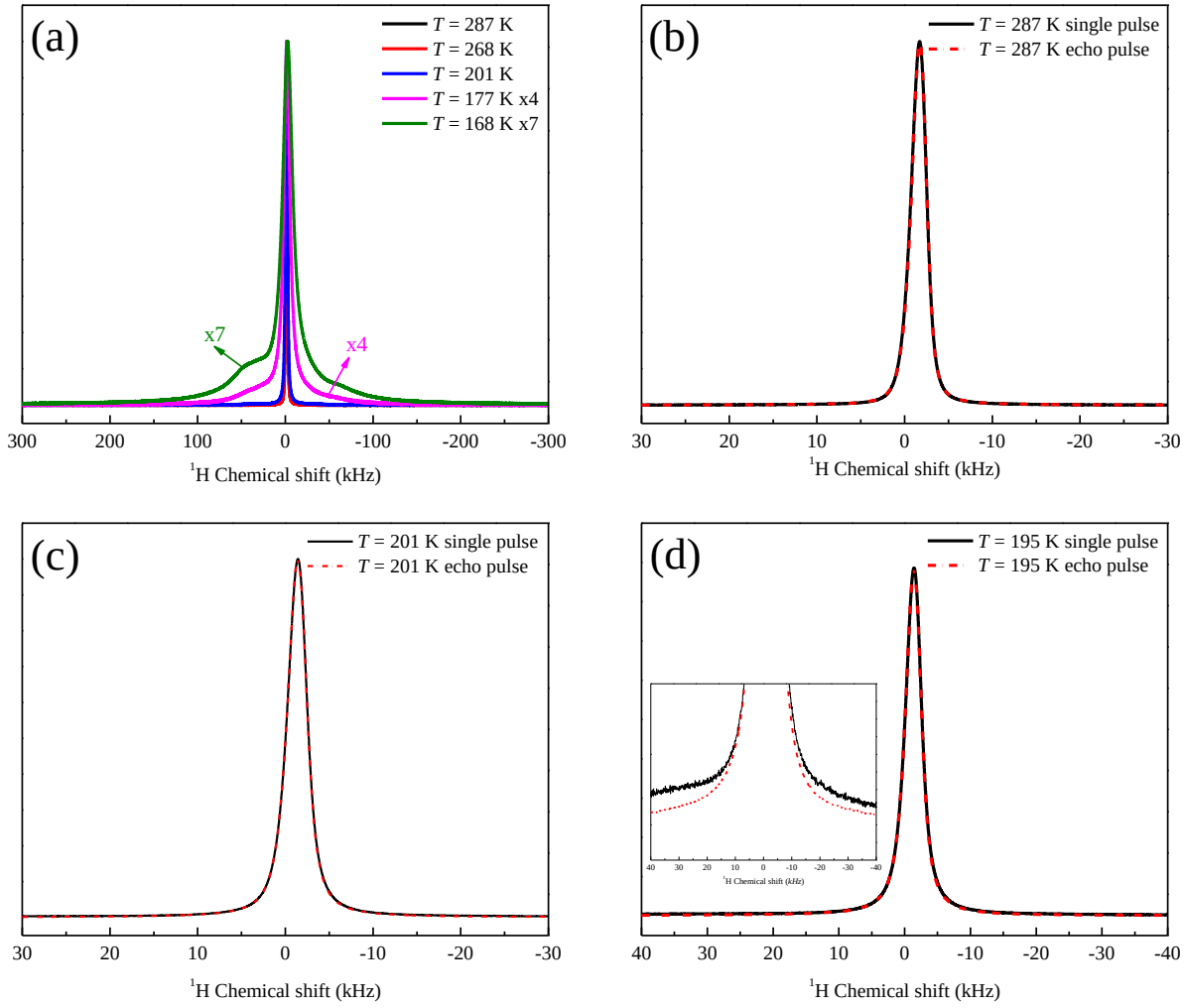

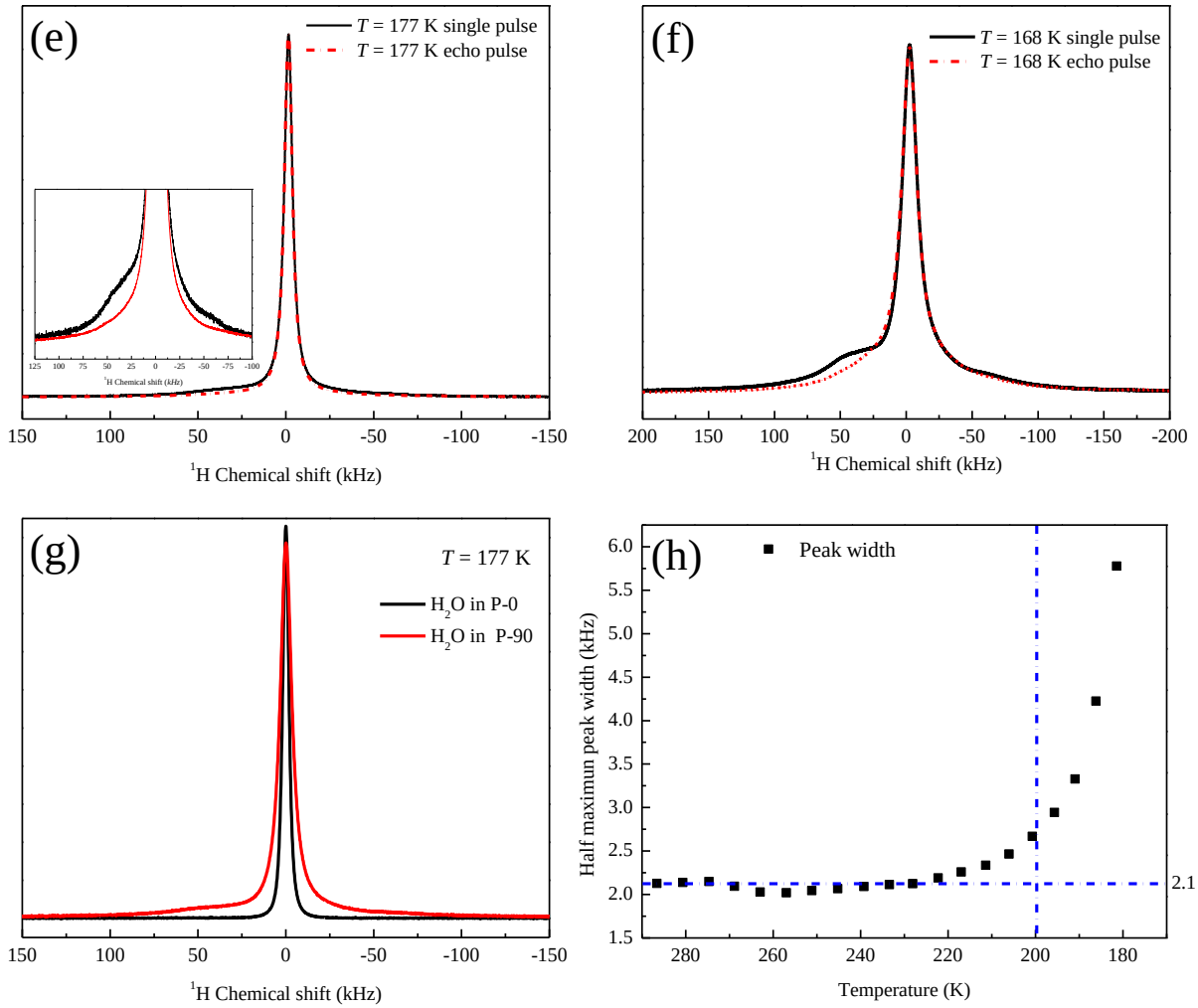

Figure 4.2 (a) Spectra of ^{1}H NMR of water confined in P-90 at different temperatures. (b)-(f) ^{1}H NMR spectra comparison with single pulse measurement and spin-echo pulse measurements of water in P-90 at different temperatures separately. (g) Comparison of spectra at $T = 177\ K$ for water in P-90 and water in P-0 (h) Full Width at Half Maximum (FWHM) of single pulse ^{1}H NMR spectra of water in P-90 versus temperatures

Confined water can be cooled below 200 K, as shown in **Figure 4.2** (a) and (h), the spectrum is significantly getting broad when the sample is at lower temperature. More importantly, at T = 177 K, the whole spectrum is not only broader but also has a broad feature from bottom. When temperature is getting lower, the asymmetric feature from bottom of the peak becomes more and more obvious. Meanwhile, the total intensity of the spectrum also dropped below 200 K as mentioned in **CHAPTER 3**. (See **Figure 3.2**). The loss of intensity

contributed from two concerns: one is water partial crystallization in larger pores, the other is from the inaccurate intensity correction of the bottom peak.

To investigate the spins in center sharp peak and in the bottom peak at low temperature coupled or decoupled, we applied spin-echo experiment on the same sample. Examples of comparison of ^{1}H NMR single pulse spectrum and spin-echo spectrum are listed in **Figure 4.2 (b)-(f)**. Above 200 K, the spin-echo spectrum overlapped with single pulse spectrum well which means all the spins in the spectrum are in the liquid state. At 195 K, the spin-echo spectrum has an observable mismatch with the single pulse spectrum at the bottom of the spectrum (see inserted picture). At 177 K, the growth of the broad feature became more significant. At 168 K, such broad bottom feature is clear enough to observe without any zoom in. So, the spins in the center sharp peak are not coupled with the spins in the broad peak from bottom. It is worth to mention, the FWHM of this broad feature in the spectrum is 100 kHz, which is larger than the water static limit 32 kHz. This observation is a strong evidence that part of the confined water starts to form amorphous ice at 195 K.

To clarify which part of water stays in liquid state and which part of water forms amorphous ice, we compare ^{1}H NMR spectrum of water confined in P-0 at 177 K with that of water confined in P-90. For P-0 AC sample whose average pore size is 0.46 nm from surface to surface, there is only single layer of water staying in the pores. In **CHAPTER 6**, it shows such confined monolayer water won't freeze even at extremely low temperature. As we discussed in **CHAPTER 2**, NICS effect is an efficient way to tell the position of detected spins in the pores by examining the chemical shift. In **Figure 4.2** (g), the center sharp peak of water in P-90 is on the same chemical shift with the peak of water in P-0. Since for water confined in P-0, it is known that water is interfacial water, so for the center sharp peak in water confined in P-90

sample, it represents the water towards to the surface without crystallization. While the broad peak from bottom in water in P-90 sample represents the amorphous ice growing from the center of pores. One more detail should be mentioned, is the FWHM of center sharp peak of water in P-90 is larger than that of water in P-0. Which means the motion of non-freezing LDL is still much slower than the pure interfacial water.

Figure 4.2 (h) shows the FWHM changing by lowering temperature, it stays constantly from room temperature to 220 K, and slightly increases from 220-200 K due to FST in liquid state. Below 200 K to 180 K, the FWHM has a drastic increase in 20 K which indicates the dipolar interaction are significant at low temperature.

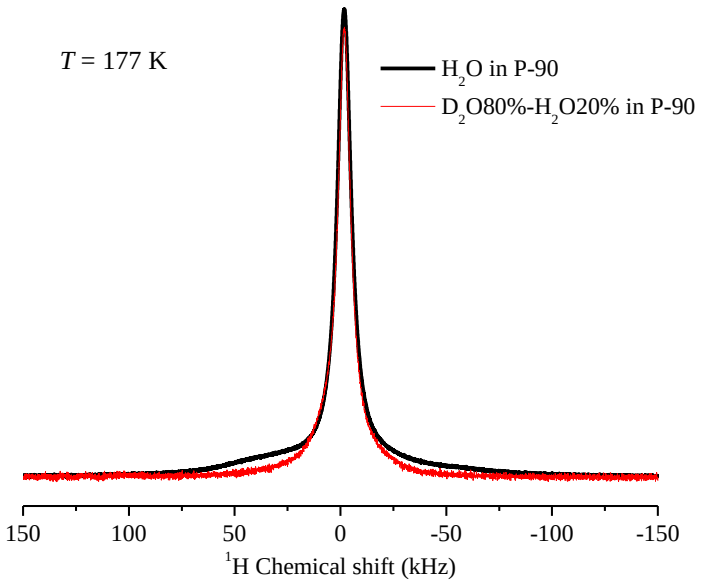

Figure 4.3 Comparison of pure water and mixed water confined in P-90 at T = 177 K.

Figure 4.3 is a supplementary figure to demonstrate the homogeneous broadening of the bottom broad peak. We compare the pure water confined in P-90 and mixed water confined in P-90 at 177 K. The mixed water sample is prepared by 80% D_2O+20%H_2O in molar ratio, it greatly reduces the intermolecular proton-proton dipolar interaction. All H_2O is replaced by HDO, since the exchange rate between H-O and D-O is so fast, so it still remains intramolecular

proton-proton dipolar interaction in NMR time scale. The advantage to use mixed sample is to reduce the intermolecular dipolar interaction and examine the reason for spectrum broadening. By comparing the two "water" in P-90 at same temperature, the spectrum for mixed water in P-90 doesn't have a asymmetric peak growth from bottom obviously, while the pure water in P-90 has. This is the evidence that the broadening of bottom peak is mainly due to the strong intermolecular dipolar interaction.

To fully understand the change of FWHM, it is necessary to discuss the dynamic properties of confined water below 200 K.

4.2.2 T_1 relaxation and rotational diffusion discussion

The T_1 relaxation measurements for confined water reveals the rotational motion of water molecules under confinement. Above 200 K, as discussed in chapter 2, the T_1 relaxation time represents the overall relaxation time for liquid state of confined water. For T_1 relaxation time below 200 K, due to the formation of amorphous ice which cannot be refocused by 180° pulses, the T_1 represents the overall spin-lattice relaxation time of the centered sharp peak which is the LDL. A conventional understanding for glass transition mechanism is the rotational motion slowing down and translational motion stopped in the formation of glassy state [124].

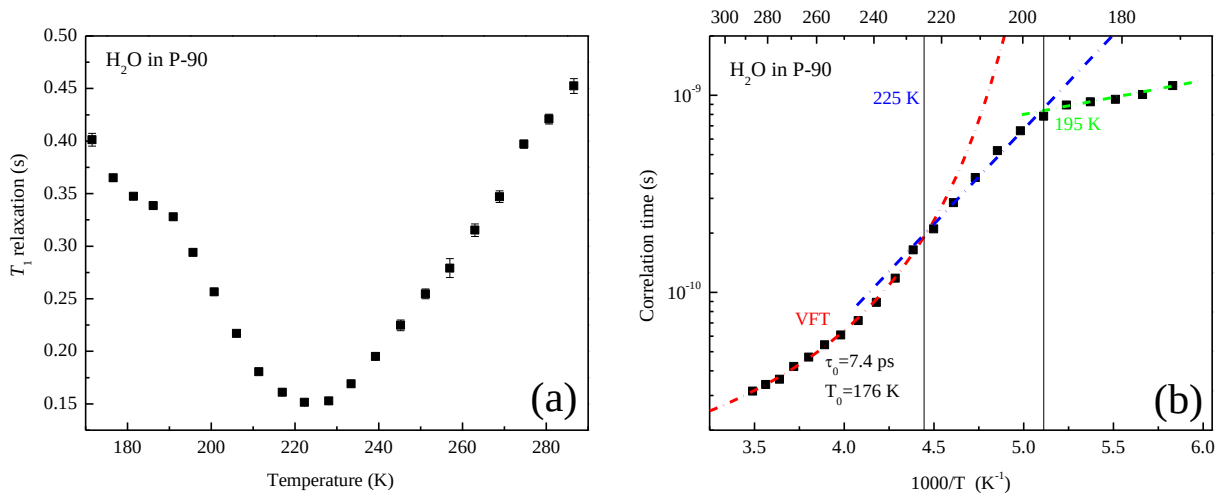

Figure 4.4 (a) Temperature dependence of the ^{1}H NMR spin-lattice relaxation time T_1 for water in P-90 (b) Correlation time of water in P-90 versus temperatures. The red dash dot line is the VFT fitting for the high temperature regime data with $T_0 = 176$ K and $\tau_0 = 7.4$ ps. The blue dash dot line and green dash dot line is the guideline for Arrhenius fitting.

The T_1 values of confined liquid water at 200-170 K are shown in **Figure 4.4** (a). There is a kink at around 190 K. The T_1 below 200 K is only measuring the center sharp peak not the whole spectrum, since the bottom peak is too broad to be flipped by 180° pulse. So, in temperature range 200-170 K, the measured T_1 reflects the LDL water which towards to the surface. The correlation time calculated from BPP equation (**Eq. 2.8)** equation plotted versus inverse of temperatures is in **Figure 4.4** (b). It is worthwhile to note that there is a second transition temperature at 195 K for the Arrhenius-Arrhenius transition. Due to the special limitation of nanopores, the amorphous ice formed from center of the pores could not grow infinitely in a narrow range of temperature as bulk glass transition phenomenon. The confinement slows down the quick growth of the amorphous ice. So, the correlation time doesn't increase as the first Arrhenius line (blue dashed line) but follows the second Arrhenius line (green dashed line). This is consistent with the previous spectrum analysis results: below 200 K,

LDL is slowing down the rotational motion and starts to form amorphous ice. The experiment results agree with the conventional glass transition theory.

4.2.3 Size Independent Experiments and Discussion

It is very important to examine how the confinement effect the glass transition. We confined water in two other different pore sizes: activated carbon P-80 with pore size 1.3 nm and activated carbon P-94 with collapsed pores and average pore size 1.8 nm.

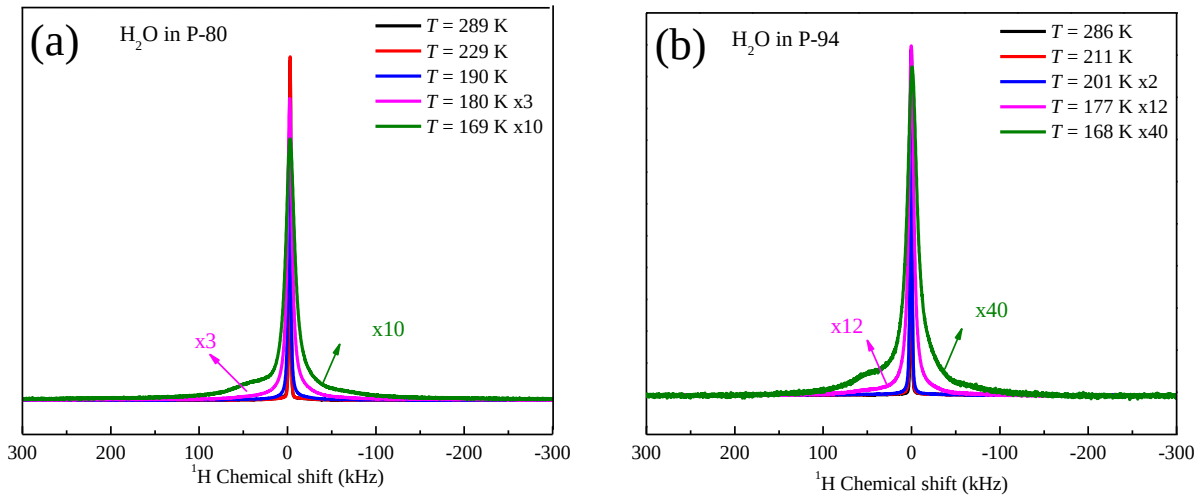

Figure 4.5 (a) Single pulse ^{1}H NMR spectra of water confined in P-80 sample at selected temperatures (b) Single pulse ^{1}H NMR spectra of water confined in P-94 sample at selected temperatures

As discussed in **CHAPTER 2**, the intensity of ^{1}H signal for water confined in P-80 and P-94 won't be lost until 190 K and 210 K which means the confined water stays in liquid state above these temperatures. The asymmetric broad feature grows up when temperature below 190 K and 200 K for water confined in P-80 and P-94 samples. For the water confined in larger nanopores, the intensity lost will happen at higher temperature, the amorphous ice will grow more easily when the liquid became LDL.

The dynamics of water confined in P-80 and P-94 below 200 K is discussed by T_1 relaxation measurements and correlation time calculations.

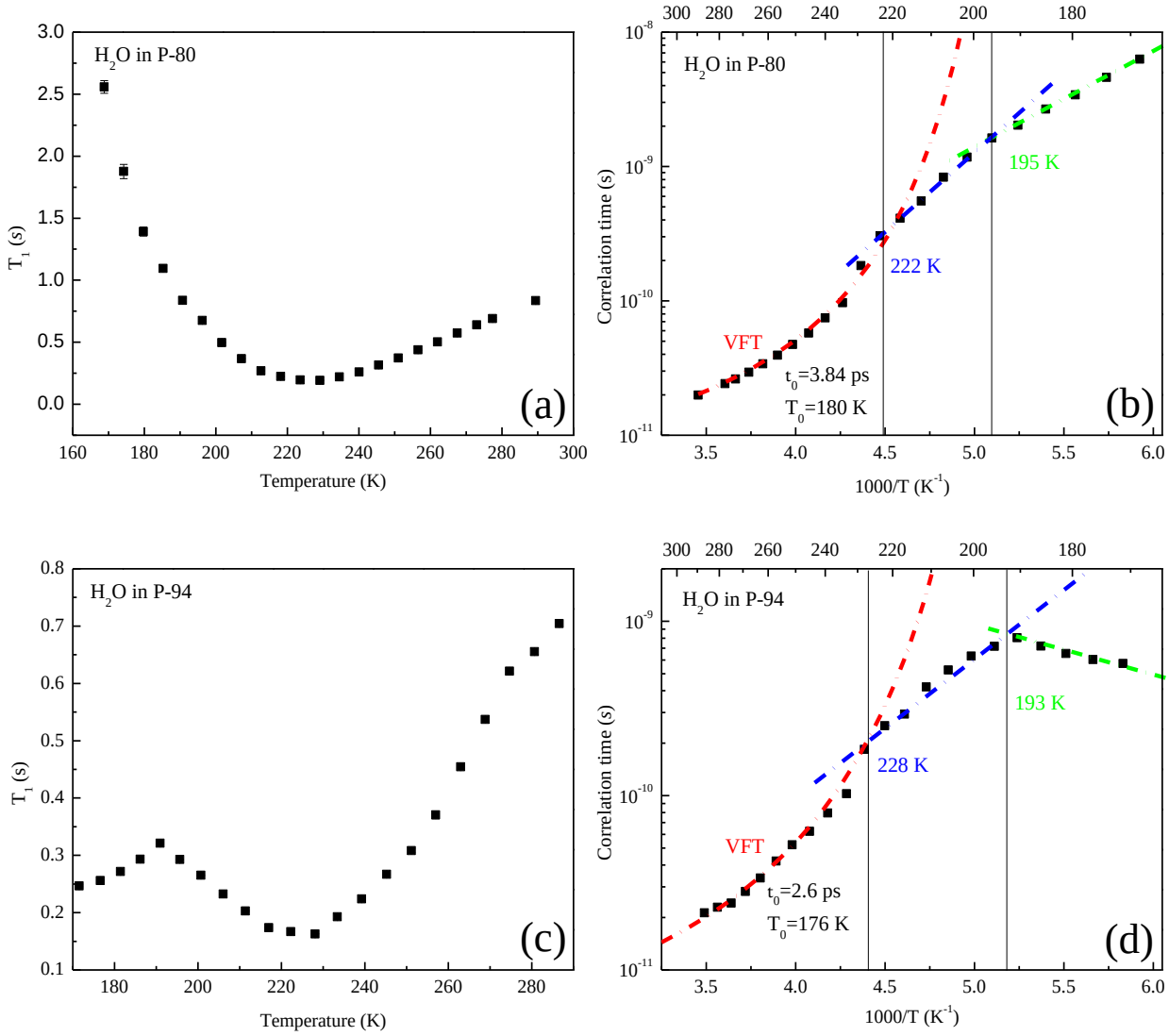

Figure 4.6 (a) T_1 relaxation time for water confined in P-80 versus temperatures. (b) Correlation time of water confined in P-80 sample versus temperatures. (c) T_1 relaxation time for water confined in P-94 versus temperatures. (d) Correlation time of water confined in P-94 versus temperatures

The rotational correlation time of confined water is calculated from **Eq. 2.8** as well. There is also a second Arrhenius-Arrhenius transition temperature at around 195 K. Rotational motion of water molecules changed at 195 K. For water confined in P-80 and P-90, the rotational

motion slows down below 195 K. For water confined in P-94, since the average pore size is 1.8-2 nm and some of the pores are collapsed, the pore structure of P-94 activated carbon sample is difficult to describe. Water will quickly freeze in larger pores below 210 K, so the intensity lost in P-94 is much more than that for water in P-90 and P-80 at low temperature regime. The larger pore size gives more space to grow the amorphous ice in the pores. So, the T_1 measured below 200 K is more associated with the interfacial water which has faster rotation, corresponding to shorter correlation time. All of these are reflecting that the bulk water could have rotational glass transition at 195 K to form amorphous ice if it could be supercooled in the "no man's land".

4.3 CONCLUSION

In this chapter, we discuss about the observation of possible rotational glass transition for water. It is of importance to emphasis that at 200 K, water is completely in LDL state. It disproves the idea that LDL is impossible to exist at low temperature stably. Furthermore, in our spectra analysis, LDL is unlike coarse-grained ice (as amorphous ice), it still has fast rotational and translational motion. It also indicates the LDL is amorphous ice glass-form liquid. The slowing down tumbling motion and growth of amorphous ice show the possible rotational glass transition for water could happen at around 195 K which is much higher than the previous estimated temperature.

CHAPTER 5 INTERFACIAL WATER INDUCED GLASS TRANSTION

5.1 INTRODUCTION

In Chapter 4, we discussed possible water glass transition by confining water in nanopore at temperature range 200 K-170 K. As we mentioned in Chapter 2, we also observe an endothermic shoulder at 150 K for confined water. Angel discussed such similar endothermic shoulder for C_{60}, it is defined as the phenomenon of rotational glass transition [104]. For their inorganic glasses analysis, Angel corrected the water glass transition temperature from 136 K to 150 K [102]. However, Lorenting argued this point and insisted the true glass transition for water is still around 136 K [103]. So, it is of importance to clarify the physics of our observation on 150 K for confined water.

In this chapter, we applied DSC experiments for water confined in different burn off activated carbon samples. The results show for water confined in less than 1nm pores, there is no such endothermic shoulder on the specific heat capacity C_P curve, while for water confined in larger than 1nm pores, the endothermic shoulder onset temperature changes by varying cooling/heating rate which indicates a glass transition phenomenon. We found when the confined water forms **'surface/interfacial water/center water'** such sandwich structure, it could have a glass transition at low temperature region.

5.2 EXPERIMENT RESULTS AND DISCUSSION

We applied DSC and NMR single pulse measurements mainly on the water in P-90 sample. To discuss the properties and physical meaning behind the asymmetric broad peak (see

Figure 5.1 (b)), we used hole burning pulse to test the correlation of two peaks in the spectrum. Also, to study the "sandwich" structure, we also confined water in different pore sizes such as P-40/60/80/94 to investigate how the confinement would affect the thermodynamics of water at low temperature by performing DSC and NMR.

5.2.1 ^{1}H NMR Spectra Analysis

Firstly, we performed NMR single pulse measurement to examine the state of confined water. We choose a RF pulse with highest power and short pulse length 0.5 μs to excite all the spins in the labtoray window (2 MHz).

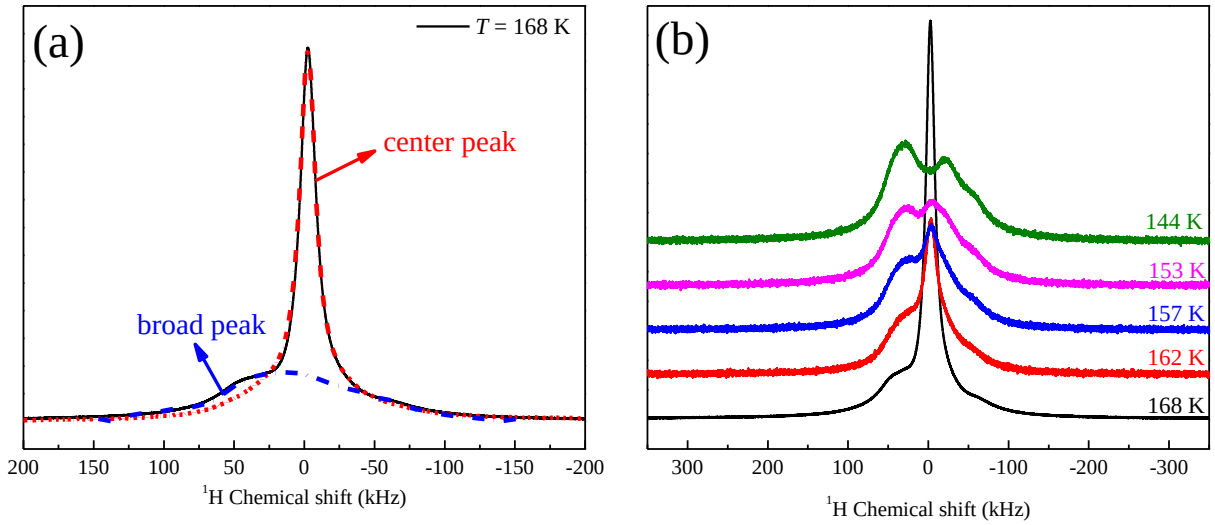

Figure 5.1 (a) ^{1}H NMR spectrum of water in P-90 at $T = 168$ K. Black solid line is the experimental data. Red dash dot line is the fitted Lorentzian peak, blue dash dot line is the residual of subtraction of experimental data and fitted Lorentzian peak (b) ^{1}H NMR spectra of water in P-90 at selected temperatures.

As shown in **Figure 5.1**(a), the peak could be divided into two parts: center sharp peak represents confined water towards to the surfaces remaining liquid state, bottom broad asymmetric peak represents the amorphous ice formed from the center of the silt pores. When cooling the confined water lower than 168 K, the center sharp peak quickly disappeared and the

broad asymmetric bottom peak splits to two asymmetric broad peaks. It is questionable that the two split peaks represent the same state of amorphous ice but anisotropic rotation or two different states of amorphous ice. The hole burning experiment (see **section 5.2.2**) proved the 'doublet' represents the same state of amorphous ice but anisotropic rotation.

Furthermore, the drastic disappearance of the center peak and quick growth of the bottom peak indicates a possible glass transition for the confined water below 160 K. In **section 5.2.3**, the analysis of DSC measurements will show there is a interfacial water induced glass transition at150 K.

5.2.2 Hole Burning Experiments and Discussion

The hole burning experiment is used to determine the inhomogeneity properties of field or samples. As we introduced in **CHAPTER 2**, if the linewidth broadening is due to the spin interaction, it won't burn a hole after applying HB pulse sequence. If it is due to the field inhomogeneity or different susceptibility of samples, it could burn a hole as shown in **Figure 5.2**.

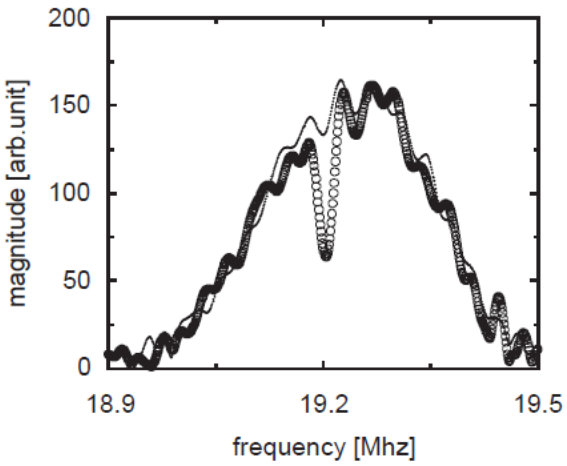

Figure 5.2 Spectrum of the hole-burning echo of pure water (open symbols) and of the Hahn echo (solid line) recorded under similar conditions. The oscillations are a Gibbs ringing artifact. [100]

The HB pulse sequence is shown in **Figure 2.8** (in **CHAPTER 2**). Roughly speaking, a soft pulse with low power level (PLW2) and long pulse length (P1), following a hard pulse with high power level (PLW2) and short pulse length (P1). **Table 5.1** shows the HB experiment parameter set up in our experiments.

Table 5.1 Numbers and Parameters for the hole burning experiments for water confined in P-90 at 144 K

Number	**SFO1(*MHz*)**	**PLW1**	**P1(μs)**	**PLW2**	**P2 (μs)**	**D1(*s*)**	**D2(*s*)**	**Pulse type**
1	500.7100408	-	-	150	0.5	-	5	Single Pulse
2	500.7100408	0.5	1000	150	0.5	0.5	5	HB
3	500.7100408	0.5	100	150	0.5	0.5	5	HB
4	500.7100408	2	1000	150	0.5	0.5	5	HB
5	500.7100408	2	100	150	0.5	0.5	5	HB
6	500.7100408	0.5	1000	150	0.5	0.1	5	HB

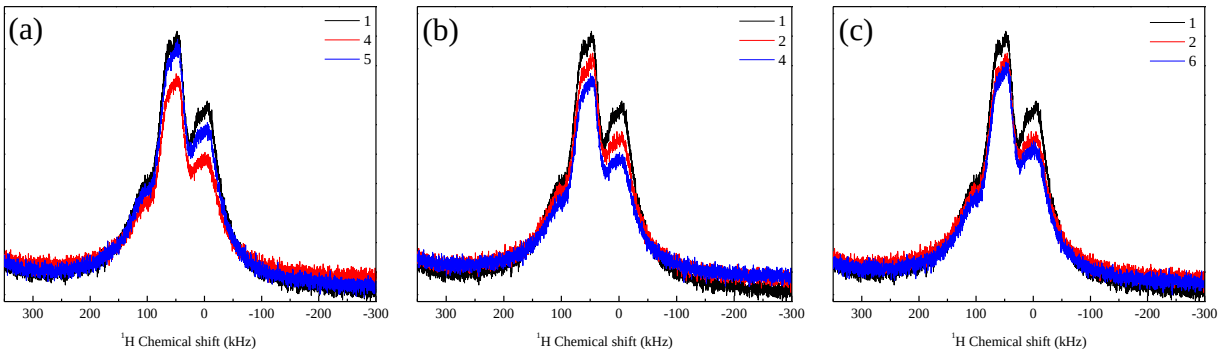

Figure 5.3 Hole burning experimental spectra with different parameters. #1 is the single pulse spectrum at 144 K in highest power

We set all the PLW2 power is 150 in amplitude which is the highest power in the NMR transmitter system and the pulse length P2 of PLW2 is 0.5μs to excited as many spins as possible (2 MHz). The D2 duration time is 5s to make sure all the spins after PLW2 RF perturbation are back to equilibrium state before it goes to the next scan. For the soft pulse in the hole burning experiments, we changed three parameters independently, power level PLW1, pulse length P1, and the duration time D1. We set the center frequency SFO1 focusing on the right peak, so if the splitting of peaks is due to field inhomogeneity, after the HB pulse, it will burn a hole on the right peak. To compare the change before and after HB, we run a single pulse with the same SFO1 as refence.

Firstly, we kept the power level PLW2 the same as weak as 2 in amplitude, change the pulse length as shown in the **Figure 5.3** (a) #4 and #5. The P1 in #4 is 1000 μs which could excite spins located (1/1000 μs) 1 kHz band width around SFO1. The P1 in #5 is 100 μs corresponding to 10 kHz band width around SFO1. The longer pulse length the narrower range of spins around the center frequency SFO1 will be excited and less quantum coherence will be lost during the soft pulse. If the field is inhomogeneity, the width of the hole burnt by long pulse length would be narrower than that burnt by short pulse length (see **Figure 5.4**). Also, the final

signal for longer pulse length will be stronger than the shorter pulse length. Comparing the original single pulse signal #1, HB experiment #4 and #5, there is no hole burnt in the spectrum and the intensity follows the order of the coherence lost. More importantly, the amplitude of the left peak also decreases as the same order of the right peak, which means the spins in the right peak region is coupled with the spins in the left peak region. The right peak and left peak are not representing two different types of spins uncorrelated, but spins in the same state with anisotropic rotational motion.

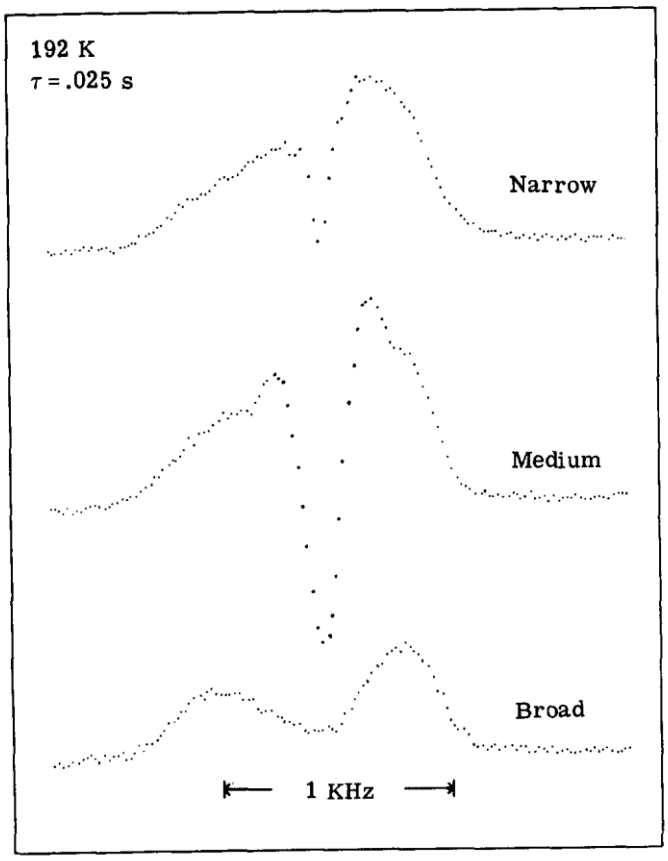

Figure 5.4 HB spectra for glycol in glass transition process. Three figures from top to bottom represent different pulse length applied on the HB pulse. The 'narrow' spectrum used the longest pulse length, and the 'broad' spectrum obtained from the shortest pulse length [129]

Secondly, we kept the pulse length (P1) the same 1000μs but changing the power level. The higher power level PLW2, the stronger perturbation to the system and more coherence will be lost. If the field is inhomogeneity, the hole burnt by a higher power would be deeper than that burnt by a lower power. In our experiment, #2 and #4, applying 0.5 power is less than 2 power, so the total signal for #2 is stronger than #4 (see **Figure 5.3** (b)). However, there is still no hole burnt from the HB pulses and the amplitude for two peaks both dropped.

Thirdly, we remained the pulse power (PLW1) and pulse length (P1) the same but varying the duration time D1. Longer D1, more spins will recover to the equilibrium state, if set D1=5T1, all the spins will come back to the equilibrium state as at the beginning of a single

pulse, the soft pulse is useless for that case. So, the empirical setting parameter of D1 is T2 <D1 <T1 to make sure the excited spins lost the transverse coherence but still has longitudinal coherence. The longer recovery time D1, the spins are more approaching to the equilibrium state and the signal is stronger, if it will burn a hole, the hole will be more shadowed (see **Figure 5.5**). #2 has 5 times longer that #6, so the intensity in #2 is larger than that of #6. The drop of the signal is shown for both peaks.

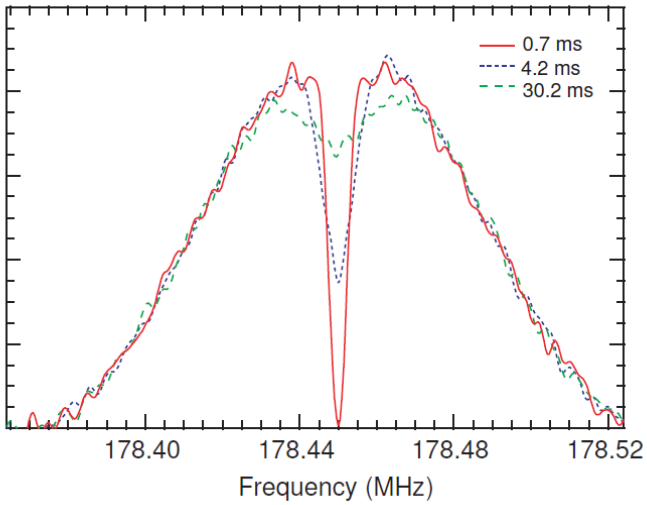

Figure 5.5 HB echo for pure water with different D1[130]

In the hole burning experiments, we change the soft pulse parameter separately. Unfortunately, there is no hole burnt by the pulse. On the contrast, the intensity of left peak decreases with the right peak intensity by HB pulse. The disappearance of holes, means the linewidth broaden is not due to the inhomogeneity of field or sample. The spins in two split peaks are coupled to each other instead of independent. The main reason to explain the doublet and the line broaden is anisotropic motion of H_2O molecules in the amorphous ice. The H_2O molecules in the glassy state reorient the hydrogen bonds such as “flip angel”, but the flip rate is

longer than NMR observation time scale, so it cannot be averaged. In other words, the ‘doublet’ indicate the state of solid formed from LDL is not a rigid lattice crystal but amorphous state.

5.2.3 DSC Analysis and Discussion

DSC is a unique technique to determine the glass transition. For a conventional glass transition phenomenon, when increase the heating rate, the onset glass transition temperature will red shift to higher temperature range, due to lack of time to relax the local structures to equilibrium state.

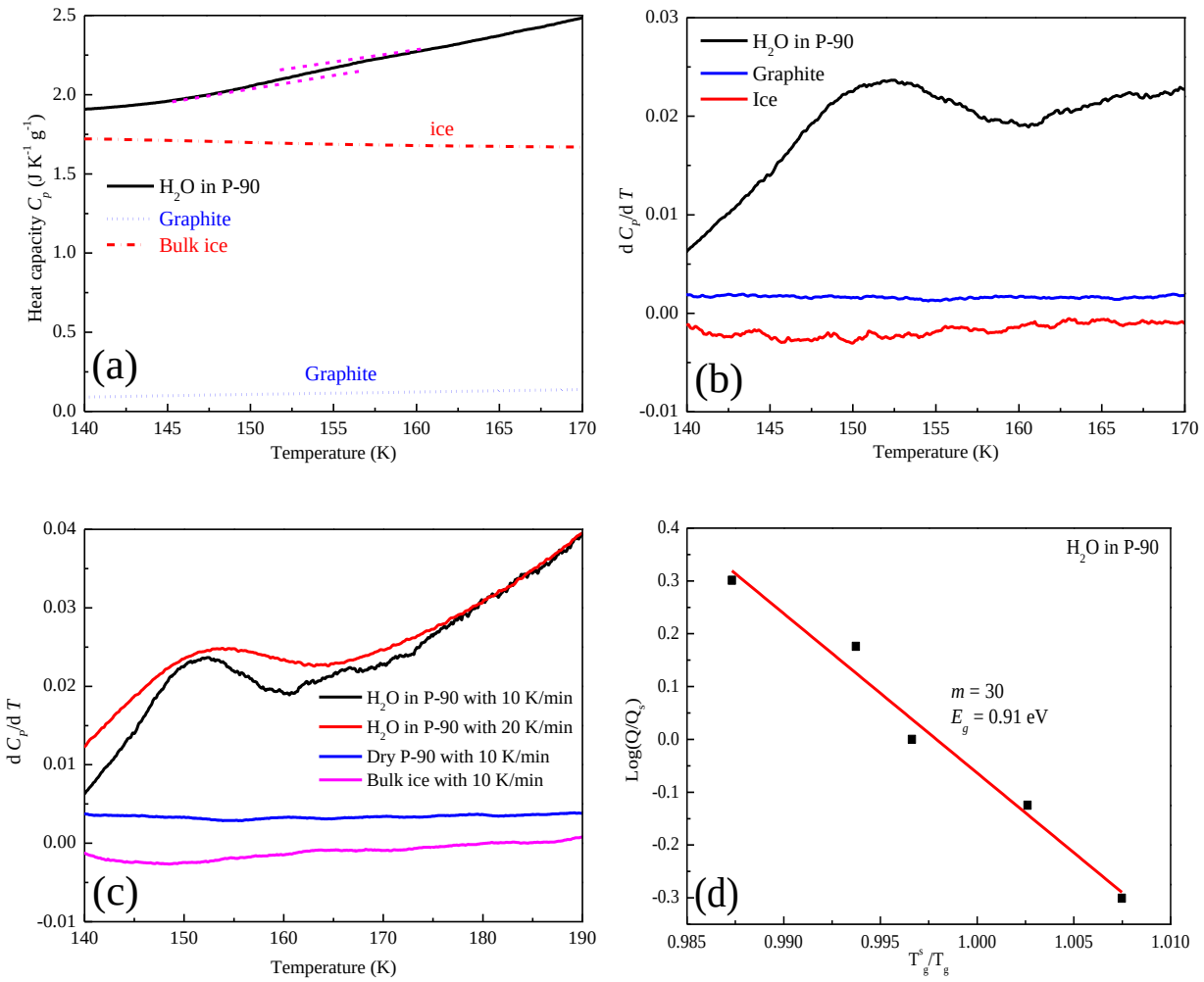

Figure 5.6 (a) Specific heat capacity C_P of H_2O confined in P-90, dry P-90 activated carbon, bulk ice/water. Zoom in the temperature region from 140-190 K from **Figure 3.1**. (b) Derivative of C_P with temperature for H_2O confined in P-90, dry P-90 activated carbon, and bulk ice/water versus temperatures. (c) Derivative of C_P in temperature for water confined in P-90 sample at heating rate 10 K/min and 20 K/min versus temperatures, derivative of C_P in temperature of dry activated carbon and bulk ice with heating rate 10 K/min as reference. (d) Plot of logarithm (Q/Q_s) versus (T_g^s/T_g) and fragility calculation for water confined in P-90 around 150 K

When we zoom in the specific heat of water confined in P-90 measured from DSC experiment, there is an endothermic shoulder around 150 K which is very different from linear increase of specific heat of ice and dry P-90 graphite by temperature, respectively (see **Figure 5.6 (a)**). It is worth to notice that at the end of the DSC measurement close to 140 K, the specific

heat of the confined water is larger than the ice (I_h) which means the "solid-like" formed from supercooled confined water is different from the ice (I_h). The possible reason is the supercooled confined water during cooling process forming amorphous ice which has more degree of freedom than crystal so that the C_P would be larger than crystal structure ice. To determine the endothermic shoulder is the real feature of glassy state of confined water and is different from the bulk ice and graphite, we took the derivative of C_P and temperature, as shown in **Figure 5.6 (b)**, obviously, for the C_P of water confined in P-90 there is a clear peak around 152 K, meanwhile, for the bulk ice and dry graphite, the derivative results are almost a flat line around 0. This calculation shows the endothermic shoulder is heat adsorption change of confined water. We selected different heating rate from 5 K/min to 20 K/min on the samples. The heat capacity of bulk ice/water and dry graphite C_P do not change by applying different heating rates. For the water confined in P-90 the center of the endothermic shoulder shifted by changing the heating rate. To examine into detail and for comparison, we selected two different heating rate 10 K/min and 20 K/min for water confined in P-90 DSC experiments and took derivative of C_P and temperature listed in **Figure 5.6 (c)**. For the heating rate 10 K/min DSC experiment, the peak at 152 K is sharper and clearer due to slower heating rate and longer time for structure relaxation of the amorphous state of confined water. For the heating rate 20 K/min of water confined in P-90 sample, the peak is broader and centered at 154 K which represent for the fast heating rate, the system doesn't have enough time to relax the structure. For this sign, it shows the glass transition happened in the confined water. By taking derivative of C_P and temperature at different heating rate, we read out a serious of onset glass transition temperature. We selected 10 K/min as reference heating rate as Q_s and the onset glass transition temperature at 10 K/min as reference glass transition temperature T_g^s. Q and T_g are representing the other heating rate and the onset

glass transition temperatures read from the heating rates respectively. Plot the logarithm Q/Q_s versus T_g^s/T_g , the fragility calculated from **Eq.2.16** is obtained from the slope which is 30 in this case, and the glass transition activation energy is calculated by obtaining the intercept in **Eq. 2.16** which is equal to 0.91 eV in this case. For the fragility smaller than 50, it would consider such glass forming liquid is a strong liquid. So, the low-density water is a strong liquid, instead of the fragile liquid for high-density liquid. This conclusion is consistent with the simulation results and theory.

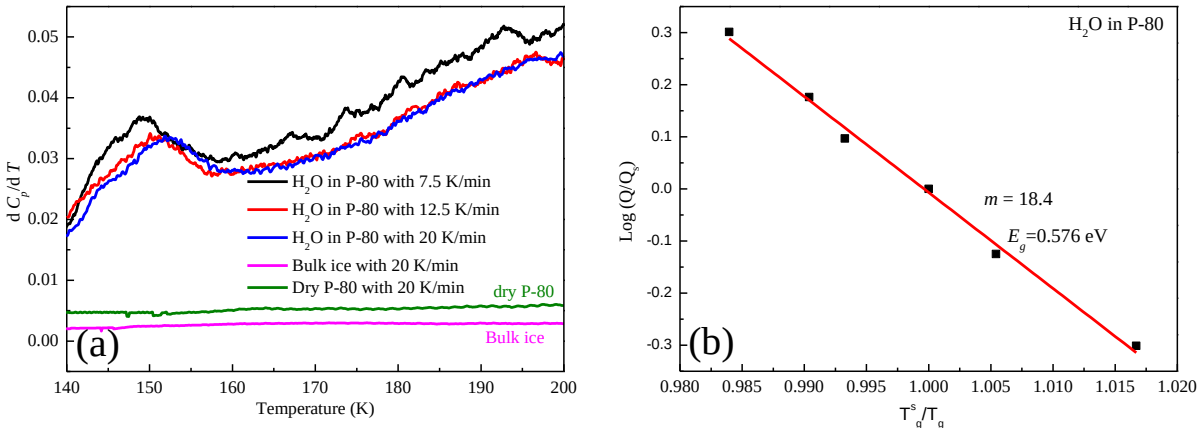

Figure 5.7 (a) Derivative of C_P in temperature of water confined in P-80 sample with heating rate 7.5 K/min, 12.5 K/min, 20 K/min. Derivative of C_P in temperature for bulk ice and dry P-80 activated carbon with heating rate 20 K/min as reference. (b) Plot of logarithm (Q/Q_s) versus (T_g^s/T_g) and fragility calculation for water confined in P-80

Similarly, for water confined in P-80 AC sample, we applied the same analysis process and get the fragility 18.4 for glass-forming supercooled LDL, which also indicates a strong liquid, consistently.

To discuss the driven force and physics behind such glass transition, we also examine the C_P of water confined in different pore sizes variant from 0.9nm to 1.8 nm (see **Figure 5.8**). For water confined in P-40 which has pore size 0.9 nm, there is only 2-3 layers of water in the P-40

slit pores, without existence of centered bulk-like water. For water confined in P-60 with pore size 1.05 nm, there is at least one layer of water staying in the center of pores besides two interfacial layers of water. And for water stay in P-80/90/94, more and more layers of water could exist in the center of pores. The properties of confined water are close to bulk water.

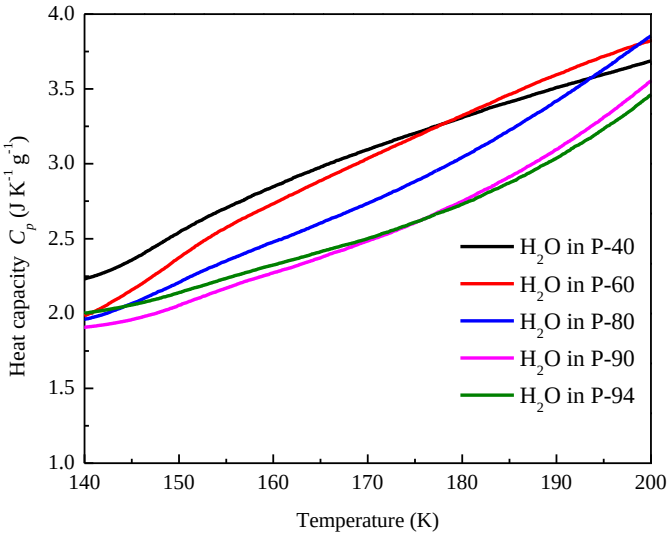

Figure 5.8 Specific heat C_P of water confined in different activated carbon samples with heating rate 10 K/min

From the DSC result and analysis of C_P for water confined in different pores, we found, for water confined in smaller than 1 nm pores, there is not endothermic shoulder at 150 K and the decrease of C_P is convex. For water confined larger than 1 nm pores which have sufficient center bulk-like water, there is an endothermic shoulder around 150 K. For water confined in P-94 AC which some pores are collapsed to larger pores (>2nm), the endothermic shoulder becomes smear and cannot get the fragility quantitatively.

5.2.4 Comparison ^{1}H NMR Spectra for Water in Different Pore Sizes at T=144 K

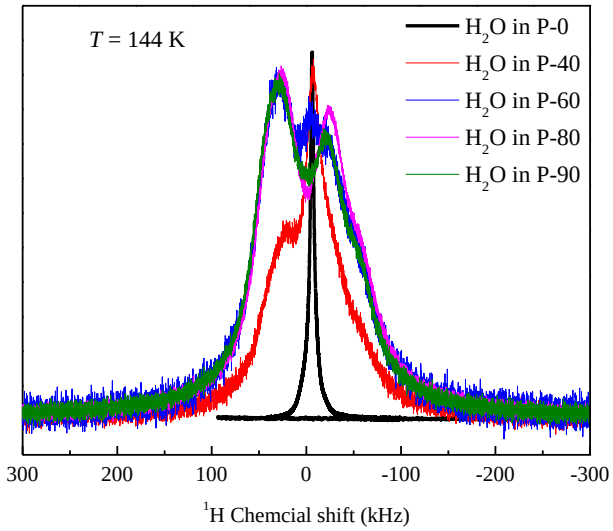

Figure 5.9 ^{1}H NMR spectra of water confined in different pore sizes at $T = 144$ K

To study the state of confined water in different pores, we applied NMR single pulse experiment for these samples at 144 K (see **Figure 5.9**). The pore sizes increase from 0.46nm (P-0) to 1.6nm (P-90), the number of lays of water confined in the slit-pores are from monolayer up to 6 layers. The stacked spectra in **Figure 5.9** shows the water confined in larger pores, the drop of the centered water is more thoroughly, especially, for the monolayer water in P-0 sample, the ^{1}H NMR spectrum at 144 K has FWHM 10 kHz, which means the monolayer water is still in liquid state at low temperature. For the water confined in P-40 which has 3 layers of water, the spectrum is a combination of center sharp peak which represents the unfrozen water towards to the surface and asymmetric broad peak from bottom which represents amorphous ice formed from center bulk-like water, however, the center peak is broader than the spectrum of water in P-0, and the broad asymmetric peak is narrower than the spectra of water in P-60/80/90. That means the rational motion of center water is slower than the interfacial monolayer water. The distinguish difference means not all the water confined in nanopores will occur second glass

transition. Only form “surface/interfacial water/‘bulk-like’water” sandwich structure could have such “glass transition”.

5.3 CONCLUSION

In this chapter, we examine the state of confined water from 170 K to 140 K. For water confined in pore size larger than 1.3 nm nanopores, all LDL converts to amorphous ice at 144 K and have a glass transition at 150 K due to quick loss of LDL. For water confined in smaller or equal 1nm pores, LDL could survive until extremely low temperature and there is no glass transition observed at 150 K. So we conclude the glass transition at 150 K is induced by interfacial water only when confined water forms ‘surface/interfacial water/center water’ sandwich structure.

CHAPTER 6 OUTLOOK RESEARCH FOR INTERFACIAL LIQUID

6.1 INTRODUCTION

The nature of interfacial water plays a crucial role in lots of natural processes, such as lipid aggregation, joints lubrication, and underwater gecko adhesion [111, 112, 131]. Many experiments such as surface force apparatus (SFA) measurements and MD simulations [132] prove under nanoconfinement, the physical properties that differ from bulk water. A simple example is for water confined in hydrophobic surfaces won't freeze at low temperature. However, the direct evidence of the structure of interfacial water, particularly, the state of hydrogen bonding network of the interfacial water is lacking. Also, the dynamic properties of interfacial water are still unclear for now.

In this chapter, we will discuss the thermodynamics, dynamics and structure of interfacial water by applying DSC, NMR and MD simulation.

6.2 EXPERIMENTAL RESULTS AND DISCUSSION

We applied DSC and NMR experimental methods to discuss the thermodynamics and dynamics of water confined in P-0 sample which has average pore size around 0.46 nm from carbon surface to surface. Such small pore size only allows single layer of water confined in the slit-pores. The diffusion in vertical direction is highly constrained by such 2D confinement. The single layer of water has interactions from both sides of surfaces. It would prospect that the state of water would be totally different with multilayers water confined in larger pores such as P-90 which has pore size around 1.6 nm as we discussed before.

6.2.1 Thermodynamics of Water Confined in P-0 AC

To discuss the thermodynamic property of confined water, DSC is a powerful technique to examine the phase transition and glass transition phenomenon. We applied DSC measurements on water confined in P-0, dry P-0 sample and bulk water with cooling and heating rate 20 K/min to investigate the state of confined water.

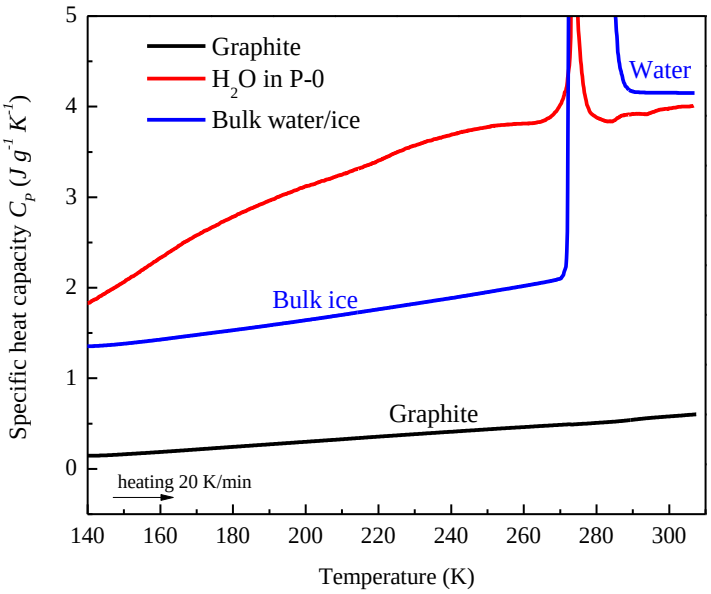

Figure 6.1 Specific heat capacity C_P of water confined in P-0 activated carbon, dry graphite, and bulk water/ice from 300 K to 140 K. Red solid line is the C_P of water confined in P-0, blue dash dot line represents the C_P of bulk water/ice, and black dot line represents C_P of dry P-0

As shown in **Figure 6.1**, the C_P of single layer water has an adsorption peak at 270 K and a decrease of C_P from 270 K to 140 K in a convex shape. Comparing to the bulk water specific heat, the endothermic peak at 270 K for confined water is due to the melting of water absorbed in the intergranular pores. It is important to point out that the C_P of monolayer water at room temperature is less than C_P of bulk water, which indicates the confined monolayer water has less degree of freedom than bulk water. Meanwhile, at 140 K, the C_P of confined monolayer water is

much larger than that of bulk ice, even larger than water confined in P-90 sample. That means, the confined monolayer water still has fast motion and not form ice at low temperature.

Unlike the water confined in P-90 pores, the monolayer water doesn't have a second endothermic peak at 230 K and neither an endothermic shoulder around 150 K. The further study shows, for the monolayer water, it does not freeze at very low temperatures and the mild drop of C_P is due to the slowing down rotational motion of monolayer water.

6.2.2 State of Interfacial Water

We performed NMR single pulse measurements to study the state of monolayer water at different temperatures.

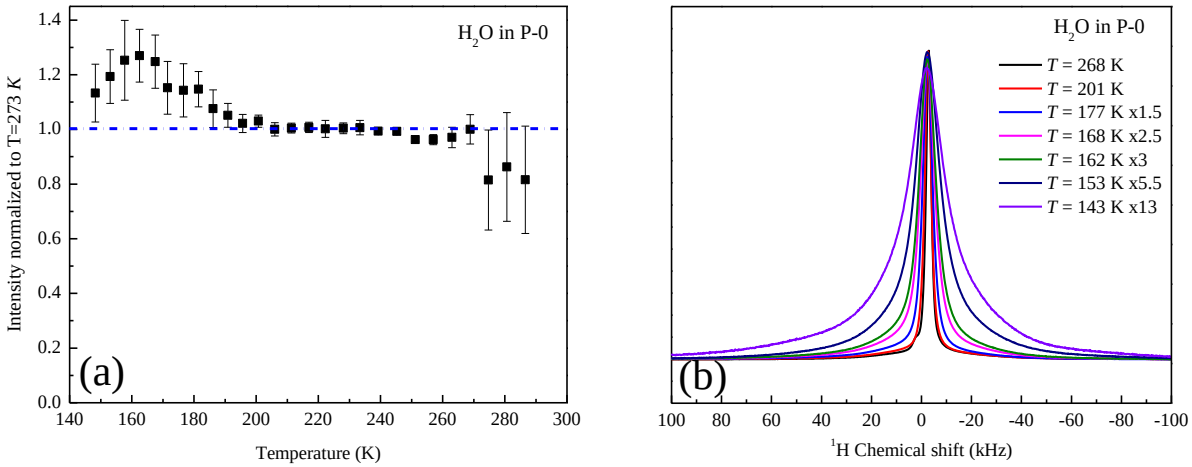

Figure 6.2 (a) Normalized intensity of ^{1}H NMR results of water confined in P-0 versus temperatures. (b)^{1}H NMR single pulse spectra of water confined in P-0 at different temperatures

The ^{1}H NMR intensity is proportional to the total number of ^{1}H spins detected. **Figure 6.2** (a) shows there is no intensity loss in the whole temperature range which means no freezing happened even at temperature as low as 140 K. The increase of normalized intensity from 180-140 K is due to the uncertainty created by extrapolation method. The examples of ^{1}H NMR spectra of water in P-0 at different temperatures are listed in **Figure 6.2** (b). The FWHM of spectra is getting broader by decreasing temperature. However, there is no "doublet" growth

from the bottom of spectrum. These observations show that the interfacial water remains in liquid state but slows down the molecule motions instead of forming other states.

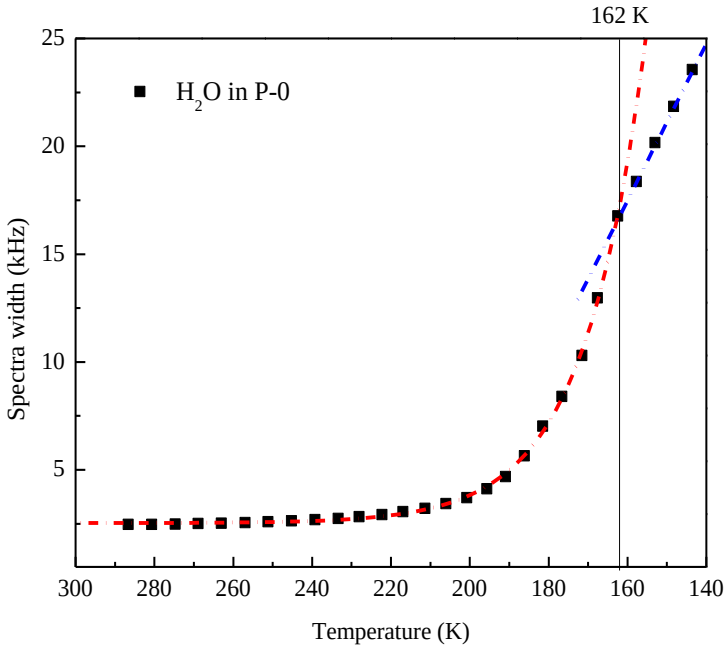

Figure 6.3 Spectra width of ^{1}H NMR spectra of water confined in P-0. Red dash dot line and blue dash dot line are guideline for data reading

The NMR spectra width partially reflects the intra- and inter- molecular dipolar interactions which is related to the motion of water molecules. We plotted the spectra width versus temperatures in **Figure 6.3**. For the water confined in the nanopores, at high temperature, above 200 K, the spectra width remains less than 4 kHz, which is due to the nanopore size distribution and that means the monolayer water has fast motions in the small pores. At low temperature region, while the dipolar interaction contributes to the spectra width. For example, by decreasing the temperature, the motion of water molecules slows down, the intra- and inter-molecular dipolar interaction become significant, the spectrum width grows broader. However, it doesn't quickly grow to the static limit 32 kHz for water molecules, in contrary, below 162 K, the quick growth stopped and the linewidth increases almost linearly. At the end of the

experiment, at 144 K, the spectrum remains a single peak with 25 kHz in FWHM. This observation agrees with the previous conclusion: there is no solid or glassy state formed during cooling the interfacial water, and the water molecule still has some mobility even at such low temperature.

6.2.3 Dynamics of Interfacial Water

To further discuss the dynamic properties of monolayer water, we performed T_1 and T_2 relaxation measurements for the water confined in P-0 sample. We applied two different types of T_2 relaxation measurements, CPMG measurement and Hahnecho measurement. As we mentioned in **CHAPTER 2**, CPMG method could greatly reduce the diffusion effect and more reflect the intrinsic translational motion. On the other words, Hahnecho method with only one echo pulse could reflect the molecular diffusion in the pores. To compare CPMG T_2 and Hahnecho T_2, it would give an idea about the how the diffusion changes by temperatures.

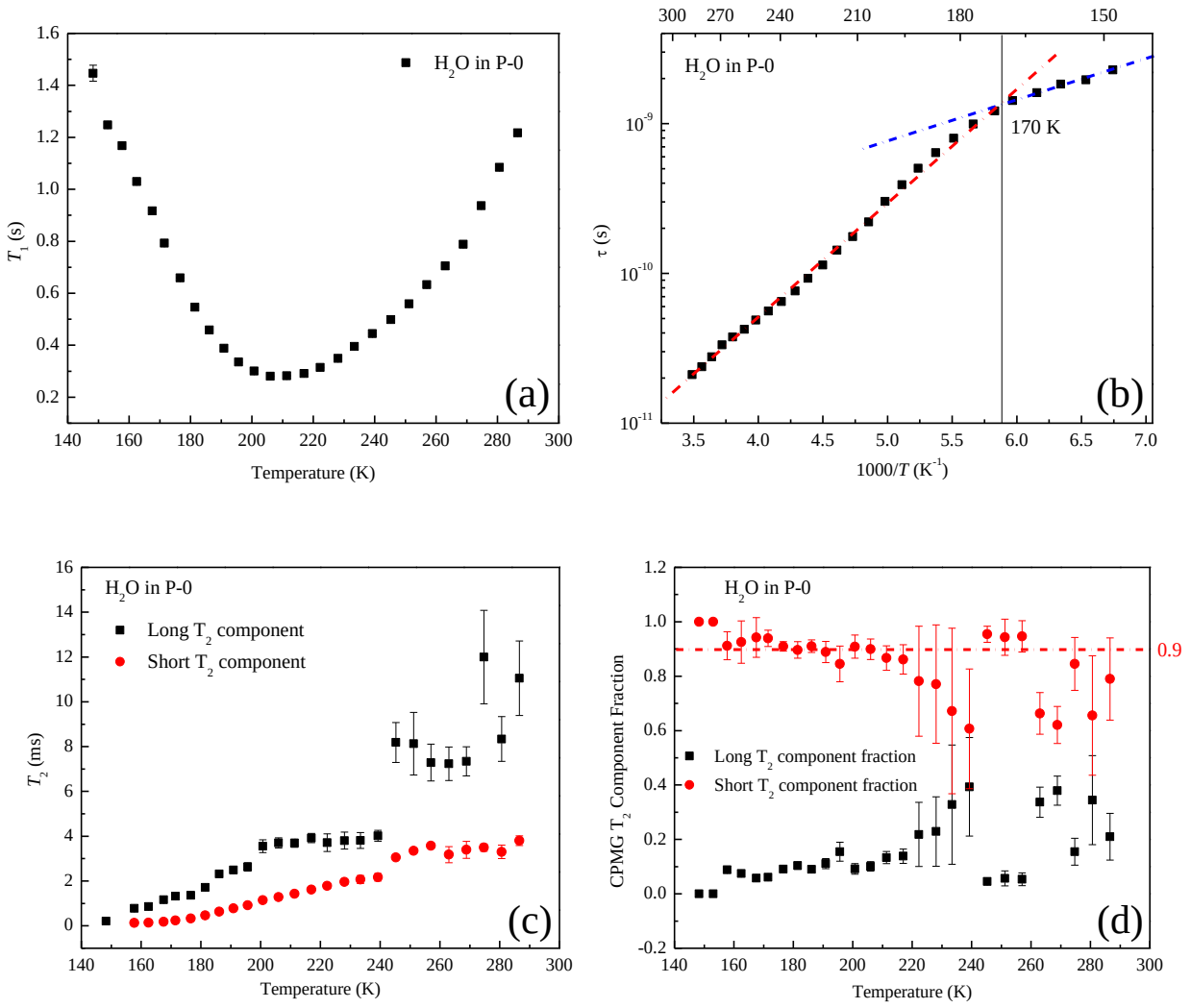

Figure 6.4 (a) T_1 of water confined in P-0 versus temperatures. (b) Correlation time of water confined in P-0 versus temperatures. (c) T_2 of water confined in P-0 measured by CPMG method versus temperatures. (d) Fraction of long and short component of T_2 for water confined in P-0 versus temperatures.

We applied inversion recovery method to measure T_1 relaxation time. The $M(t)$ obtained from T_1 measurement could be fitted in single exponential decay equation perfectly. There is a T_1 minimum at 205 K (see **Figure 6.4 (a)**), the correlation time calculated from BPP **Eq. (2.8)** plotted by temperature is in **Figure 6.4 (b)**. At high temperature region, the interfacial water is more like an Arrhenius liquid instead of VFT liquid as bulk water. And there is only one

Arrhenius to Arrhenius transition at 170 K which coincides with the cross-section temperature 162 K in spectra width analysis (See **Figure 6.3**).

The T_2 relaxation measured by CPMG method still has two components, long and short T_2 relaxation time. The difference between long and short T_2 is not distinguish, less than an order in magnitude. By decreasing the temperature, T_2 for both long and short component are dropped but not drastically. The fraction of these two components versus temperature are plotted in **Figure 6.4 (d)**, there is no such HDL to LDL conversion observed as water confined in P-90 (See **Figure 3.14 (a)**), while the fraction of short component T_2 stays around 0.9 and the fraction of long component T_2 stays at 0.1 stably.

The two components in T_2 measurements mean it has two physical environments for all the spins. It has two explanations: one is there are "two phases" stably exists for the interfacial water, the other is spins stay in two different pores. Due to the T_2 value for long and short components are not significantly different and it does have pore size distribution. The more reasonable understanding for the two components is due to the nanopore inhomogeneity.

6.2.4 Comparison of CPMG T_2 and Hahnecho T_2

Since the diffusion of interfacial water on vertical direction is restricted by surfaces, it is important to discuss the diffusion on lateral direction. By comparing CPMG T_2 and Hahnecho T_2, it could tell the translational motion of interfacial molecules.

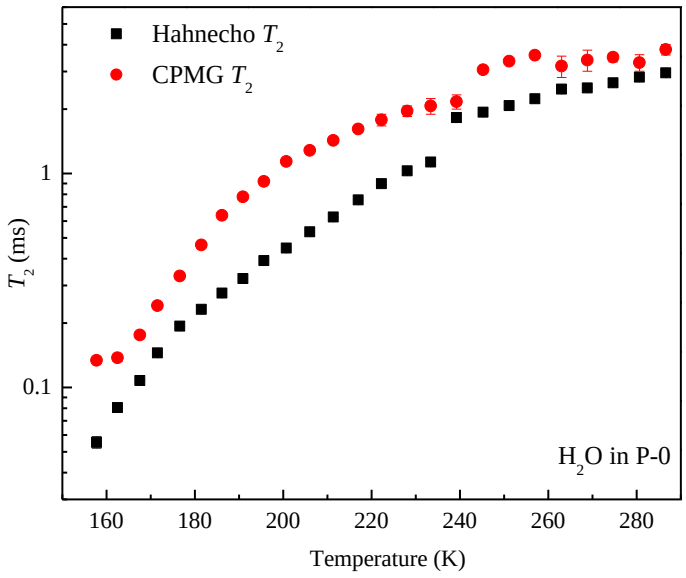

Figure 6.5 Comparison of Hahnecho T_2 (short component) and CPMG T_2 (short component) for water confined in P-0 sample

We noticed, the magnitude difference between CPMG T_2 and Hahnecho T_2 are less than 3 times. At most temperature, there is no big difference between these two T_2 values. This phenomenon indicates the lateral translational diffusion for interfacial water molecules in the pores are much less mobile than bulk water.

6.3 CONCLUSION

In this chapter, the properties of interfacial water are studied by DSC and NMR measurements. We found for the water on hydrophobic surfaces, it will not freeze at low temperature and keep fast rotational motion. Thermodynamically, the interfacial water will remain liquid state without crystallization or glass transition from room temperature to low temperature. Dynamically, there is an Arrhenius to Arrhenius transition at 170 K due to slowing down the rotational motion of interfacial water molecules. Comparing to the bulk water motion,

our results show that for the water on the hydrophobic surfaces, it displays much slower orientationally dynamics than the bulk water and effectively immobilized.

However, for more details about hydrogen bonding network for the interfacial water, it requires femtosecond FTIR or Raman spectroscopy methods to investigate the O-H bond and vibration modes. We also need MD simulations to understand more about the structure of interfacial water.

APPENDIX A

A1. ^{1}H NMR spectra for water confined in P-90 sample at $T = 289\ K$ and $T = 268\ K$

Sample is prepared by injecting water into dry P-90 sample setting in the 4mm rotor. We applied ^{1}H MAS NMR on the sample at two different temperatures.

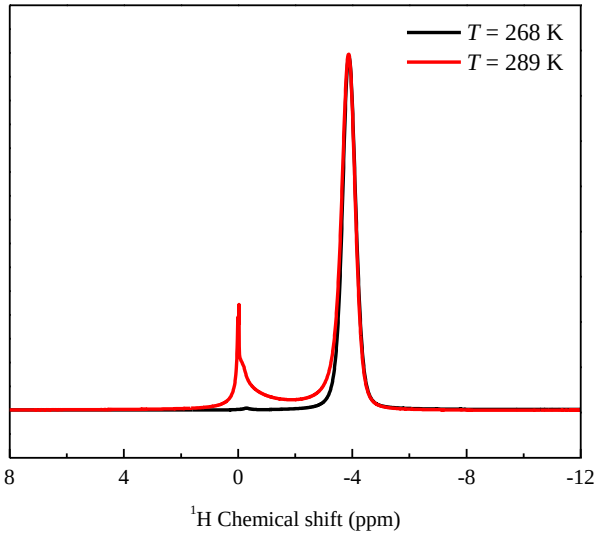

Figure A.1 ^{1}H MAS spectra for water confined in P-90 at T = 289 K and T = 268 K

At room temperature, there are two peaks in the spectrum, the left peak represents the water stays in the intergranular space and the right peak represents nanoconfined water. At $T =$ 268 K, only right peak survived, the left peak disappeared due to crystallization happened in the larger pores.

The NMR result consistent with the DSC observation: at 268 K, there is an endothermic peak on the C_P curve, which is due to the crystallization of water in the intergranular space.

A2. NMR Results Analysis for Water in P-60 AC

From NMR intensity analysis, the water confined in P-60 doesn't crystallize until below 170 K.

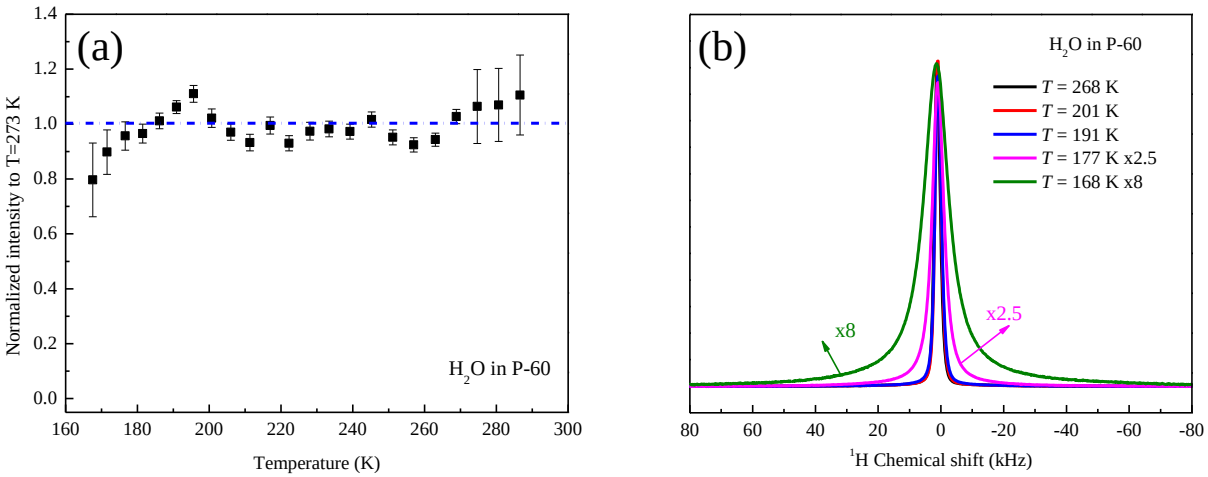

Figure A.2 (a) Normalized intensity of water in P-60 versus temperatures. (b) ^{1}H NMR spectra of water in P-60 at selected temperatures.

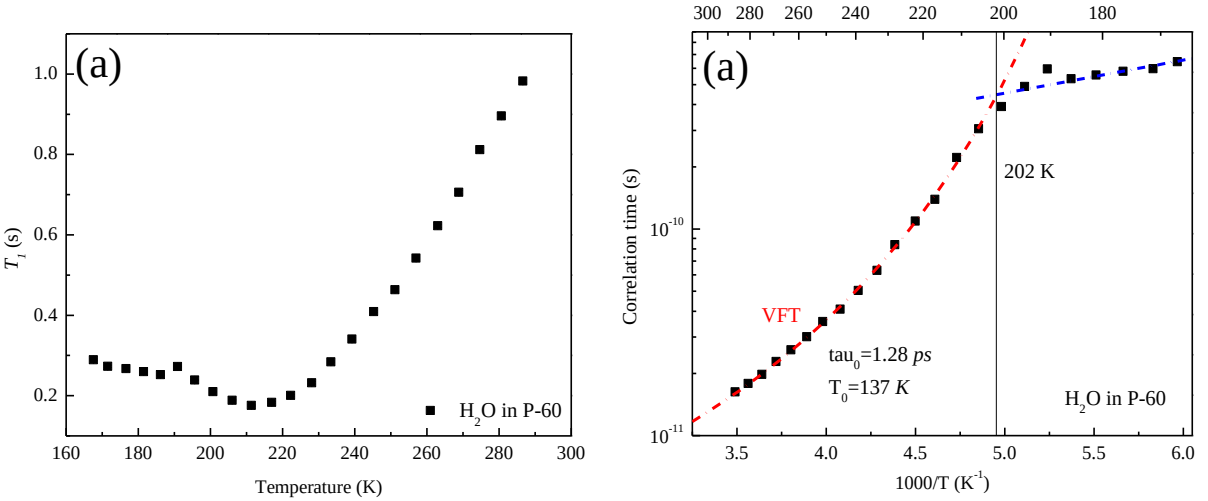

Figure A.3 (a) T_1 relaxation time for water in P-60 AC versus temperatures. (b) correlation time of water confined in P-60 versus temperatures

From NMR T_1 relaxation measurement and correlation time analysis, we found for water confined in P-60, there exists a VFT to Arrhenius transition at 202 K which the confined water still in liquid state.

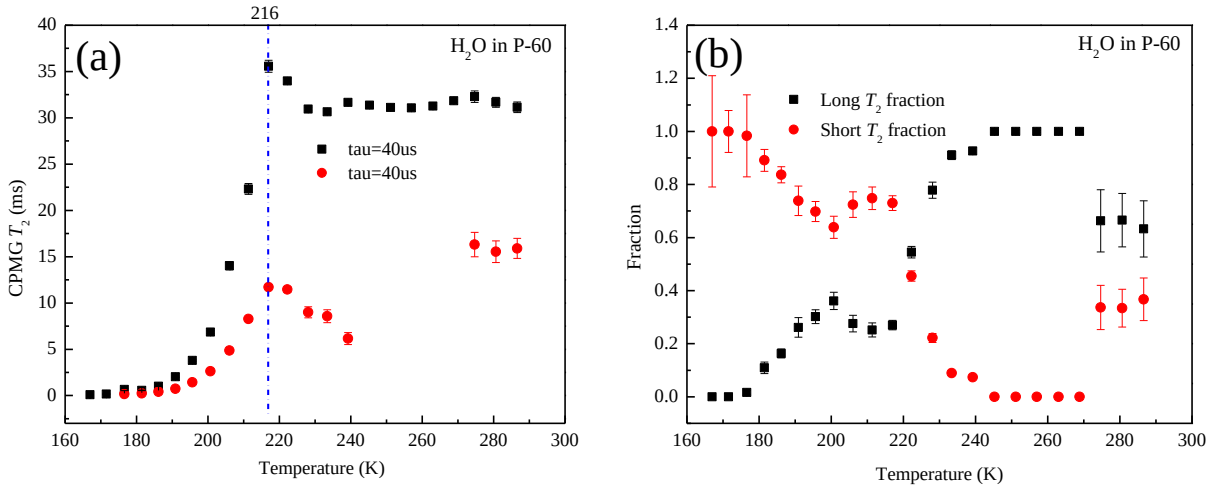

Figure A.4 (a) CPMG T_2 relaxation time for water in P-60 AC versus temperatures. (b) Fraction of long component and short component T_2 for water in P-60 AC versus temperatures.

In the middle temperature range, we also observed two components in CPMG measurement with echo space 80 μs. The fraction of T_2 long and short components are plotted in Figure A.4 (b). It is clear to see there has a conversion from these two components.

A3. NMR Results Analysis for water in P-40 AC

From NMR intensity analysis, the water confined in P-40 doesn't crystallize until below 170 K.

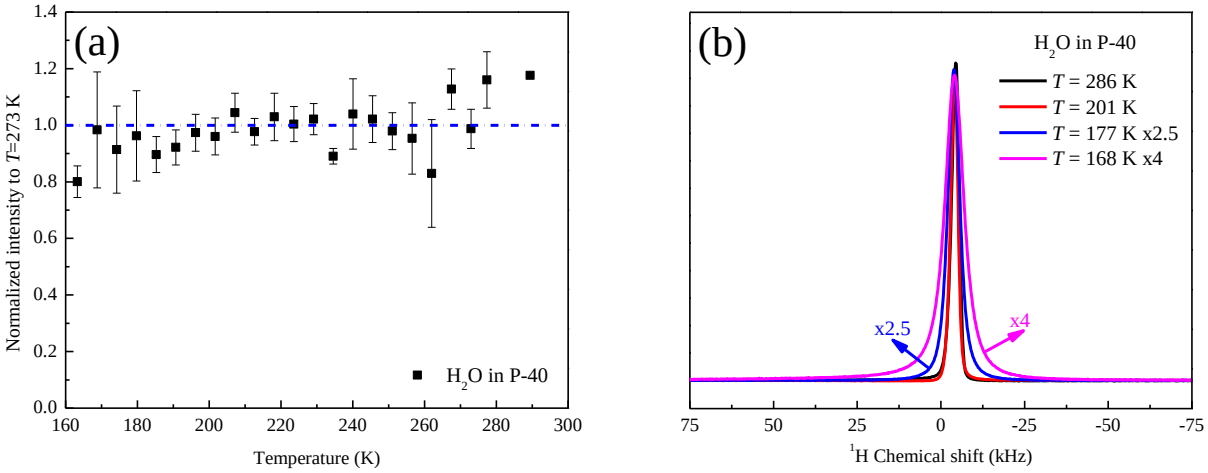

Figure A.5 (a) Normalized intensity of water in P-40 versus temperatures. (b) ^{1}H NMR spectra of water in P-40 at selected temperatures

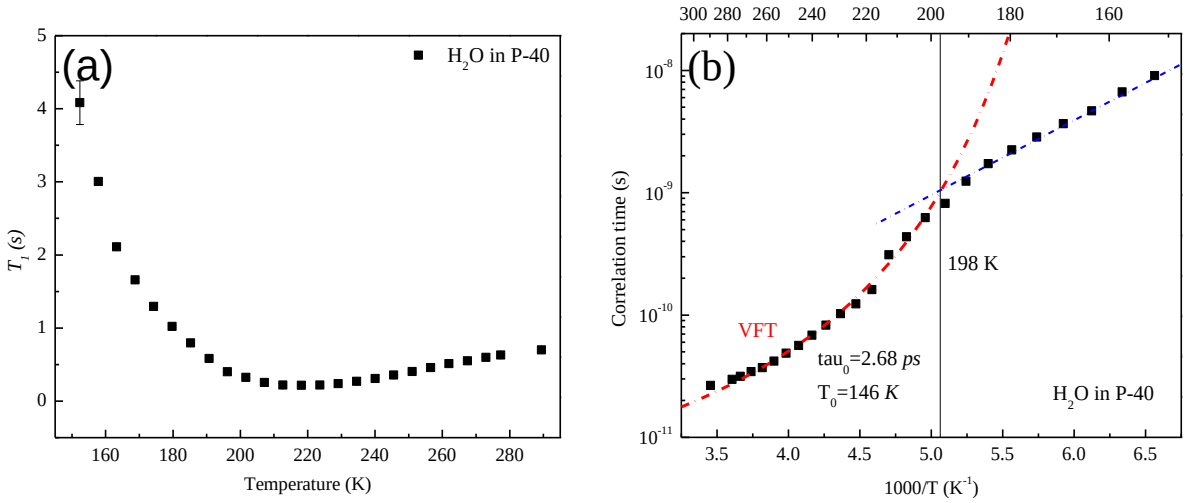

Figure A.6 (a) T_1 relaxation time for water in P-40 AC versus temperatures. (b) correlation time of water confined in P-40 versus temperature.

From NMR T_1 relaxation measurement and correlation time analysis, we found for water confined in P-40, there exists a VFT to Arrhenius transition at 198 K which the confined water still in liquid state.

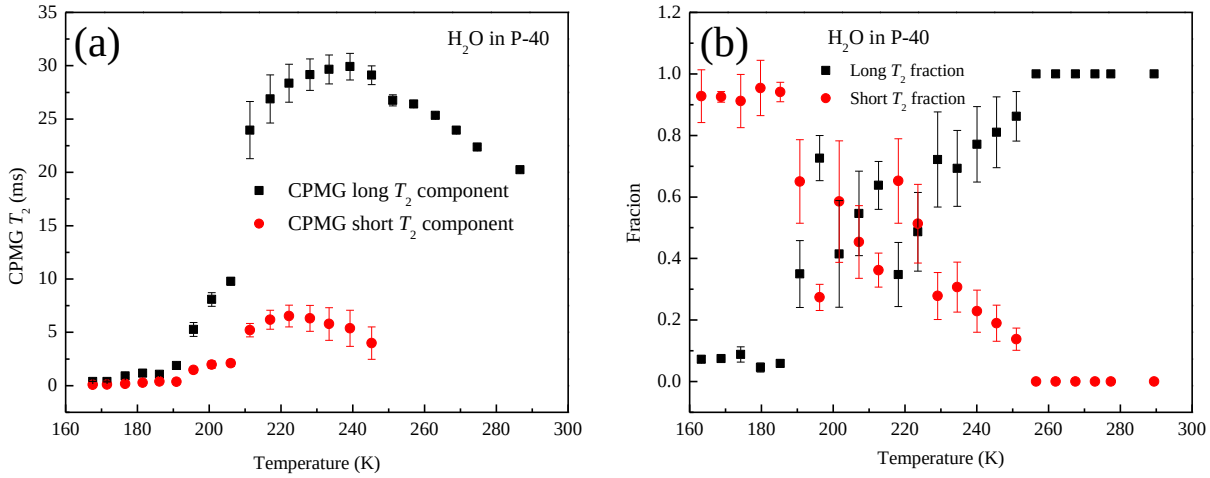

Figure A.7 (a) CPMG T_2 relaxation time for water in P-40 AC versus temperatures. (b) Fraction of long component T_2 and short component T_2 for water in P-40 AC versus temperatures.

In the middle temperature range, there are two components in CPMG measurement with echo space 80 μs. The fraction of long and short T_2 component is plotted in **Figure A3.3 (b)**. The conversion from these two components are not as clear as water in the larger pores.

A4. Plot of dynamic crossover temperature Versus pore sizes

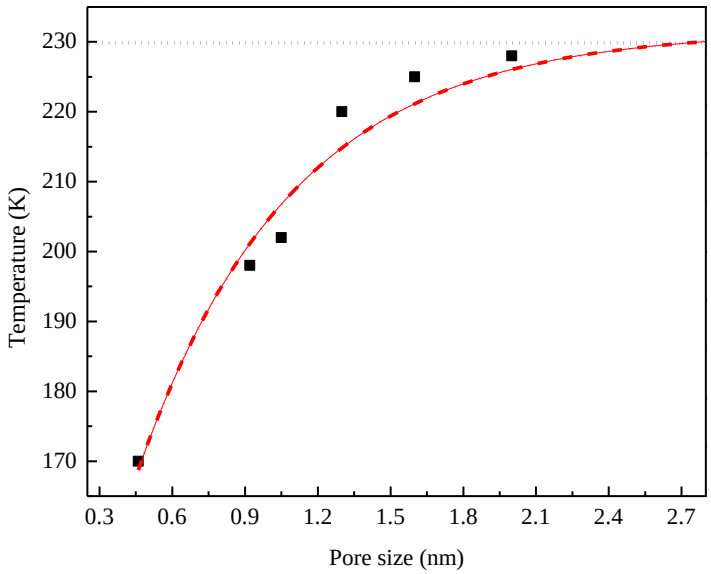

Figure A.8 Dynamic crossover temperature versus pore sizes.

In this thesis, we are studying the dynamic crossover for water confined in nanopores. The dynamic change for confined water all happened in liquid state so it is not induced by crystallization. For water confined in smaller pores, the dynamic crossover temperature is lower. For water confined in pore size equal or larger than 1.3 nm pores, the dynamic crossover temperature almost the same at around 225 K. That means, this temperature is independent with the pore sizes, but the intrinsic property of bulk water.

APPENDIX B

B1. T_1 NMR Measurements and Analysis for Bulk Water

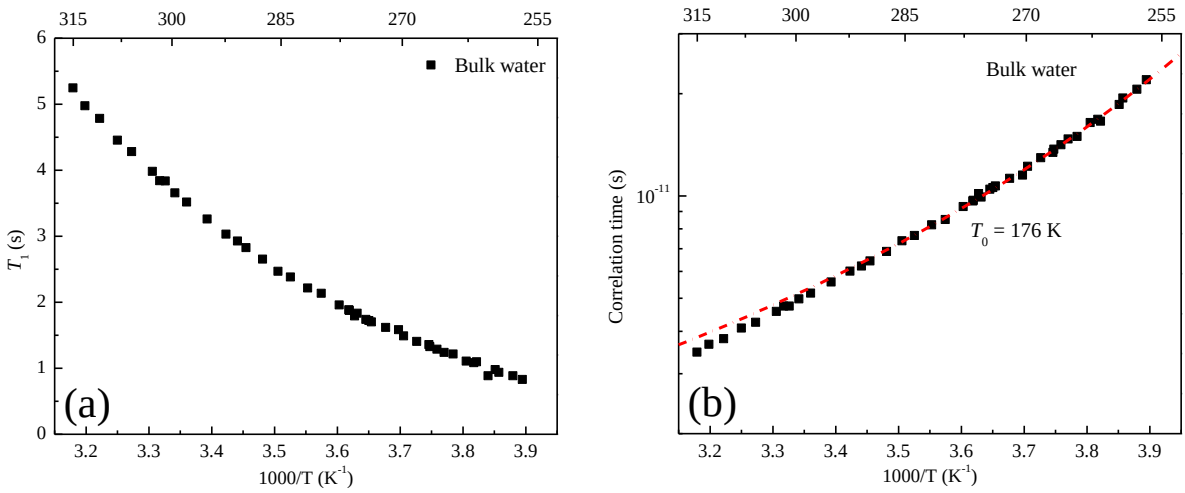

Figure B.1 (a) Experimental T_1 value for bulk water measured. (b) Correlation time calculated from experimental T_1 of water versus 1000/T. The red dashed line is the best fitting from VFT with fitting parameter $T_0 = 176$ K

Note: 176 K will be set in the fitting parameter for water in P-90/94 as reference

Krynicki, Hindman and Wood did the T_1 relaxation experiment for bulk water in a wide temperature before its crystallization several decades ago [133, 134]. **Figure B.1 (a)** is the original data from Hindman paper and **Figure B1.1 (b)** is the correlation time calculated from BPP equation (**Eq. (2.8)**). We selected the data in temperature range 295-270 K and fitted with VFT equation. The $T_0 = 176$ K is obtained from the best fit in the program and used as a reference for fitting the data in Chapter 3. In VFT equation, T_0 is the ideal glass transition temperature for a glass-form supercooled liquid. The possible rotational glass transition temperature from our measurements in **CHAPTER 4** is around 195 K which is not very far away 176 K.

B2. Intensity correction and uncertainty calculation

The intensity obtained from single pulse experiment is corrected by Currie's Law and extrapolate the signal to $t = 0$.

In **Eq. (2.2)**, doing the high temperature approximation, $\hbar\omega \ll k_B T$, it could be simplified to $M_0 \propto \frac{N\gamma^2\hbar^2 B_0 I(I+1)}{3k_B T} = \frac{N\gamma^2\hbar^2 B_0}{4k_B T} \propto \frac{1}{T}$. It means, for the same number spins under detection, at lower temperature will have larger intensity. So, the intensity measured in a large temperature range should be corrected by inverse of temperature before comparison.

Another correction is from electronic correction, the electronic circuit in the probe for example, resistors, capacitors are a function of temperature. The *Q* factor is different when it is at high temperature and low temperature which also will affect the detected intensity. In general, the detected intensity $M_0 \propto \sqrt{\frac{1}{Q}}$. Roughly speaking, we estimate the *Q* factor by measuring 3dB value from spectrometer.

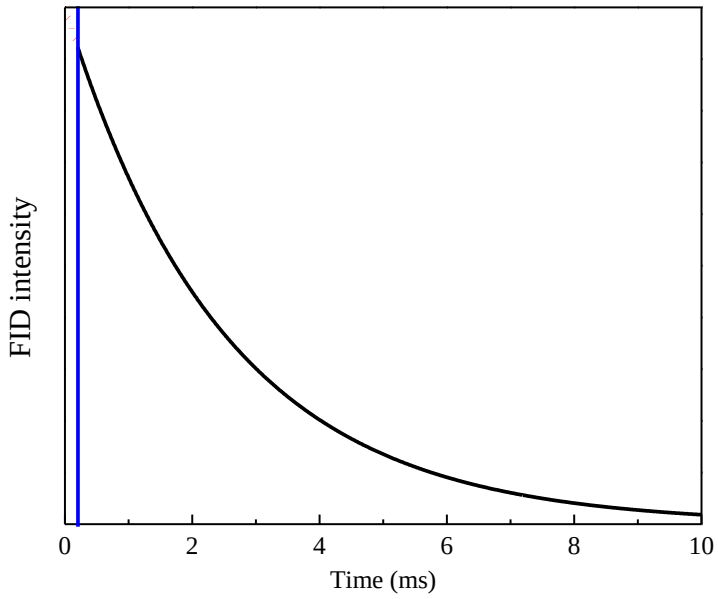

Figure B.2 Illustration of FID signal from single pulse NMR experiment. The black line is the example of typical FID signal, the red dot line is the signal missing during ring down delay and acquisition delay.

Figure B.2 shows a typical FID signal, the time for receiver to collect the signal is not at $t = 0$ but after ring down delay (rd) and acquisition delay (ad) manually set in the software. The rd and ad usually "dead time" are set for reducing the artificial noise when the RF pulse taken off. The decay rate of the FID is T_2^* which is the inverse of full width of half maximum of the Lorentzian spectrum (see Figure B.3).

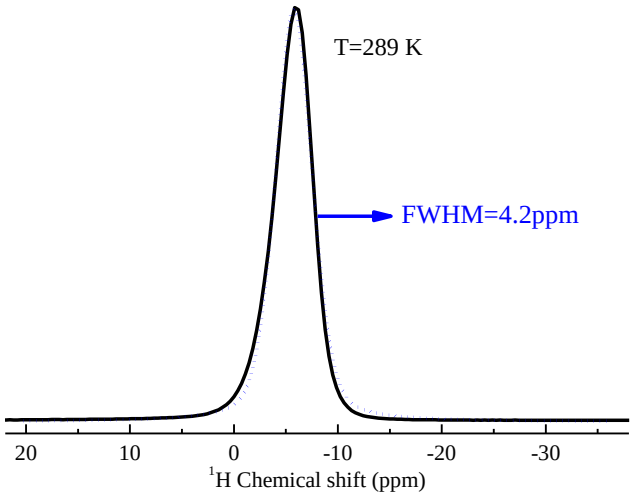

Figure B.3 ^{1}H NMR spectrum for water in P-90 at T = 289 K and fitted spectrum in Lorentzian shape

In our experiment, the total dead time = rd+ad+1/2 RF pulse length + dwell time=6.2μs

The T_2^* is calculated by Eq. (B.1)

$$T_2^* = \frac{1}{\pi \times FWHM} \qquad (B.1)$$

The corrected FID intensity should be

$$M(t=0) = M(t=6.2\ \mu s) \times \exp(6.2\mu s / T_2^*) \qquad (B.2)$$

For example, to correct the intensity of water in P-90 at T = 289 K, the fitted FWHM is 4.2 ppm for 500. 007 MHz magnet. The $T_2^* = \frac{1}{3.14 \times 4.2\ ppm \times 500.007\ MHz} = 0.0015\ s = 150\ \mu s$

Calculate each T_2^* from FWHM by fitting the spectra at different temperatures. At low temperatures, the FWHM of spectra are broader than 4.2 ppm which means most signal has been lost before the receiver collecting data. So, it is very necessary to extrapolate the FID signal to $t = 0$ and obtain the original intensity.

To estimate the uncertainty of the extrapolated intensity, we applied uncertainty propagation equation:

$$\frac{\delta M(t=0)}{M(t=0)} = \frac{\partial M(t=0)}{\partial T_2^*} \times \delta T_2^* = M(t=0) \times \frac{6.2\mu s}{(T_2^*)^2} \times \delta T_2^* \qquad (B.3)$$

Where $\delta M(t=0)$ is the uncertainty of extrapolated magnetization at $t=0$, δT_2^* is the standard error from fitting the spectrum.

B3. Temperature Calibration Process

When performing a variable temperature (VT) NMR experiment, the displayed temperature is not necessary the actual sample temperature. In our experiments, we need to know the actual temperature, with a high degree of accuracy, it is important to calibrate the sample temperature, relative to the displayed temperature.

We run the experiment from room temperature to -122℃ shown in VT panel. The proper method to do the temperature calibration is to observe the chemical-shift separation between the OH resonances and CH_3 resonances in 100% methanol [135]. The temperature dependence of this chemical shift is well-studied and is proper to calibration from 180-330 K.

The equation to calculate the actual temperature by chemical shift is:

$$T = -23.832\delta^2 - 29.46\delta + 403.0 \qquad (B.4)$$

Where δ is the chemical shift between OH group and CH_3 group.

Table (B.1) is the list for our temperature calibration experiment with the actual temperature calculated from Eq. (B.4) and the displayed temperature. Below 180 K, methanol cannot be further supercooled. The direct chemical shift will end on 180 K. For the temperature calibration below 180 K, we applied Eq. (B.6) to get the "actual" temperature.

Table B.1 List of experiment parameter and actual temperature calculated from Eq. (B.4)

T (℃)	δ_{CH_3}(ppm)	δ_{OH}(ppm)	δ(ppm)	**Actual T**	T (K)	ΔT (K)
15	0.8181	-0.8586	1.6767	**286.6049709**	288.15	1.545029114
10	0.8806	-0.8498	1.7304	**280.6626359**	283.15	2.487364101
5	0.9353	-0.8478	1.7831	**274.6973262**	278.15	3.452673778

0	0.9836	-0.8499	1.8335	**268.8685253**	273.15	4.281474662
-5	1.0319	-0.8514	1.8833	**262.9901942**	268.15	5.159805786
-10	1.0825	-0.8507	1.9332	**256.9814943**	263.15	6.168505704
-15	1.1296	-0.8509	1.9805	**251.1763039**	258.15	6.973696118
-20	1.1791	-0.8489	2.028	**245.2392517**	253.15	7.910748288
-25	1.2327	-0.8424	2.0751	**239.2460085**	248.15	8.903991518
-30	1.2901	-0.8303	2.1204	**233.3820523**	243.15	9.767947685
-35	1.3214	-0.8395	2.1609	**228.0566287**	238.15	10.09337132
-40	1.3635	-0.8408	2.2043	**222.2630999**	233.15	10.88690009
-45	1.4033	-0.8401	2.2434	**216.9667083**	228.15	11.18329172
-50	1.4472	-0.837	2.2842	**211.3623483**	223.15	11.78765166
-55	1.4948	-0.8277	2.3225	**206.0291931**	218.15	12.12080695
-60	1.5382	-0.8219	2.3601	**200.7254979**	213.15	12.42450214
-65	1.5644	-0.8313	2.3957	**195.6418098**	208.15	12.50819017
-70	1.5956	-0.8328	2.4284	**190.9190158**	203.15	12.23098418
-75	1.6265	-0.8346	2.4611	**186.1452552**	198.15	12.00474482
-80	1.659	-0.8339	2.4929	**181.4540006**	193.15	11.69599937
-85	1.7021	-0.8234	2.5255	**176.5946932**	188.15	11.55530676
-90	1.7455	-0.8137	2.5592	**171.5181734**	183.15	11.63182658
-95	1.7673	-0.8178	2.5851	**167.5798464**	178.15	10.57015358
-100				**162.473305**	173.15	10.676695
-102				**160.579905**	171.15	10.570095
-104				**158.686505**	169.15	10.463495
-106				**156.793105**	167.15	10.356895
-108				**154.899705**	165.15	10.250295
-110				**153.006305**	163.15	10.143695
-112				**151.112905**	161.15	10.037095
-114				**149.219505**	159.15	9.930495
-116				**147.326105**	157.15	9.823895
-118				**145.432705**	155.15	9.717295
-120				**143.539305**	153.15	9.610695

Note: T (℃) is the displayed temperature in VT unit; $T(K)$ is the absolute temperature for the displayed temperatures ($T(K) = T(℃) + 273.15$); δ_{CH_3} is the absolute chemical shift for CH_3 group in 100% methanol; δ_{OH} is the absolute chemical shift for OH group in 100% methanol; δ is the chemical shift between CH_3 group and OH group in 100% methanol; Actual T is the calibrated temperature by calculating from Eq. (B.4); ΔT is the difference between actual temperature and displayed temperature.

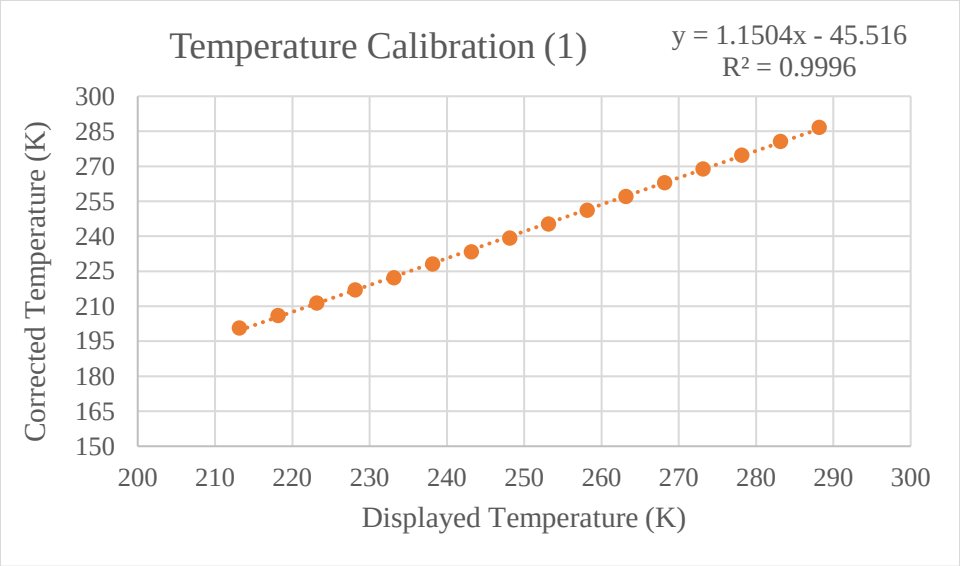

Figure B.4 Linear regression fitting for actual temperature and displayed temperature in temperature range 300 K-210 K. The linear equation from least square fitting is $y = 1.1504x - 45.516$ with $R^2 = 0.9996$

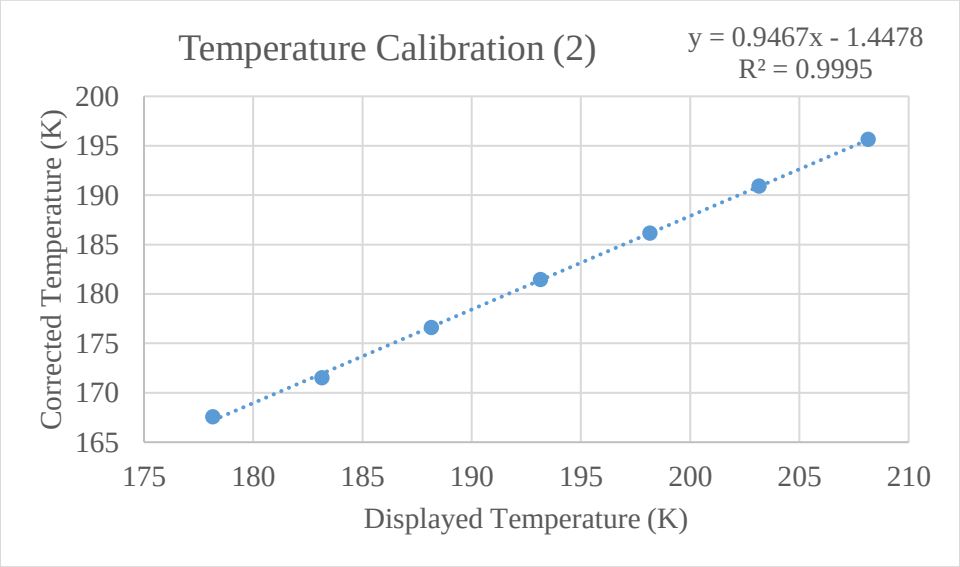

Figure B.5 Linear regression fitting for actual temperature and displayed temperature in temperature range 210 K-180 K. The linear equation from least square fitting is $y = 0.9467x - 1.4478$ with $R^2 = 0.9995$

As shown in **Figure B.4** and **Figure B.5**, the linear regression equations for actual temperature and displayed temperature are different in high temperature range and low temperature range.

From our fitting result, in high temperature range, the linear regression equation to describe actual temperature and displayed temperature is:

$$Actual\ T = 1.1504 \times (displayed\ T) - 45.516 \qquad (B.5)$$

And in low temperature range, the linear regression equation to describe the actual temperature and displayed temperature is:

$$Actual\ T = 0.9467 \times (displayed\ T) - 1.4478 \qquad (B.6)$$

Since we are lack of data for temperature calibration below 180 K, so, we applied Eq. (B.6) to calculate the actual temperature by the displayed temperature.

APPENDIX C

C1. Separation Spin-Lattice Relaxation Process

The T_1 relaxation mechanism for water is contributed by dipolar interaction and spin-rotation.

The experiment measured T_1 is in terms of T_{1d} and T_{1sr}, where T_{1d} is the dipolar interaction contributed part and T_{1sr} is spin-rotation contributed part.

$$1/T_{1,exp} = 1/T_{1d} + 1/T_{1sr} \qquad (C.1)$$

To estimation the contribution from proton-proton dipolar interaction and water molecule spin-rotation, we introduce the correlation time τ_d which describe the water molecule re-oriented rate and τ_{sr} which is the angular velocity for water molecules. Hence,

$$T_{1d} \propto \tau_d^{-1} \qquad (C.2)$$

For a linear molecule, the spin-rotation contribution to the relaxation is given by [95]:

$$T_{1sr} = 3/4\ I_0^{-1} k_B^{-1} \hbar^2 c^{-2} \tau_{sr}^{-1} \qquad (C.3)$$

Where I_0 is the momentum of inertia, c is the spin-rotation interaction constant and τ_{sr} is the correlation time for angular velocity of the water molecule. k_B is the Boltzmann constant, $\hbar$ is the Plank constant.

It has been shown that for spherical molecules and in certain circumstances, τ_d and τ_{sr} are related by [95]:

$$\tau_d \tau_{sr} = I_0/6k_B T \qquad (C.4)$$

If we assume the water molecule is similar to hard spherical molecule, we can apply Eq. (C.4) to estimate τ_d and τ_{sr} from experimental results. Powles and Smith did that in 1966, they found for bulk water at room temperature, τ_{sr} is in $10^{-15} s^{-1}$ scale (femtosecond), while τ_d is in picosecond, so, $\tau_{sr} \ll \tau_d$. Then the contribution from spin-rotation in liquid bulk water could be

negligible. The dipolar interaction will dominate the T_1 relaxation process. For bulk liquid, the dipolar interaction from two parts: intermolecular homonuclear dipolar interaction and intramolecular homonuclear dipolar interaction. To rewrite the Eq. (C.1) into:

$$1/T_{1,exp} = 1/T_{1,intra} + 1/T_{1,inter} \qquad (C.5)$$

To separate the inter and intra proton-proton dipolar interaction contribution to T_1, we introduce heavy water and pure water mixture system [136].

In such mixture there are three species, H_2O, D_2O and HDO in dynamic equilibrium:

$$H_2O + D_2O \rightleftharpoons 2HDO \qquad (C.6)$$

The D_2O will have fast exchange with H_2O and extra D_2O could be surround H_2O, so the intramolecular proton-proton interaction could be replaced by proton-deuterium interaction, and the same as intermolecular dipolar interaction. When the D2O introduced to bulk water system, it could reduce the proton-proton dipolar interaction due to D has much smaller γ_D comparing to γ_H. So the inter and intra proton-proton dipolar interaction is related to the number of proton in the system (mole fraction x). The total inter-contribution to the dipolar relaxation in the solution is expressed:

$$1/T_{1,inter} = x \cdot 1/T_{1(inter\ H\ with\ H)} + (1-x) \cdot 1/T_{1(inter\ H\ with\ D)} \qquad (C.7)$$

The intra-dipolar relaxation is from H-H and H-D from the same molecule. So that

$$1/T_{1,intra} = 1/T_{1,intra\ H_2O} + 1/T_{1,intra\ HDO} \qquad (C.8)$$

Since from dipolar interaction calculation

$$\frac{T_{1,H\ in\ D_2O}}{T_{1,inter\ H_2O}} = \frac{T_{1,intra\ HDO}}{T_{1,intra\ H_2O}} = \frac{\frac{3}{2}(\gamma_H/\gamma_D)^2 I_H(I_H+1)}{I_D(I_D+1)} = 24 \qquad (C.9)$$

To simplify the Eq. (C.1) and Eq. (C.5), we can extrapolate the $T_{1,inter\ H_2O}$ and $T_{1,intra\ H_2O}$ by varying the mole fraction of pure water in the mixed sample and fit the experimental T_1 in:

$$\frac{1}{T_{1,exp}} = \left(\frac{23}{24}x + \frac{1}{24}\right)\frac{1}{T_{1,inter}} + \frac{1}{T_{1,intra}} \qquad (C.10)$$

This equation is more commonly written in terms of mole fraction α of D_2O in mixed water [137]:

$$1/T_{1,exp} = 1/T_{1,intra} + \left(1 - \frac{23}{24}\alpha\right)\frac{1}{T_{1,inter}} \qquad (C.11)$$

If we plot the experimental $1/T_1$ versus $(1 - \frac{23}{24}\alpha)$, for different molar ratio D_2O, there is a straight line, the intercept is $1/T_{1,intra}$, and the slope is $1/T_{1,inter}$.

The ratio of translational and rotational motion for bulk water can be estimated [92]:

$$\frac{1/T_{1,translation}}{1/T_{1,rotationa}} = \frac{3\pi N b^6}{5a^3} = 0.24 \qquad (C.12)$$

Where N is number of spins in 1 cm^3, for water two spins system, $N = 2\times\frac{6.02}{18}\times 10^{23}\ per\ cm^3$, b is internuclear distance (intramolecular distance), for water $b = 1.56$ Å, a is molecular radius, $a = 1.957$ Å for water.

In our experiment, the purpose to use mixed sample confined in P-90 is to separate the $T_{1,inter}$ and $T_{1,intra}$ in nanoconfinement system. We mixed D_2O in pure water sample with different molar ratio, α = 0, 0.2, 0.4, 0.6, and 0.8. We measured T_1 for the set of samples by applying inversion-recovery pulse sequence. In whole temperature range, T_1 decay follows single exponential decay for all the samples.

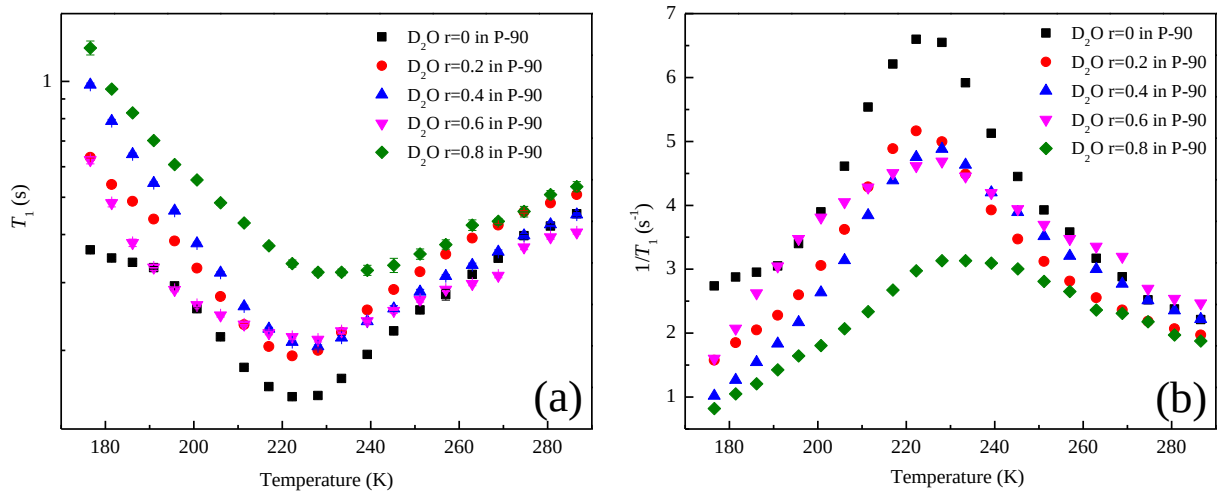

Figure C.1 (a) T_1 spin-lattice relaxation time for different water sample confined in P-90 activated carbon versus temperatures. (b) Inverse of T_1 for different samples versus temperatures.

In **Figure C.1**, it is clearly to see that T_1 doesn't have distinguish increase by adding more D_2O from room temperature to 250 K. Below 250 K, there has a clear separate T_1 for different molar ratio of D_2O, at lower temperature, such separation is more obvious. Overall, comparing the absolute T_1 experimental values for pure water in P-90 and D_2O80%-H_2O in P-90, in the whole temperature range, the T_1 for mixed water in P-90 is longer than that for pure water in P-90. This is due to adding D_2O into the water could reduce the inter and intra molecular dipolar interaction.

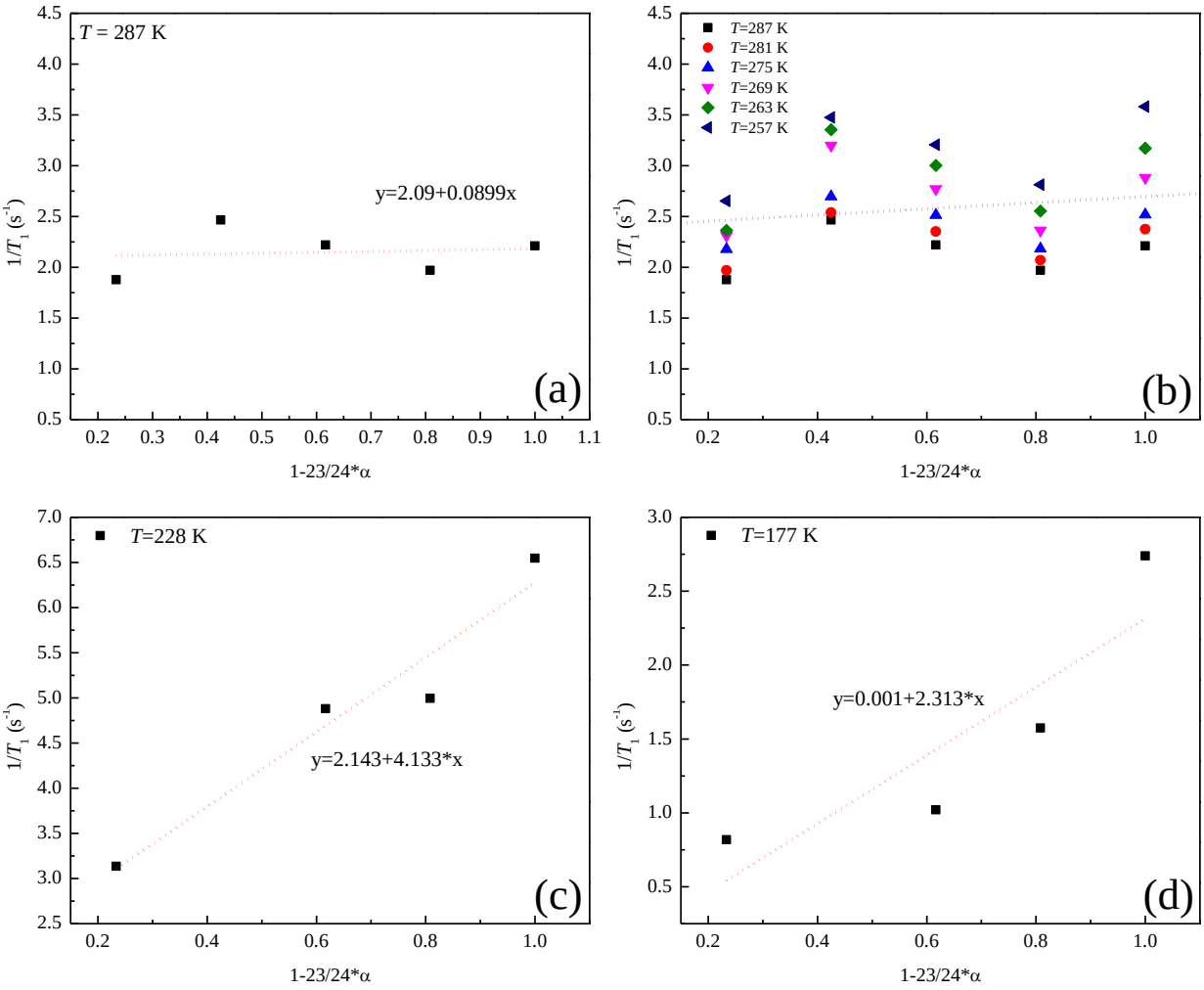

Figure C.2 (a) $1/T_1$ experimental data plot for different α value at T = 287 K. the red dot line is least-square linear regression fitting result. (b) $1/T_1$ experimental data at different temperatures versus different α values. Black dot line is the sketched straight line for reading data. (c) $1/T_1$ experimental data versus different α for water confined in P-90 at T = 228 K. Red dot line is the linear regression fitting for the data. (d) $1/T_1$ experimental data versus different α for water confined in P-90 at T = 177 K. Red dot line is the linear regression fitting for the data.

In **Figure C.2**, we gave the example to apply **Eq. (C.11)** to the experimental data. In this data analysis process, it is important to emphasis we ignored the spin-rotation contribution for water at low temperature, we assume, as sufficient low temperature the τ_{sr} keeps the same as it is at high temperature in femtosecond scale, the most relaxation contribution for T_1 is still from dipolar interaction. So, from the data analysis in **Figure C.2 (a)** and **(b)** the less distinguishable

separation T_1 at 300-260 K shows if we plot the T_1 in terms of r in **Eq. (C.11)**, the slope is close to zero and the intercept is equal to $1/T_1$. This indicates, for the confinement system, the $1/T_{1,inter}$ part is negligible to be accounted into the contribution to T_1 relaxation process. The T_1 relaxation mechanism in confinement system above 260 K is due to the intramolecular dipolar interaction.

Below 260 K, it is more obvious to see the difference of T_1 for different molar ratio D_2O mixed in the water. If we plot the data and fit with **Eq. (C.11)**, it gives a reasonable linear relationship as shown in **Figure (C.3) (c)**. If the T_1 relaxation process is still dominated from dipolar interaction, the inter-molecular dipolar interaction becomes important when it goes to lower temperature. When at 177 K, it is not a linear curve but increases drastically.

Table C.1 and **Figure C.4** is the summary for the linear fitting of all the listed data.

Table C.1 Analysis summary for T_{1intra} and T_{1inter} from experimental data and **Eq. (C.11)**

Temp (K)	$\mathbf{1/T_{1exp}}$	$\mathbf{1/T_{1intra}}$	$\mathbf{1/T_{1inter}}$	$\boldsymbol{T_{1exp}}$	$\boldsymbol{T_{1intra}}$	$\boldsymbol{T_{1inter}}$	$\boldsymbol{R^2}$
287	2.21029	2.093	0.0899	0.45243	0.47778	11.12347	0.01
281	2.37552	2.151	0.1788	0.42096	0.4649	5.59284	0.04
275	2.51864	2.364	0.0878	0.39704	0.42301	11.38952	0.01
269	2.8811	2.606	0.156	0.34709	0.38373	6.41026	0.02
263	3.17168	2.626	0.425	0.31529	0.38081	2.35294	0.09
257	3.58218	2.761	0.624	0.27916	0.36219	1.60256	0.25
251	3.92711	2.54	1.2	0.25464	0.3937	0.83333	0.488
245	4.44978	2.65	158	0.22473	0.37736	0.00633	0.567
239	5.12531	2.54	2.32	0.19511	0.3937	0.43103	0.74
233	5.91786	2.36	3.28	0.16898	0.42373	0.30488	0.839
228	6.54707	2.143	4.132	0.15274	0.46664	0.24201	0.911
222	6.59718	1.887	4.49	0.15158	0.52994	0.22272	0.958
217	6.21118	1.599	4.426	0.161	0.62539	0.22594	0.97
211	5.5371	1.348	3.991	0.1806	0.74184	0.25056	0.9641
206	4.60957	1.243	3.18	0.21694	0.80451	0.31447	0.962
201	3.89848	1.105	2.623	0.25651	0.90498	0.38124	0.952

196	3.40078	1.004	2.181	0.29405	0.99602	0.45851	0.887
191	3.04971	0.808	2.016	0.3279	1.23762	0.49603	0.8518
186	2.9543	0.510	2.15	0.33849	1.96078	0.46512	0.785
181	2.87853	0.2742	2.238	0.3474	3.64697	0.44683	0.701
177	2.73943	0.001	2.313	0.36504	1000	0.43234	0.656

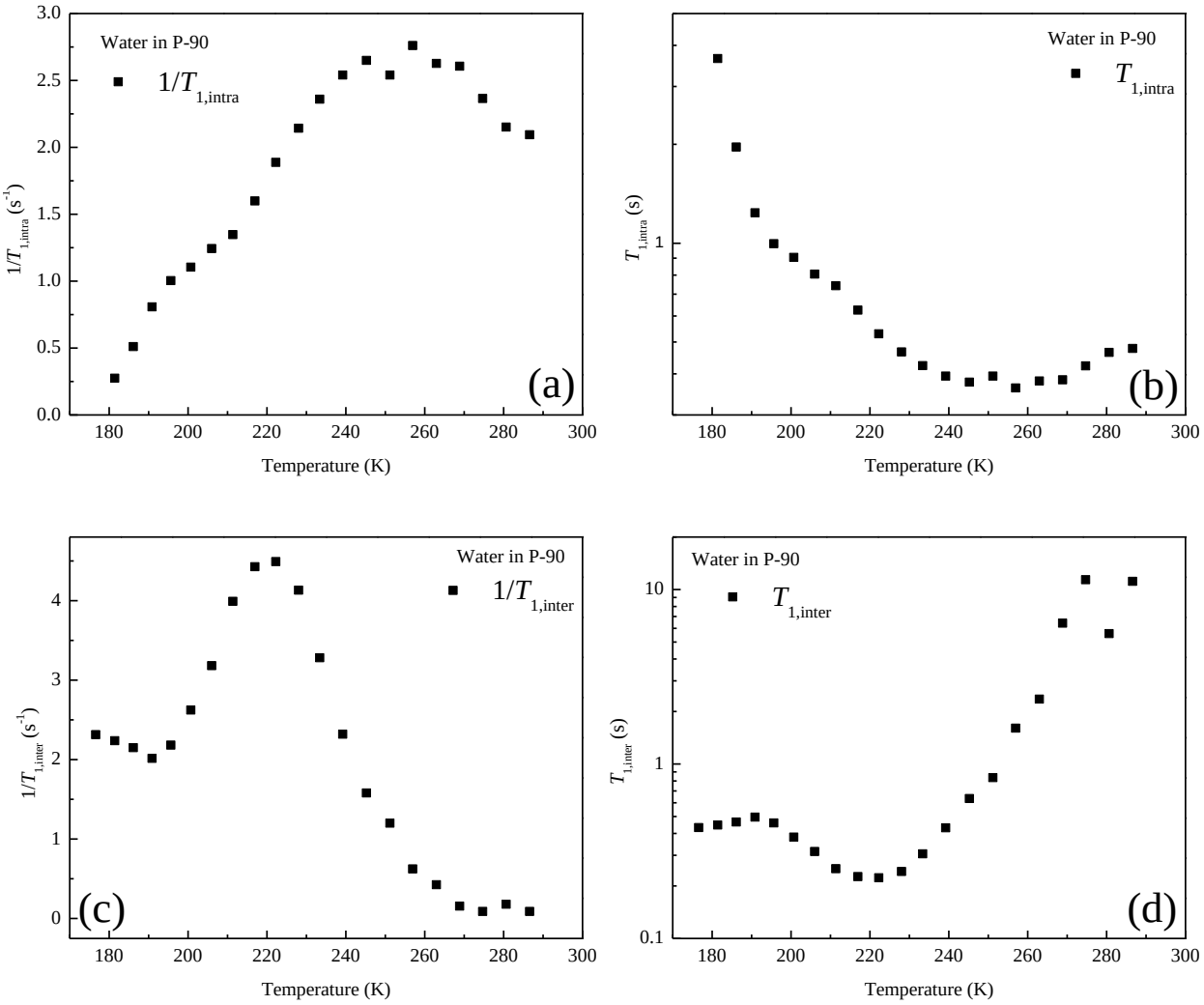

Figure C.3 (a) $1/T_{1,intra}$ from **Table C.1** versus temperatures. (b) $T_{1,intra}$ versus temperatures. (c)1/ $T_{1,inter}$ from **Table C.1** versus temperatures. (d) $T_{1,inter}$ versus temperatures

By comparing **Figure C.3 (a)** and **(c)**, at high temperature range, from room temperature to 260 K, the inter part doesn't play an important role, while at low temperatures, the inter part plays a much important role in T_1 relaxation mechanism which is very questionable.

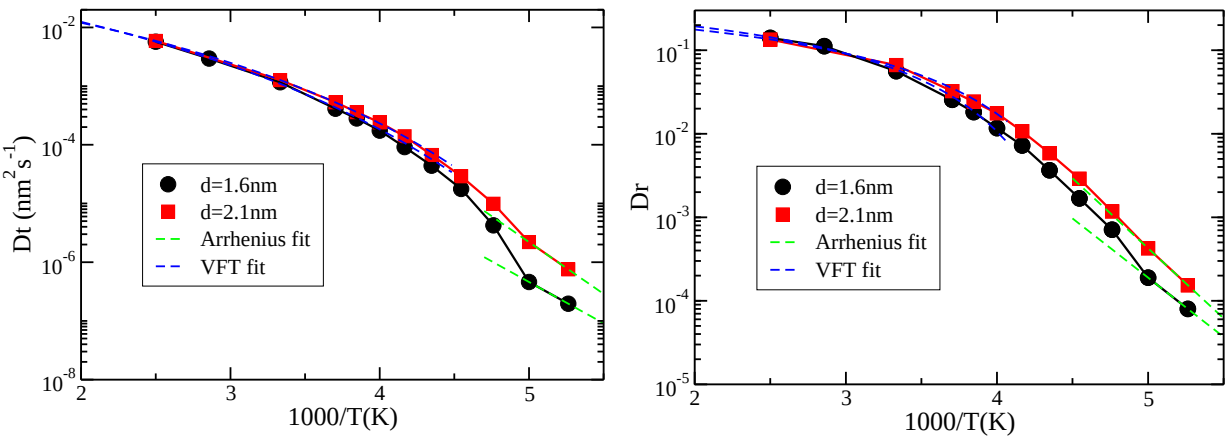

Figure C.4 (a) Translational diffusion coefficient for water confined in 1.6 nm hydrophilic pores and 2.1 nm hydrophilic pores. (b) Rotational diffusion coefficient for water confined in 1.6 nm hydrophilic pores and 2.1 nm hydrophilic pores. Green dash line is Arrhenius equation fit for the diffusion coefficient at low temperatures. Blue dash line is VFT equation fit for diffusion coefficient at high temperature region.

From our collaborate simulation results (see **Figure C.4**), it shows both rotational diffusion coefficient and translational diffusion coefficient will slow down quickly in the supercooled region. The VFT and Arrhenius fitting shows, at high temperature, the diffusion coefficients follow VFT equation, while going to low temperature, especially below 250 K, the diffusion coefficients follow Arrhenius equation. If we lot the ratio of rotational and translational coefficient versus temperature for confined water, **Figure C.4** shows at 350 K, the rotational and translational diffusion coefficient is comparable, both intra and inter are important, however, by decreasing the temperature, the ratio of rotational and translational diffusion coefficient is getting larger, at 210 K, the ratio reaches 100, and below 210 K, it ratio drastically increases to 400 for water confined in 1.6 nm hydrophobic pores. This result means, comparing to intramolecular interaction, at low temperature, the intermolecular interaction is much less important.

This conclusion is also proved by the neutron scattering and NMR diffusion experiments for confined water (See **Figure 1.13** in **CHAPTER 1**). By decreasing the temperature, the

diffusion coefficient for confined water dropped, and the translational correlation time increases fast.

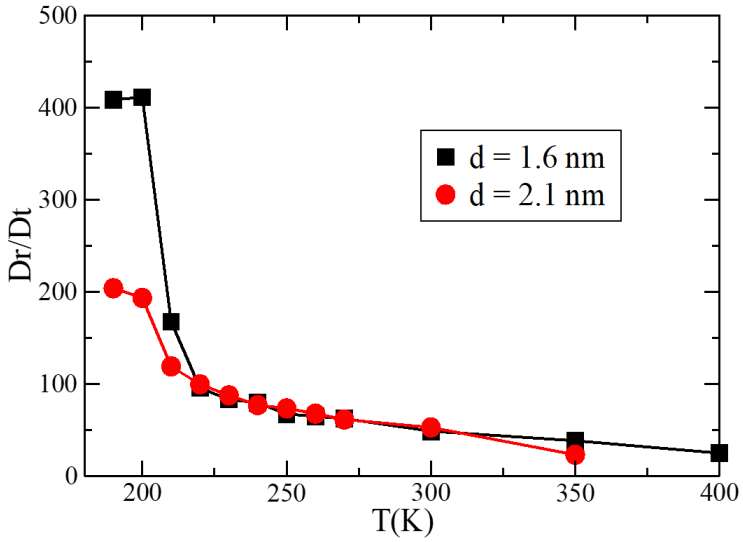

Figure C.5 Ratio of rotational and translational coefficient for confined water versus temperatures.

So, from simulation and direct experimental evidence, for the confined water, intermolecular dipolar interaction is negligible for T_1 relaxation process. Also from our data fitting and fitting weight R^2 (see **Figure C.6**), only at 240-190 K, the experimental data follows **Eq. (C.11)**. There is other mechanism should be introduced into the relaxation process in the supercooled region. In section 1 discuss, since we consider water has fast spin-rotation, which is negligible in the **Eq. (C.5)** for bulk water. This assumption is questionable when water in the supercooled region. If the spin-rotation rate is comparable to the intra-molecular rotation, the T_1 relaxation mechanism for confined water is a combination of intra-dipolar interaction and spin-rotation. Further discussion will be done in the future.

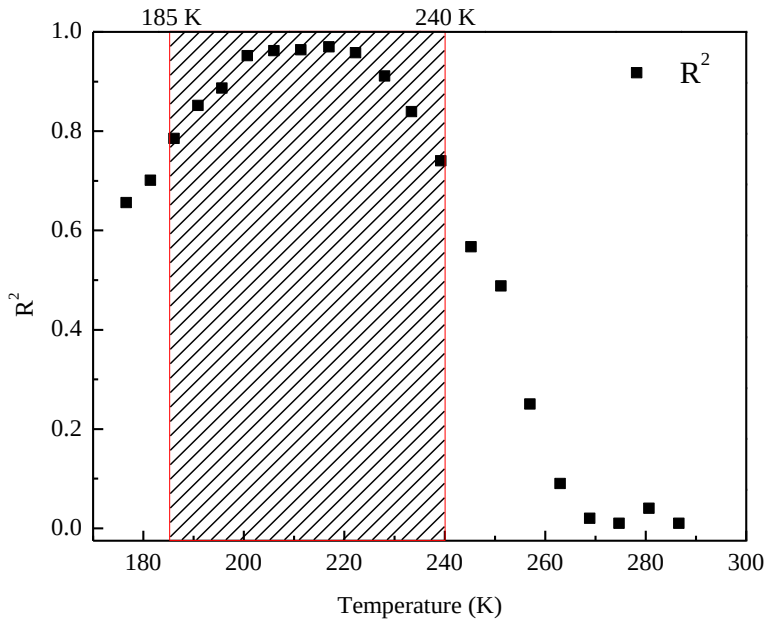

Figure C.6 Least-square linear regression fitting weight R^2 versus temperatures.

C2. Line Broadening Discussion

In **CHAPTER 4**, we discussed the broad peak from bottom at low temperature which is the sign of amorphous ice. The line broadening of the bottom peak is due to the strong intermolecular dipolar interaction. In this part, we show the details to discuss the dipolar interaction line broadening.

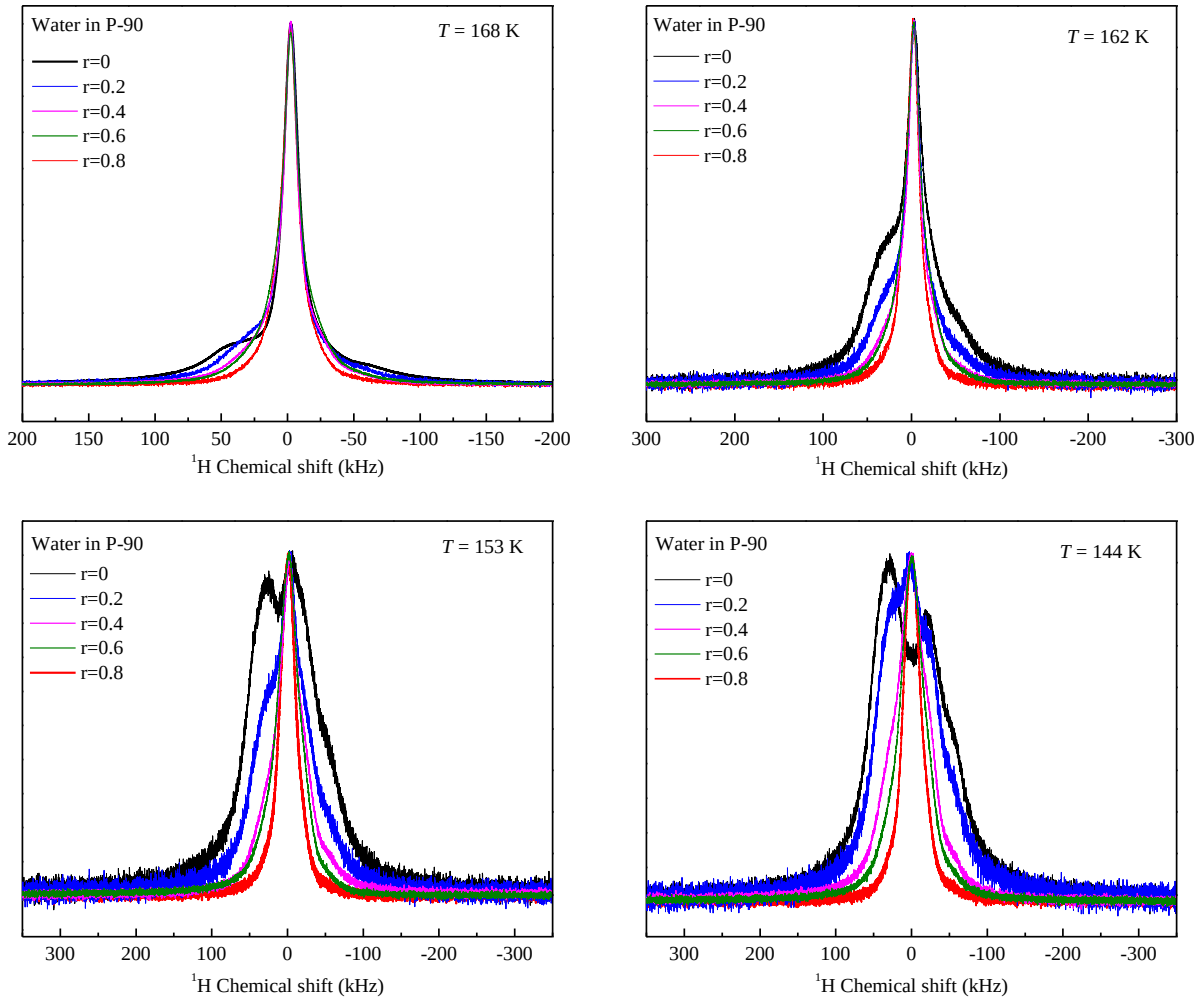

Figure C.7 (a)-(d) ^{1}H spectra for r=0/0.2/0.4/0.6/0.8 molar ratio of D_2O in water confined in P-90 at selected temperature

REFERENCE

1. Linstrom, P.J. and W.G.e. Mallard, *Water.* NIST Chemistry WebBook, NIST Standard Reference Database Number 69, 2016.

2. Ball, P., *Water-an enduring mystery.* Nature, 2008. **452**: p. 291-292.

3. Landau, L.D. and E.M. Lifshitz, *Statistical Physics 3rd Edition.* Institute of Physical Problems, USSR Academy of Sciences, Moscow, 1980. **5**.

4. Franks, F., *Introduction-water, the unique chemical.* Water A comprehensive treaties, 1972. **Vol. 1**(Plenum Press): p. 1-20.

5. Angell, C., J. Shuppert, and J. Tucker, *Anomalous properties of supercooled water. Heat capacity, expansivity, and proton magnetic resonance chemical shift from 0 to-38%.* The Journal of Physical Chemistry, 1973. **77**(26): p. 3092-3099.

6. Speedy RJ and A. CA., *Isothermal compressibility of supercooled water and evidence for a thermodynamic singularity at -45C.* The Journal of Chemical Physics, 1976. **65**: p. 851-858.

7. Mason, B.J., *The supercooling and nucleation of water.* Adv. Phys, 1958. **7**: p. 221-234.

8. Choukrouna, M. and O. Grasset, *Thermodynamic model for water and high-pressure ices up to 2.2 GPa and down to the metastable domain.* J. Chem. Phys., 2007. **127**(124506).

9. Debenedetti, P.G., *Supercooled and glassy water.* Journal of Physics: Condensed Matter, 2003. **15**(45): p. R1669.

10. Mishima, O. and H.E. Stanley, *Decompression-induced melting of ice IV and the liquid-liquid transition in water.* Nature, 1998. **392**: p. 164-168.

11. Burton, E.F. and W.F. Oliver, *The crystal structure of ice at low temperatures.* Proc. R. Soc. Lond A, 1936. **153**: p. 166-172.

12. Smith, R.S., C. Huang, and B.D. Kay, *Evidence for molecular translational diffusion during the crystallization of amorphous solid water.* J. Phys. Chem B, 1997. **101**: p. 6123-6126.

13. Johari, G.P. and M. Goldstein, *Viscous Liquids and the Glass Transition. II. Secondary Relaxations in Glasses of Rigid Molecules.* J Chem Phys, 1970. **53**(6): p. 2372.

14. Sellberg, J.A., et al., *Ultrafast X-ray probing of water structure below the homogeneous ice nucleation temperature.* Nature, 2014. **510**(7505): p. 381-4.

15. Mishima, O., L.D. Calvert, and E. Whalley, *Melting ice at 77K and 10kbar: a new method of making amorphous solids.* Nature, 1984. **310**: p. 393-395.

16. Heide, H.-G., *Observation on ice layers.* Ultramicroscopy, 1984. **14**: p. 271-278.

17. Mishima, O., L.D. Calvert, and E. Whalley, *An apparently first-order transition between two amorphous phases of ice induced by pressure.* Nature, 1985. **314**: p. 76-78.

18. Mishima, O., *Relationship between melting and amorphization of ice.* Nature, 1996. **384**: p. 546-549.

19. Hemley, R.J., L.C. Chen, and H.K. Mao, *New transformations between crystalline and amorphous ice.* Nature, 1989. **338**: p. 638-640.

20. Brazhkin, V.V., et al., *Elastic softening of amrphous H2O network prior to the hda-lda transition in amorphous state.* Rev. High Press. Sci. Technol, 1998. **7**: p. 1129-1131.

21. Bellissent-Funel, M.C. and L.A. Bosio, *A neutron scattering study of liquid D2O* J. Chem. Phys., 1995. **102**: p. 3727-3735.

22. Starr, F.W., M.C. Bellissent-Funel, and H.E. Stanley, *Structual evidence for the continuityof liquid and glassy water.* Cond. Matt. Phys, 1998.

23. Sharma, S.M. and S.K. Sikka, *Pressure induced amorphization of material.* Prog. Mater. Sci., 1996. **40**: p. 1-77.

24. Ponyatovsky, E.G. and O.I. Barkalov, *Pressure-induced amorphous phases.* Mater. Sci. Rep., 1992. **8**: p. 147-191.

25. Soper, A.K., *Structures of High-Density and Low-Density Water.* PHYS. REV. LETT., 2000. **84**(13).

26. Poole, P.H., et al., *Phase behaviour of metastable water.* Nature, 1992. **360**(6402): p. 324-328.

27. Sastry, S., et al., *Singularity-free interpretation of the thermodynamics of supercooled water.* Phys Rev. E, 1996. **53**(6).

28. Rebelo, L.P.N., P.G. Debenedetti, and S. Sastry, *Singularity-free interpretation of the thermodynamics of supercooled water.II. Thermal and volumetric behavior.* J. Chem. Phys., 1998. **109**(2).

29. Poole, P.H., et al., *The spinodal of liquid water.* Phys. Rev. E, 1993. **48**: p. 3799-3817.

30. Borick, S.S., P.G. Debenedetti, and S. Sastry, *A lattice model of network-forming fluids with orientation-dependent bonding: equilibrium. stability, and implications from the phase behavior of supercooled water.* J. Phys. Chem, 1995. **99**: p. 3781-3793.

31. Stanley, H.E. and J. Teixeira, *Interpretation of the unusual behavior of H2O and D2O at low temperatures: Tests of a percolation model.* J. Phys. Chem, 1980. **73**: p. 3404-3422.

32. Geiger, A. and H.E. Stanley, *Low-density patches in the hyrogen-bonded network of liquid water: Evidence from molecular dynamics computer simulation.* Phys. Rev. Lett., 1982. **49**: p. 1749-1752.

33. Tanaka, H., *Phase behaviors of supercooled water: Reconciling a critical point of amorphous ices with spinodal instability.* J. Chem. Phys., 1996. **105**: p. 5099-5111.

34. Mishima, O. and H.E. Stanley, *The relationship between liquid, supercooled and glassy water.* Nature, 1998. **396**: p. 329-335.

35. Harrington, S., et al., *Liquid-liquid phase transition: Evidence from simulations.* Phys. Rev. Lett., 1997. **78**: p. 2409-2412.

36. Sciortino, F., et al., *Line of compressibility maxima in the phase diagram of supercooled water.* Phys Rev E, 1997. **55**: p. 727-737.

37. Li, Y., J. Li, and F. Wang, *Liquid-liquid transition in supercooled water suggested by microsecond simulations.* Proc Natl Acad Sci U S A, 2013. **110**(30): p. 12209-12.

38. Rontgen, W.C., *Ueber die constitution des flussigen wassers.* Ann. Phys. Chem., 1892. **45**: p. 91-97.

39. Frank, H.S., *The Structure of Ordinary Water.* Science, 1970. **169**(635).

40. Holten, V. and M.A. Anisimov, *Entropy-driven liquid-liquid separation in supercooled water.* Sci Rep, 2012. **2**: p. 713.

41. Bertrand, C.E. and M.A. Anisimov, *Peculiar thermodynamics of the second critical point in supercooled water.* J Phys Chem B, 2011. **115**(48): p. 14099-111.

42. Fuentevilla, D.A. and M.A. Anisimov, *Scaled Equation of State for Supercooled Water near the Liquid-Liquid Critical Point.* Physical Review Letters, 2006. **97**(19).

43. Holten, V., et al., *Two-state thermodynamics of the ST2 model for supercooled water.* J Chem Phys, 2014. **140**(10): p. 104502.

44. Tanaka, H., et al., *General discussion.* Faraday Discuss., 2013. **167**: p. 109-143.

45. Limmer, D.T. and D. Chandler, *The putative liquid-liquid transition is a liquid-solid transition in atomistic models of water. II.* J Chem Phys, 2013. **138**(21): p. 214504.

46. Sadr-Lahijany, M.R., et al., *Liquid state anomalies for the Stell-Hemmer core-softened potential.* Phys. Rev. Lett., 1998. **81**: p. 4895-4898.

47. Robinson, G.W., et al., *Water in Biology, Chemistry and Physics: Experimental Overviews and Computational Methodologies.* World Scientific, Singapore, 1996.

48. Stillinger, F.H. and A. Rahman, *Improved simulation of liquid water by molecular dynamics.* The Jounal of Chemical Physics, 1974. **60**(4): p. 1545-1557.

49. Berendsen, H.J.C., J.R. Grigera, and T.P. Straatsma, *The missing term in effective pair potentials.* J. Phys. Chem., 1987. **91**: p. 6269-6271.

50. Horn, H.W., et al., *Development of an improved four-site water model for biomolecular simulations: TIP4P-Ew.* J. Chem. Phys., 2004. **120**: p. 9665-9678.

51. Mahoney, M.W. and W.L. Jorgensen, *A five-site model for liquid water and the reproduction of the density anomaly by rigid, nonpolarizable potential functions.* J. Chem. Phys., 2000. **112**: p. 8910-8922.

52. Akin-Ojo, O., Y. Song, and F. Wang, *Developing ab initio quality force fields from condensed phase quantum-mechanics/molecular-mechanics calculations through the adaptive force matching method.* J. Chem. Phys., 2008. **129**(6).

53. Kusalik, P.G. and I.M. Svishchev, *The spatial structure in liquid water.* Science, 1994. **265**: p. 1219-1221.

54. Mahoney, M.W. and W.L. Jorgensen, *Diffusion constant of the TIP5P model of liquid water.* J. Chem. Phys., 2001. **114**: p. 363-366.

55. Baez, L.A. and P. Clancy, *Existence of a density maximum in extended simple point-charge water.* J. Chem. Phys., 1994. **101**: p. 9837-9840.

56. Wu, Y., H.L. Tepper, and G.A. Voth, *Flexible simple point-charge water model with improved liquid state properties.* J. Chem. Phys., 2006. **124**(024503).

57. Abascal, J.L.F. and C. Vega, *A general purpose model for the condensed phases of water: TIP4P/2005.* J. Chem. Phys., 2005. **123**(234505).

58. Pi, H.L., et al., *Anomalies in water as obtained from computer simulations of the TIP4P/2005 model: density maxima, and density, isothermal compressibility and heat capacity minima.* Mol. Phys., 2009. **107**: p. 365-374.

59. Pinnick, E.R., S. Erramilli, and F. Wang, *Predicting the melting temperature of ice-Ih with only electronic structure information as input.* J. Phys. Chem, 2012. **137**(1).

60. Jorgensen, W.L. and J.D. Madura, *Temperature and size dependence for monte carlo simulations of TIP4P water.* Mol. Phys., 1985. **56**: p. 1381-1392.

61. Holten, V., et al., *Nature of the anomalies in the supercooled liquid state of the mW model of water.* J Chem Phys, 2013. **138**(17): p. 174501.

62. Nilsson, A. and L.G.M. Pettersson, *Perspective on the structure of liquid water.* Chemical Physics, 2011. **389**(1-3): p. 1-34.

63. Nilsson, A. and L.G. Pettersson, *The structural origin of anomalous properties of liquid water.* Nat Commun, 2015. **6**: p. 8998.

64. Huang, C., et al., *The inhomogeneous structure of water at ambient conditions.* Proc Natl Acad Sci U S A, 2009. **106**(36): p. 15214-8.

65. Song, Y., O. Akin-Ojo, and F. Wang, *Correcting for dispersion interaction and beyond in density functional theory through force matching.* J. Chem. Phys., 2010. **133**(17).

66. Shuichi Takahara, M.N., and Shigeharu Kittaka*, *Neutron Scattering Study on Dynamics of Water Molecules in MCM-41.* J. Phys. Chem. B 1999. **103**: p. 5814-5819.

67. Faraone, A., et al., *Fragile-to-strong liquid transition in deeply supercooled confined water.* J Chem Phys, 2004. **121**(22): p. 10843-6.

68. Liu, L., et al., *Pressure dependence of fragile-to-strong transition and a possible second critical point in supercooled confined water.* Phys Rev Lett, 2005. **95**(11): p. 117802.

69. Mallamace, F., et al., *The fragile-to-strong dynamic crossover transition in confined water: nuclear magnetic resonance results.* J Chem Phys, 2006. **124**(16): p. 161102.

70. Jahnert, S., et al., *Melting and freezing of water in cylindrical silica nanopores.* Phys Chem Chem Phys, 2008. **10**(39): p. 6039-51.

71. Yoshida, K., et al., *Thermodynamic, structural, and dynamic properties of supercooled water confined in mesoporous MCM-41 studied with calorimetric, neutron diffraction, and neutron spin echo measurements.* J Chem Phys, 2008. **129**(5): p. 054702.

72. Faraone, A., et al., *Single particle dynamics of water confined in a hydrophobically modified MCM-41-S nanoporous matrix.* J Chem Phys, 2009. **130**(13): p. 134512.

73. Chen, P.G.M.R.a.S.-H., *Dynamic Crossover in Supercooled Confined Water Understanding Bulk Properties through Confinement.* The Jounal of Physical Chemistry Letter, 2010: p. 5.

74. Khalid Elamin, H.J.a.J.S., *Dynamics of aqueous binary glass-formers confined in MCM-41*. Phys.Chem.Chem.Phys., 2015. **17**: p. 12978.

75. Sattig, M. and M. Vogel, *Dynamic Crossovers and Stepwise Solidification of Confined Water: A (2)H NMR Study.* J Phys Chem Lett, 2014. **5**(1): p. 174-8.

76. Cerveny, S., et al., *Confined Water as Model of Supercooled Water.* Chem Rev, 2016. **116**(13): p. 7608-25.

77. Mattias Sattig, S.R., Franz Fujara, Mayke Werner, Gerd Buntkowsky, Michael Vogel, *NMR studies on the temperature-dependent dynamics of confined water.* Phys. Chem. Chem. Phys, 2014. **16**: p. 12.

78. Findenegg, G.H., et al., *Freezing and melting of water confined in silica nanopores.* Chemphyschem, 2008. **9**(18): p. 2651-9.

79. Guichet, X., M. Fleury, and E. Kohler, *Effect of clay aggregation on water diffusivity using low field NMR.* J Colloid Interface Sci, 2008. **327**(1): p. 84-93.

80. Fleury, M., et al., *Characterization and Quantification of Water in Smectites with Low-Field NMR.* The Journal of Physical Chemistry C, 2013. **117**(9): p. 4551-4560.

81. Duncan Akporiaye, E.W.H., . Ralf Schmidt, and Michael Stiicker, *Water-Saturated Mesoporous MCM-41 Systems Characterized by 'H NMR.* J. Phys. Chem., 1994. **98**: p. 1926-1928.

82. Alba-Simionesco, C., et al., *Effects of confinement on freezing and melting.* Journal of Physics: Condensed Matter, 2006. **18**(6): p. R15-68.

83. Nagoe, A., et al., *Findings of Cp Maximum at 233 K for the Water within Silica Nanopores and Very Weak Dependence of the Tmax on the Pore Size.* J. Phys. Chem. B, 2010. **114**: p. 13940–13943.

84. Mallamace, F., et al., *Dynamical properties of confined supercooled water: an NMR study.* Journal of Physics: Condensed Matter, 2006. **18**(36): p. S2285-S2297.

85. Ikeda, M. and M. Aniya, *Understanding the Vogel–Fulcher–Tammann law in terms of the bond strength–coordination number fluctuation model.* Journal of Non-Crystalline Solids, 2013. **371-372**: p. 53-57.

86. Rault, J., *Origin of the Vogel-Fulcher-Tammann law in glass-forming materials: the alpha-beta bifurcation.* J. Non-Crystalline Sol., 2000. **271**: p. 177-277.

87. Futamura, R., et al., *Negative thermal expansion of water in hydrophobic nanospaces.* Phys Chem Chem Phys, 2012. **14**(2): p. 981-6.

88. Domin, K., et al., *Structure of Ice in Confinement: Water in Mesoporous Carbons.* Journal of Chemical & Engineering Data, 2016. **61**(12): p. 4252-4260.

89. Crupi, V., et al., *Confinement influence in liquid water studied by Raman and neutron scattering.* J. Phys. Cond. Matt., 2000. **12**(311).

90. Mallamace, F., et al., *The anomalous behavior of the density of water in the range 30 K < T < 373 K.* Proc Natl Acad Sci U S A, 2007. **104**(47): p. 18387-91.

91. Bloch, F., *Nuclear induction.* Physical Review, 1946.

92. Abragam, A., *Principle of Nuclear Magnetism.* Oxford Science Publications, 1989.

93. LevItt, M.H., *Spin Dynamics: Basics of Nuclear Magnetic Resonance.* WILEY, 1990.

94. Bloch, F. and A. Siegert, *Magnetic Resonance for Nonrotating Fields.* Physical Review, 1940. **57**(6): p. 522-527.

95. Bloembergen, N., E.M. Purcell, and R.V. Pound, *Relaxation Effects in Nuclear Magnetic Resonance Absorption.* Physical Review, 1948. **73**(7): p. 679-712.

96. Hahn, E.L., *Spin Echoes.* Physical Review, 1950. **80**(4): p. 580-594.

97. Carr, H.Y. and E.M. Purcell, *Effects of Diffusion on Free Precession in Nuclear Magnetic Resonance Experiments.* Physical Review, 1954. **94**(3): p. 630-638.

98. Meiboom, S. and D. Gill, *Modified Spin-Echo Method for Measuring Nuclear Relaxation Times.* Review of Scientific Instruments, 1958. **29**(8): p. 688-691.

99. Kohmotoa, T., et al., *Spectral hole burning in NMR: Experimental test of relaxation theories by using well-characterized noise fields.* Journal of Luminescence, 1995. **64**: p. 51-54.

100. Todica, M. and B. Blumich, *Hole-burning NMR in strongly inhomogeneous fields.* Solid State Nucl Magn Reson, 2007. **32**(2): p. 66-70.

101. Ito, K., C.T. Moynihan, and C.A. Angell, *Thermodynamic determination of fragility in liquids and a fragile-to-strong liquid transition in water.* Nature, 1999: p. 492-495.

102. Yue, Y. and C.A. Angell, *Clarifying the glass-transition behaviour of water by comparison with hyperquenched inorganic glasses.* Nature Physics, 2004. **427**.

103. Kohl, I., et al., *Water Behaviour: glass transition in hyperquenched water?* Nature, 2005. **435**(7041): p. E1; discussion E1-2.

104. Angell, C.A., *Insights into phases of liquid water from study of its unusual glass-forming properties.* Science, 2008. **319**(5863): p. 582-7.

105. Moynihan, C.T., et al., *Dependence of glass transition on cooling and heating rate.* J. Phys. Chem, 1974. **78**(26).

106. Pople, J.A., *Proton Magnetic Resonance of Hydrocarbons.* J Chem Phys, 1956. **24**(5): p. 1111-1111.

107. Jonathan, N., S. Gordon, and B.P. Dailey, *Chemical Shifts and Ring Currents in Condensed Ring Hydrocarbons.* J Chem Phys, 1962. **36**(9): p. 2443-2448.

108. Pople, J.A. and K.G. Untch, *Induced Paramagnetic Ring Currents.* J. Am. Chem. Soc., 1966. **88**(21): p. 4811-4815.

109. Xing, Y.-Z., et al., *Probing carbon micropore size distribution by nucleus independent chemical shift.* Carbon, 2014. **77**: p. 1132-1139.

110. Mallamace, F., et al., *The dynamical crossover phenomenon in bulk water, confined water and protein hydration water.* J Phys Condens Matter, 2012. **24**(6): p. 064103.

111. Chong, Y., et al., *Dominant Alcohol-Protein Interaction via Hydration-Enabled Enthalpy-Driven Binding Mechanism.* J Phys Chem B, 2015. **119**(17): p. 5367-75.

112. Chong, Y., A. Kleinhammes, and Y. Wu, *Protein dynamics and thermodynamics crossover at 10°C: Different roles of hydration at hydrophilic and hydrophobic groups.* Chemical Physics Letters, 2016. **664**: p. 108-113.

113. Luo, Z.X., et al., *Electroneutrality breakdown and specific ion effects in nanoconfined aqueous electrolytes observed by NMR.* Nat Commun, 2015. **6**: p. 6358.

114. Chiavazzo, E., et al., *Scaling behaviour for the water transport in nanoconfined geometries.* Nat Commun, 2014. **5**: p. 4565.

115. K. Overloop, V.G., *Freezing for Adsorbed Water as Studied by NMR.* Jounal of Magnetic Resonance, 1993. **Series A**(101): p. 179-187.

116. Schreiber, A., I. Ketelsen, and G.H. Findenegg, *Melting and freezing of water in ordered mesoporous silica materials.* Physical Chemistry Chemical Physics, 2001. **3**(7): p. 1185-1195.

117. Takaiwa, D., et al., *Phase diagram of water in carbon nanotubes.* Proc Natl Acad Sci U S A, 2008. **105**(1): p. 39-43.

118. Mallamace, F., et al., *Evidence of the existence of the low-density liquid phase in supercooled, confined water.* Proc Natl Acad Sci U S A, 2007. **104**(2): p. 424-8.

119. Xu, L., et al., *Relation between the Widom line and the dynamic crossover in systems with a liquid-liquid phase transition.* Proc Natl Acad Sci U S A, 2005. **102**(46): p. 16558-62.

120. Mallamace, F., et al., *NMR evidence of a sharp change in a measure of local order in deeply supercooled confined water.* Proc Natl Acad Sci U S A, 2008. **105**(35): p. 12725-9.

121. Limmer, D.T. and D. Chandler, *Phase diagram of supercooled water confined to hydrophilic nanopores.* J Chem Phys, 2012. **137**(4): p. 044509.

122. Maruyama, S., K. Wakabayashi, and M. Oguni, *Thermal Properties of Supercooled Water Confined within Silica Gel Pores.* 2004. **708**: p. 675-676.

123. Swenson, J., *The glass transition and fragility of supercooled confined water.* Journal of Physics: Condensed Matter, 2004. **16**(45): p. S5317-S5327.

124. Debenedetti, P.G., *Metastable Liquids: concepts and principles. Physical chemistry.* Princeton University Press, 1996.

125. Anderson, P.W., *Through the Glass Lightly.* Science, 1995. **267**(5204): p. 1617-1617.

126. Debenedetti, P.G. and F.H. Stillinger, *Supercooled liquids and the glass transition.* Nature, 2001. **410**(6825): p. 259-267.

127. Johari, G.P., A. Hallbrucker, and E. Mayer, *The glass-liquid transition of hyperquenched water.* Nature, 1987. **330**: p. 552-553.

128. Angell, C.A., *in Water: a Comprehensive Treaties.* Plenum, New York, 1982. **7**.

129. Kuhns, P.L. and M.S. Conradi, *NMR hole-burning: A study of slow molecular rotations in glassy glycerol.* J Chem Phys, 1982. **77**(4): p. 1771-1778.

130. Sigmund, E.E. and W.P. Halperin, *Hole-burning Diffusion Measurements in High Magnetic Field Gradients.* 2008.

131. Woessner, D.E. and J. B. S. Snowden, *A PULSED NMR STUDY OF DYNAMICS AND ORDERING OF WATER MOLECULES IN INTERFACIAL SYSTEMS.* Ann. NY. Acad. Sci., 1973: p. 113-124.

132. Pascala, T.A., W.A. Goddarda, and Y. Junga, *Entropy and the driving force for the filling of carbon nanotubes with water.* Proc. Nat. Acad. Sci., 2011. **108**(29): p. 11794-11798.

133. Krynicki, K., *Proton spin-lattice relaxation in pure water between 0°C and 100°C.* Physica 1966. **32**: p. 167-178.

134. Hindman, J.C., A. Svirmickas, and M. Wood, *Relaxation processes in water. A study of the proton spin-lattice relaxation time.* J Chem Phys, 1973. **59**(3): p. 1517-1522.

135. Amman, C., P. Meier, and A.E. Merbach, *A Simple Multinuclear NMR Thermometer.* J. Magn. Reson., 1982. **46**: p. 319-321.

136. Smith, D.W.G. and J.G. Powles, *Proton spin-lattice relaxation in liquid water and liquid ammonia.* Molecular Physics, 1966. **10**(5): p. 451-463.

137. Korb, J.P., S. Xu, and J. Jonas, *Confinement effects on dipolar relaxation by translational dynamics of liquids in porous silica glasses.* J Chem Phys, 1993. **98**(3): p. 2411-2422.